GRAPHENE-BASED ELECTRODES FOR HIGH-PERFORMANCE ELECTROCHEMICAL ENERGY STORAGE

A Dissertation
Presented to
The Academic Faculty

by

Byeongyong Lee

In Partial Fulfillment
of the Requirements for the Degree
Doctor of Philosophy in the
George W. Woodruff School of Mechanical Engineering

Georgia Institute of Technology
December 2018

GRAPHENE-BASED ELECTRODES FOR HIGH-PERFORMANCE ELECTROCHEMICAL ENERGY STORAGE

Approved by:

Dr. Seung Woo Lee, Advisor
The George W. Woodruff School of Mechanical Engineering
Georgia Institute of Technology

Dr. Hesketh Peter
The George W. Woodruff School of Mechanical Engineering
Georgia Institute of Technology

Dr. Hailong Chen
The George W. Woodruff School of Mechanical Engineering
Georgia Institute of Technology

Dr. Seung Soon Jang
School of Material Science and Engineering
Georgia Institute of Technology

Dr. Thomas Fuller
School of Chemical & Biomolecular Engineering
Georgia Institute of Technology

Date Approved: July 30, 2018

ACKNOWLEDGEMENTS

I would like to thank my advisor, Dr. Seung Woo Lee, for his advice and encouragement. I appreciate that I am one of his first graduate students. As a start-up member in his group, I could get valuable experiences for my future career. I would like to thank my committee members, prof. Peter J. Hesketh, prof. Hailong Chen, prof. Seung Soon Jang and prof. Thomas F. Fuller, for their comments on my research.

I gratefully thank my collaborators, prof. Suguru Noda and prof. Zhongming Chen. They prepared few-walled carbon nonotube that was widely employed in my research. I thanks to prof. Hee Dong Jang and Dr. Sunkyung Kim for constructive discussion on the preparation of crumpled graphene and submicron Si particles. I appreciate prof. Kwangsup Eom for discussion on overall electrochemistry which helps me to analyze my experimental results. I truly thank Prof. Shuo Chen and Linxin Xie for their devotion to material characterization. I thank my collaborator, Dr. Seokjoon Kwon for collaborations on understanding the charge storage mechanism of graphene. I would also thank Prof. Maenghyo Cho for his advice on finding my research area. I would like to thank my collaborators and friends, Dr. Tianyuan Liu and Mr. Michael J. Lee, including all the group members in prof. Lee's group.

Above all things, I truly thank my wife, Hyunji Kim, and my sons, Eldor and Marvin for supporting me with their endless encouragement.

I gratefully acknowledge financial support from prof. Lee's Georgia Institute of Technology startup fund, Samsung Advanced Institute of Technology (SAIT)'s Global

Research Outreach (GRO) program and Korea Institute of Geoscience and Mineral Resources (KIGAM).

TABLE OF CONTENTS

LIST OF TABLES

LIST OF FIGURES

LIST OF SYMBOLS AND ABBREVIATIONS

AC	Activated carbon
A-CG	Activated crumpled graphene
AFM	Atomic force microscopy
BCC	Body centered cubic
BJH	Barrett-Joyner-Halenda
CE	Coulombic efficiency
CG	Crumpled graphene
CGA	Generalized gradient approximation
CGO	Crumpled graphene oxide
C-GR	Cabbage-like graphene
CNT	Carbon nanotube
CS	Carbon sphere
CV	Cyclic voltammetry
CVD	Chemical vapor deposition
DFT	Density functional theory
DMC	Dimethyl carbonate
DV	Double vacancy
EC	Ethylene carbonate

EDLC	Electrochemical double-layer capacitor
EDX	Energy dispersive X-ray
EIS	Electrochemical impedance spectroscopy
ESR	Equivalent series resistance
EV	Electric vehicle
FFT	Fast Fourier transform
FTIR	Fourier transform infrared
GCD	Galvanostatic charge and discharge
GITT	Galvanostatic intermittent titration technique
GO	Graphene oxide
HC	Hard carbon
HRTEM	High resolution transmission electron microscopy
HSC	Hybrid supercapacitor
HT	Heat treatment
HTC	Hydrothermal carbonization
KIB	Potassium ion battery
LIB	Lithium ion battery
NMP	N-methyl-2-pyrrolidone
PAW	Projector augmented wave
PBE	Perdue-Burke-Ernzerhof
PDCV	Potential-dependent cyclic voltammetry

PDDA	Poly (diallydimethylammonium chloride)
PVDF	Polyvinylidene difluoride
R_{ct}	Charge transfer resistance
RGO	Reduced graphene oxide
R_s	Electrolyte resistance
R_{SEI}	Solid electrolyte interface resistance
SAED	Selected area electron diffraction
SC	Supercapacitor
SEI	Solid electrolyte interphase
SEM	Scanning electron microscopy
SIB	Sodium ion battery
SV	Single vacancy
SW	Stone-Wales
TDFC	Two-dimensional functional carbon
TGA	Thermo gravimetric analysis
XPS	X-ray photoelectron spectroscopy
XRD	X-ray diffraction

SUMMARY

Graphene, a two-dimensional honeycomb carbon layer, has drawn intensive attention as a promising electrode material for rechargeable batteries and supercapacitors due to its high electrical conductivity as well as chemical and physical stability. Recent progress of large-scale synthesis of graphene oxide (GO) from graphite has boosted more investigations for the conversion of GO to graphene. For energy storage applications, the role of graphene can be largely categorized into two groups: A) An inactive, supporting component for the build-up of composites with various active materials and B) Graphene itself as an active material for charge storage.

Graphene, as a supporting component, is not involved electrochemical reactions to store charge or contribute to the amount of charge storage with very limited capacity or capacitance. Regarding this role, graphene-encapsulated submicron Si and two-dimensional functional carbon (TDFC) synthesis using graphene-template were studied in tow sub-themes. In the graphene-encapsulated submicron Si study, submicron Si particles were recovered from Si waste and utilized as a high-performance anode material for LIBs. From the versatile hydrothermal assembly, submicron Si particles were securely coated with graphene. The submicron Si/graphene composite exhibited good cycling stability, showing a capacity retention of 84% at the 100th cycles. In the study of the TDFC, ultrathin TDFC (thickness of 10~20nm) with abundant oxygen functional groups was prepared by GO-template assisted hydrothermal reaction of glucose. During the hydrothermal reaction, GO acted as a substrate for depositing hydrocarbon on its surface. Due to the presence of oxygen functional group on the surface of GO and the planar morphology of GO, the

prepared 2D thin film enables more efficient utilization of the redox reactions compared to the conventional carbon sphere, showing a key approach to effectively utilize their redox-reactions.

In addition, graphene actively participates in charge storage and thus graphene can be identified as an active material. It is known that an irreversible restacking of GO sheets during electrode preparation has limited the accessible surface area (ASA) to store ions, resulting in a low gravimetric capacity of ~100 mAh g^{-1}. In this section, three subtopics of graphene as the active material for charge storage were investigated; A) Crumpled graphene oxide cathode for lithium-ion battery (LIB). B) Stacking-controlled cabbage-like graphene electrodes for supercapacitor. C) Crumpled graphene anode for Sodium-ion battery. The second group is mostly associated with the restacking issue of GO and graphene. In the study of crumpled graphene oxide cathode, the crumpled graphene oxide was employed as cathode material for LIB. The crumpled graphene oxide has an aggregation-resistive characteristic and 3D ball-like morphology. The crumpled graphene oxide showed that the effective utilization of the surface redox reactions with enhanced electrochemical energy storage such as high rate-capability, indicating that the microstructure of graphene is an important parameter for the development of high-power LIBs. In the study of cabbage-like graphene, high density cabbage-like graphene (0.75 g cm^{-3}) was prepared by two step processes of liquid-phase pre-stacking of graphene and subsequent aerosol spray drying. Despite its high density, the cabbage-like graphene showed a high gravimetric and volumetric capacitance (177 F g^{-1} and 117 F cm^{-3}) in aqueous supercapacitors. As a cathode for LIB, it showed a capacity of 176 mAh g^{-1} (1.0 mAh cm^{-2}). This superior electrochemical performance suggests that the stacking-control

approach could provide a new way to achieve both high gravimetric and high volumetric performance of graphene electrodes rather than avoiding restacking. In the study of crumpled graphene anode for sodium-ion battery (SIB), it has been shown that graphene stores sodium ions through capacitive mechanism and there are two sub-routes in the capacitive mechanism, ion adsorption in a similar way of double layer capacitance and ion adsorption on defective sites.

In summary, this dissertation discusses the various roles of graphene for energy storage application, such as supercapacitor, LIB, SIB and hybrid supercapacitor. In each application, graphene can be identified as active or inactive material based on its role. The results in various applications using graphene would provide insights how graphene play a role for high performance energy storage.

CHAPTER 1. INTRODUCTION

1.1 Energy storage systems: Lithium-ion battery and electrochemical capacitor

Rapid penetration of portable electronic devices electric vehicles (EVs) to our daily lives demands electrochemical energy storage devices with a high-energy and high-power density, and long-lasting lifetime.[1-2] A significant volume of research has been devoted to the development of such energy storage systems (EESs).[3-4] At forefront of these are lithium-ion batteries (LIBs) and electrochemical capacitors (ECs).[5] Because of their different energy storage characteristics,[5-7] LIBs and ECs show complementary energy-storage features (**Figure. 1.1**) In typical, LIBs utilize intercalation of Li ions into active materials of anodes and cathodes which is oft referred as diffusion-controlled process. For instance, the most commercialized electrodes materials such as graphite and lithium cobalt oxide ($LiCoO_2$) host Li ions into their layers. Thus, LIBs provide a high energy density of ~200 Wh kg^{-1}. However, they suffer from limited cycling stability. For instance, $Li_{1-x}CoO_2$ can only maintain its structure in an interval of $0.5>x>0$. When a cell is overcharged (i.e., Li is excessively extracted), $Li_{1-x}CoO_2$ shows rapid structural degradation.[8-9] Although the graphite is recognized as the most stable anode material for LIB, the graphite is also electrochemically degraded upon lithiation and delithiation because of extended solid electrolyte interface into the internal structure of graphite (i.e., internal pore of graphite).[10] Moreover, LIB shows a limited power density less than 1 kW kg^{-1} due to the diffusion-controlled process.[11-12] On the contrary, ECs (so-called supercapacitors, SCs), store charge using electrolyte ion adsorption. ECs are typically classified into electrochemical double-layer capacitors (EDLCs) and pseudocapacitors (PCs). Both EDLC and PC store ions on

the electrode surface and they are identified as a surface-limited energy storage system. Unlike the EDLC, PCs store charges through surface redox reactions on top of the double layer capacitance, showing an increased energy density compared to EDLCs.[5, 13] By virtue of the EC's charge storage mechanism, ECs show high power density and good life cycle.[14]

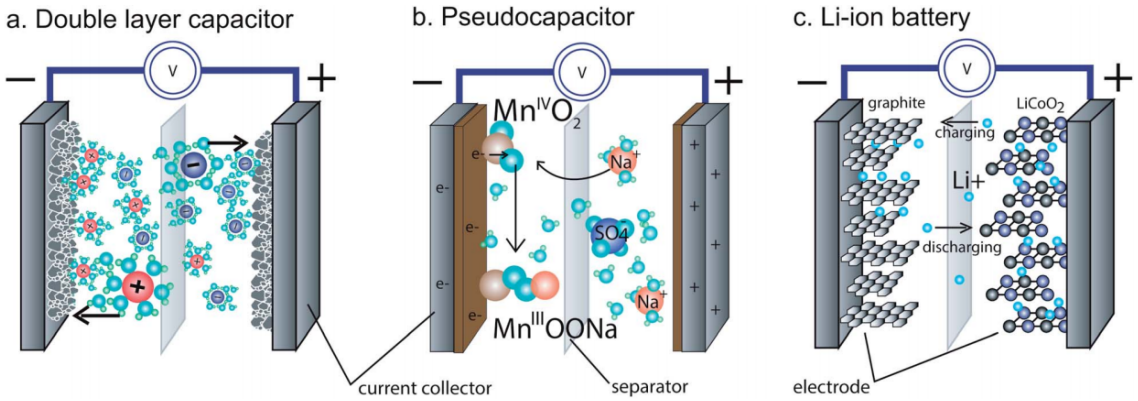

Figure 1.1 Schematic illustration of (a) all carbon electrochemical double layer capacitor, (b) pseudocapacitor and (c) lithium ion battery. All devices have an active material, a current collector, a separator and electrolyte. Reprinted with permission from Ref#13 Copyright © 2014 Royal Society of Chemistry.

An emerging target in next-generation EES is delivering both high energy and power with a single energy storage system. In this regard, hybrid supercapacitors (HSCs) have been explored to bridge batteries and ECs by combining the features of batteries and ECs.[15-17] HSCs consist of a high-energy battery anode, a high-power EC cathode, and Li salts containing organic electrolytes to realize different storage mechanisms at both electrodes. These asymmetric configurations give a difference between HSCs and conventional asymmetric SCs in which asymmetric SCs employ two different capacitive electrodes. HSCs can have a higher energy density than SCs due to the high capacity of the battery-type anode and a higher power density than LIBs due to the capacitive cathode.

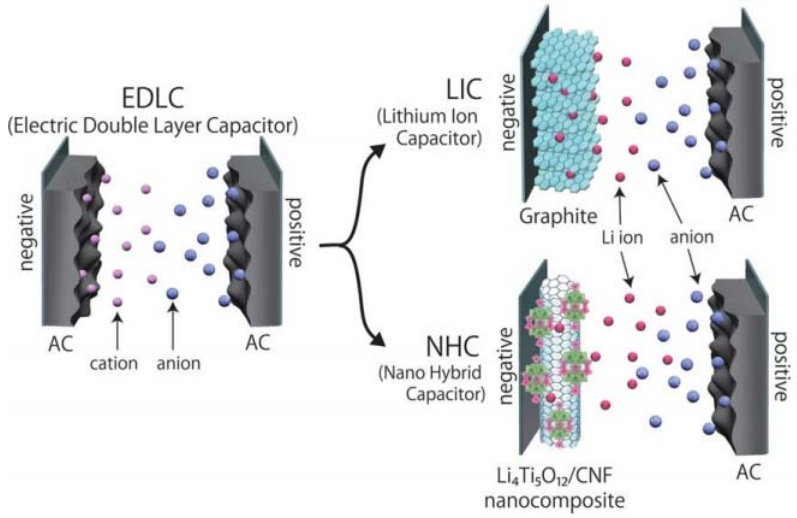

Figure 1.2 Schematic illustration of an ordinary electric double layer capacitor (EDLC) system and hybrid supercapacitor. Conventional EDLC has a symmetric cell configuration of activated carbon for both positive and negative electrodes. Hybrid supercapacitor, herein lithium ion capacitor, employs Li-intercalation negative electrode material (e.g., graphite and $Li_4Ti_5O_{12}$) and capacitive positive electrode material. Reprinted with permission from Ref#18 Copyright © 2012 Royal Society of Chemistry.

Table 1.1 Properties of Graphene compared with other carbon materials.[19]

	Graphene	Carbon nanotube	Fullerene	Graphite
Dimensions	2	1	0	3
Hybridization	sp^2	Mostly sp^2	Mostly sp^2	sp^2
Hardness	Highest	High	High	High
Tenacity	Flexible, elastic	Flexible, elastic	Elastic	non-elastic
Experimental SSA ($m^2\ g^{-1}$)	~1,500	~1,300	80–90	~10–20
Electrical conductivity ($S\ cm^{-1}$)	~2,000	Structure-dependent	10^{-10}	Anisotropic
Thermal conductivity ($W\ m^{-1}\ K^{-1}$)	4,840–5,300	3,500	0.4	Anisotropic

1.2 Preparation of graphene

Since the first finding of a Free-State graphene in 2004, interest in graphene results in 'graphene gold rush'.[19-20] Graphene has appealing properties for a wide range of applications such as transistor,[21] energy storage, conductive supporter[22] and sensors because of its two-dimensional morphology, mechanical stability, surface area (~1500 m^2 g^{-1}) and electrical conductivity (~2000 S cm^{-1}) compared to the other forms of carbon (**Table 1.1**).[23-25] Therefore, graphene could play various roles as active and inactive materials for those EESs.

Graphene is a honeycomb-like 2D carbon. Preparation of graphene can be largely categorized into two groups (**Fig. 1.3**); A) Top-down and B) bottom-up approach. The top-down approach mostly starts from graphite since graphite is a stack of graphene layers.[25] In the category of the top-down approach, it is needed to overcome van der Walls forces to separate each single layer of graphene from graphite. One of well-known ways in the top-down approach is 'peel-off' (also called scotch tape method).[20] Although high-quality (i.e., defect free graphene) can be obtained from the 'peel-off' method, scalable production of graphene sheets using this method is difficult. Electrochemical exfoliation, exfoliation of graphite intercalation compounds (GICs) and solvent-based exfoliation have been proposed as scalable methods to prepare graphene. In electrochemical exfoliation, graphite is employed as a sacrificial electrode with the various electrolytes.[26] In the case of exfoliation of GICs, graphene is prepared by two step process of lithium salt intercalated and subsequent sonication.[27-28] In 2008, exfoliation of natural graphite flake by sonication was also reported.[29] One of the most popular way to obtain graphene in top-down approach is to oxidize graphite to prepare GO and then thermally or chemically reduce the GO. In

these top-down approaches, the critical challenge is to prevent aggregation or restacking of GO and graphene. Thus, in many cases, surfactants are employed.[30-31] However, removal of surfactant is difficult. To prevent surfactant-free and aggregation-resistive graphene, Huang *et al*. employed aerosol-pyrolysis process for GO and obtained crumpled graphene.[32] Figure 1.4 shows the schematic illustration of aggregation-resistive graphene. First, aqueous GO solution is nebulized into a pre-heated tubular furnace with the inert gas flow. In the furnace, rapid evaporation of GO droplet occurs, concentrating GO sheets and compressing them into crumpled ball (thus so-called crumpled graphene).[32] Due to the inert gas environment and high temperature in the furnace, GO is reduced, thus yielding graphene at the outlet of the furnace. Crumpled graphene has a locally π- π stacked ridge structure which imparts aggregation-resistive property to graphene. Bottom-up approach can provide high quality high-quality crystallites up to 100μm.[33] In this approach, graphene is usually prepared by chemical vapor deposition (CV) on copper foils and growth on SiC.[34] Despite the high-quality, these methods are expensive to scale up because of large energy consumption at present.[23] The various preparation methods and applications of graphene are summarized in Figure 1.5.

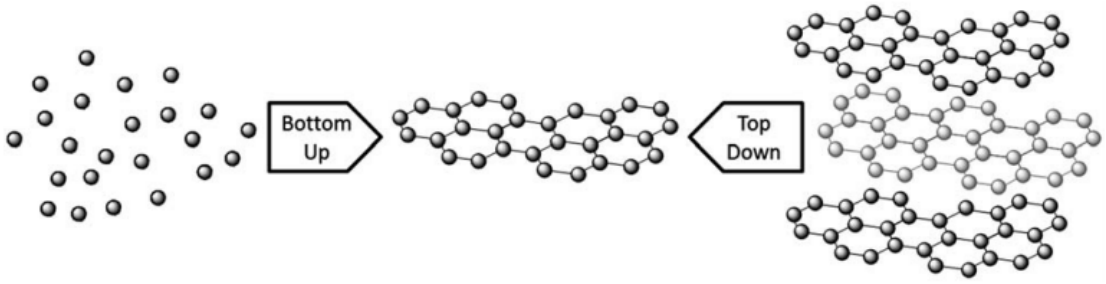

Figure 1.3 Schematic illustration of top-down and bottom-up graphene preparation. Reprinted with permission from Ref#25 Copyright © 2013 Royal Society of Chemistry.

Figure 1.4 Schematic illustration of aggregation-resistive graphene. Reprinted with permission from Ref#32 Copyright (2011) American Chemical Society.

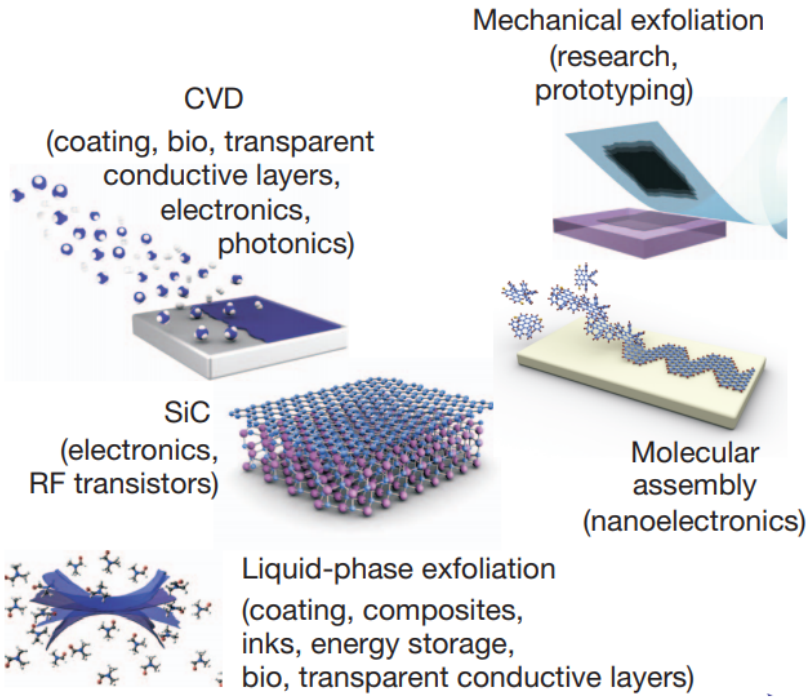

Figure 1.5 Various methods to prepare graphene and their applications. Reprinted with permission from Ref#23 Copyright ©2012 Springer Nature.

1.3 Graphene in energy storage applications

The role of graphene in energy storage application can be divided into graphene as the active material and the inactive component. When graphene directly takes part in energy, graphene can be looked upon as active material. For instance, graphene can host alkali metal ions (e.g., Li^+ and Na^+) in both negative and positive electrodes. Scorasati *et al*. prepared graphene flake by sonication and then utilized anode material for LIBs (**Fig. 1.6**).[35] Graphene anodes generally show ultra-high capacity in the first lithiation due to the formation of SEI and the large surface area of graphene.[36] In 2013, Dou e*t al.* reported reduced graphene anode for SIB.[37] Although authors showed good cycling stability and high capacity of the reduced graphene electrodes, the energy storage mechanism was not

elucidated. In 2014, Wang *et al*. prepared expanded graphite with the interlayer distance of 0.37 nm,[38] providing a hope for SIBs using graphene. Graphene's large theoretical surface area (~2675 m^2 g^{-1})[39] is the attractive feature for ECs since the specific capacitance of ECs is directly dependent on available surface area of electrodes. However, it is difficult to achieve the high surface area of graphene due to the restacking issue of graphene. Thus, various approaches to avoid the restacking of graphene have been proposed.[26, 50, 77, 121-122] For instance, physical '*spacers*' to separate the graphene nanosheet, three-dimensional graphene assembly and vertically aligned graphene have been introduced.[40-46] In this dissertation, we proposed crumpled graphene as discussed in chapter 4 and 6.

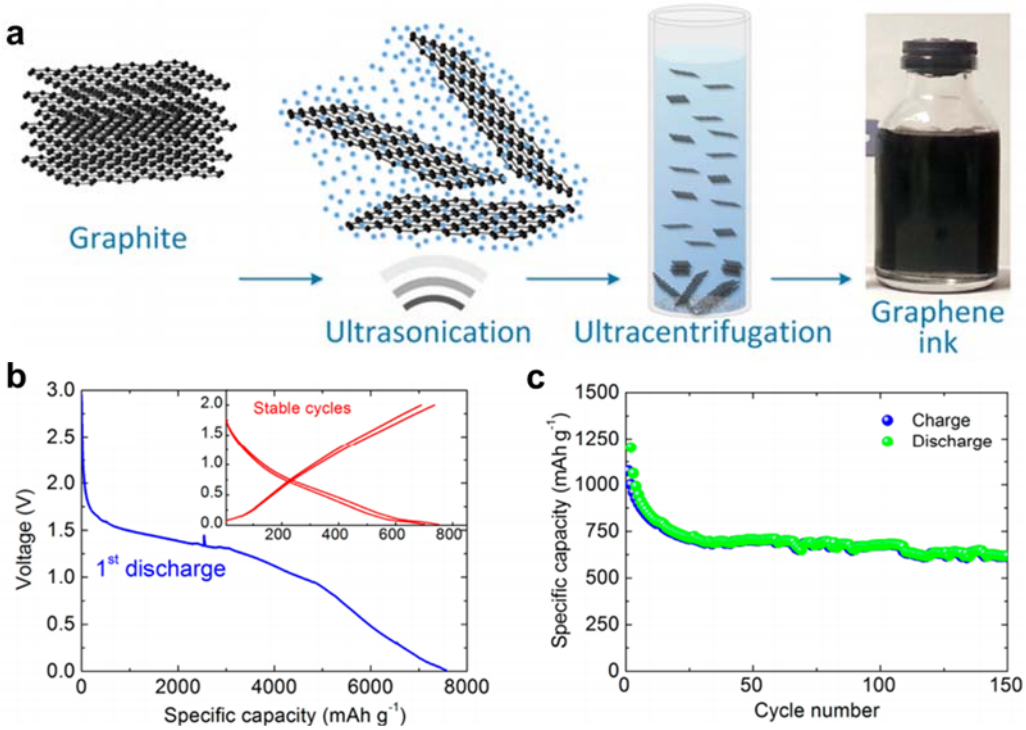

Figure 1.6 (a) Preparation of graphene. (b) Galavanostatic discharge profile of graphene anode in Li-cell (Inset: charge/discharge profile at steady-state). (c) Cycling stability of graphene in Li-cell. Reprinted with permission from Ref#35 Copyright (2014) American Chemical Society.

Graphene can be an assistant or supporter to enable a stable operation of EESs due to its high conductivity and, mechanical and electrochemical stability.[40, 47-48] In this role, graphene is not actively involved in charge storage reaction. First, graphene can impart electrical conductivity to poorly conductive, but electrochemically active materials, such as Lithium metal oxide cathodes (e.g., $LiFePO_4$, $LiCoO_2$ and $LiMnO_2$), Si and organic molecules. For instance, various composites, such as graphene-embedded $LiFePO_4$ and three-dimensional graphene/$LiFePO_4$ have been prepared.[49-50] The various forms of graphene-based composites are shown in Figure 1.7. In the case of poor conductive materials which accompany large volume change such as phosphorous and silicon, encapsulated, wrapped and layered composites were mostly investigated.[51] In Li-S batteries, the dissolution of elemental S and sulfide and their poor electrical conductivity are known as the most critical issues. In addition, graphene can be a promising candidate to resolve the issues of Li-S batteries.[52-53] For instance, Li_2S-graphene electrode prepared by dropping Li_2S precursor onto reduced GO paper showed stable cycling performance up to 150 cycles with a high capacity of ~750 mAh g^{-1}.[54]

It has been 14 years since the finding free-state graphene and numerous approaches of graphene for EES have shown noticeable progress. However, it is hard to find them in our daily life. In this thesis, to promote uptake of graphene in EESs, we considered the scalable synthesis of graphene-based electrodes as discussed in each chapter.

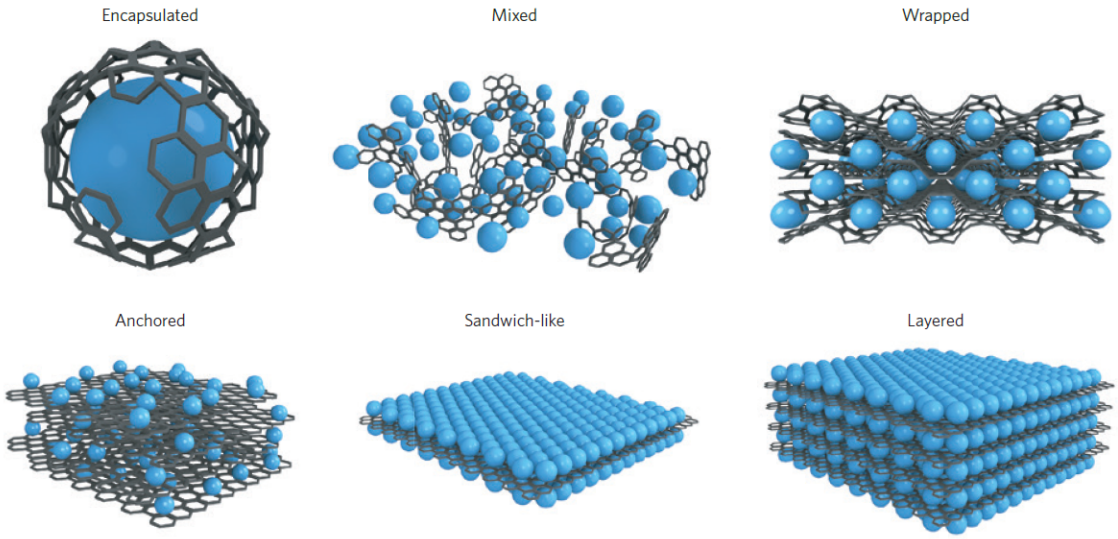

Figure 1.7 Schematic illustration of graphene-based composite electrodes. Reproduced from Ref#19 with permission of Springer Nature, Copyright ©2014.

1.4 Chapter Organization

Table 1.2 Summary of chapter organization

	Material	Role	Application			
			LIB	SIB	EC	-
Inactive	**Ch.2** Si/graphene composite	Physical protection layer	Anode			Hybrid supercapacitor in chapter 3
	Ch. 3 Two-dimensional functional carbon	Template	Cathode	Cathode		
Active	**Ch. 4** Crumpled graphene oxide	Charge Storage	Cathode			
	Ch. 5 Cabbage-like Graphene cabbage		Cathode		Electrode	
	Ch. 6 Crumpled graphene			Anode		

Chapter organization is summarized in **table 1.2**. In Chapter 2 and 3, graphene is employed as an inactive component (i.e., physical blocking layer or substrate to deposit hydrocarbon), which does not actively involve electrochemical reaction. In Chapter 2, graphene-encapsulated submicron Si (Si/graphene composite) is investigated as an anode material for LIBs. While pristine submicron Si shows a limited cycling stability, the Si/graphene composite exhibits stable cycling performance with the high reversible capacity (1423 mAh g^{-1}) and capacity retention of 84% at 100th cycle. Despite severe pulverization of Si during lithiation and delithiation, the pulverized Si particles are securely confined in graphene cage. In Chapter 3, two-dimensional functional carbon, which contains a large amount of redox-active oxygen functional group, is prepared using hydrothermal carbonization (HTC) of glucose. During the hydrothermal carbonization of glucose, we employed GO nanosheets as a template to control the morphology of hydrothermal products. The TDFC exhibits a very high capacity of ~250 mAh g^{-1} in the voltage window of 1.5-4.5 V vs. Li. Even with a commercial level mass-loading of ~9.3 mg cm^{-2}, the TDFC maintains a high capacity of ~243 mAh g^{-1}. The anode in Chapter 2 and the TDFC cathode in Chapter 3 are integrated to build a hybrid supercapacitor. The hybrid supercapacitor delivers a high-energy density of ~182 Wh kg^{-1} at a high-power density of 1 kW kg^{-1} and maintains its performance over 3,000 cycles. The study of the hybrid supercapacitor is discussed in Chapter 3.

In Chapter 3, 4 and 5, graphene is employed as an active component which means that graphene itself stores charge. In Chapter 4, crumpled graphene oxide is used as a cathode material for LIB. Graphene oxide can have redox reactions with lithium ions at the high potential of ~3 V vs. Li. However, due to severe restacking issue during the

preparation of electrodes, it shows limited capacity less than 100 mAh g^{-1} and poor rate-capability despite its copious redox active oxygen-functional group. Thus, in this chapter, crumpled graphene oxide, which has an aggregation-resistive property and 3D ball-like morphology, is employed. The crumpled graphene oxide shows the much higher capacity of 154 mAh g^{-1} at 0.1 A g^{-1} than GO. In Chapter 5, controllable and scalable stacking-engineering process of graphene is introduced for charge storage. From the stacking-engineering, cabbage-like graphene (C-GR) is prepared and investigated for aqueous symmetric supercapacitor with KOH electrolyte. In addition, the C-GR is employed as cathode material for LIB. This stacking-control strategy of GR provides an insight for 2D materials to enhance the charge storage. In Chapter 6, graphene's charge (Li, Na and K ion) storage mechanism is shown. Graphene stores alkali metal ions through two sub-routes of surface-capacitive charge storage: i) double layer capacitance and cation adsorption on defective sites. In this section, as a graphene model, crumpled graphene (CG) is employed.

Finally, Chapter 7 will provide a summary and perspective of graphene-based electrodes for energy storage applications.

CHAPTER 2.

CONFINEMENT OF SILICON PARTICLES IN GRAPHENE SHEATH

Reprinted with permission from Byeongyong Lee, Tianyuan Liu, Sun Kyung Kim, Han kwon Chang, Kwangsup Eom, Lixin Xie, Shuo Chen, Hee Dong Jang, and Seung Woo Lee *Carbon,* **2017** 119, 438-445. Figures and tables shown in this chapter were referred from *Carbon,* **2017** 119, 438-445 without a formal permission form based on Elsevier's policy "you retain the right to include it in a thesis or dissertation, provided it is not published commercially."

2.1 Overview

Si has drawn intensive attention as a next-generation anode material owing to its much higher theoretical capacity (4200 mAh g^{-1}) than graphite (372 mAh g^{-1}).[55-56] In spite of its high capacity, the practical application of Si in LIBs has been hindered by its low electrical conductivity and dramatic volume variation up to 400% during the insertion and extraction of Li.[57] The induced mechanical strain during the huge volume change pulverizes Si particles, resulting in disconnection of the small pulverized Si particles.[58] Moreover, the newly exposed Si surface promotes the continuous formation of a solid-electrolyte interphase (SEI), which is generated by the reductive decomposition of the organic electrolyte, causing the irreversible consumption of electrolyte and lithium.[59-61]

Numerous nanostructured designs of the Si anode have been proposed to address the issues. Experimental and computational studies have shown that Si nanoparticles, which

are smaller than ~150 nm, can effectively alleviate their mechanical strain, accordingly avoiding the severe pulverization.[62-63] Additionally, nanostructured Si, such as yolk-shell,[64-65] hollow Si, porous Si[66-68] and Si nanowire[69-70], have demonstrated good cycling stability using free space around Si to accommodate the volume expansion. Recently, Si nanoparticle and carbonaceous material composite systems have shown the improved cycling stability.[71-77] In these composites of Si and carbonaceous materials, the carbonaceous materials can not only provide the conductive pathways from Si to current collector for Si-based electrodes, but also prevent the direct exposure of Si particles to electrolytes, thus improving the performance of the anodes.[74-76] Despite the enhanced cycling stability and rate-capability, the nanostructured Si and composite anodes have scalability issues as they often employ costly Si nanoparticle.[78-80] For example, most of the nanostructured Si anodes have been constructed from the costly processes, such as CVD,[73, 81] laser deposition,[82] and magnesiothermic reduction.[83]

Over the past decades, Si has been mostly exploited in photovoltaic and semiconductor industries.[84] Annual demand of Si in photovoltaic and semiconductor industries was 50,000 tons in 2010 and is expected to hit over 180,000 tons in 2020.[85] Unfortunately, more than 40% of the Si used in the industries is directly being discarded as industrial Si waste.[86] The industrial Si waste, which is typically generated in the course of slicing Si ingots to obtain Si wafers, contains high purity Si, SiC and a small portion of metallic impurities. Researchers have proposed recovery of Si from the industrial Si waste to support a Si source for LIBs.[79, 86] However, they only utilized recovered Si nanoparticles less than 100nm or crushed the recovered Si particles into nanoparticles through high-energy ball milling, thus reducing the merit of the Si waste in cost-effectiveness and

scalability. In addition, the specific capacity and rate capability of these nanoparticles were lower than those of the nanostructured Si.

Micrometer-scale Si has been proposed to improve the low scalability.[48, 87-89] The micrometer-scale Si is generally more prone to mechanical fracture upon cycling compared to the Si nanoparticles owing to the lithiation-induced swelling.[62] In addition, the ion and electron transport pathways in micrometer-scale Si is longer than those in Si nanoparticles, giving rise to the adverse impact in rate-capability.[89] To address these issues in the mechanical fracture and rate-capability , conformably graphene-coated micro-Si[48] , porous bulk Si[87-88] and micro-sized Si-C[89] have been explored. Although these studies have shown the improved electrochemical performance, the electrode fabrication processes still rely on toxic chemicals such as hydrofluoric acid or complicated fabrication procedures. Therefore, it is highly desirable to develop simple, scalable and toxic-free fabrication process for high-performance Si electrode using large Si particles recycled from the waste.

2.2 Approach

In this section, we propose a graphene-encapsulated submicron Si as an anode material for LIBs. The graphene-encapsulated submicron Si was prepared by recovery of submicron Si (sm-Si) from the industrial Si waste and subsequent hydrothermal graphene encapsulation. This graphene-encapsulated submicron Si provides several advantages: A. Recycling of industrial waste. B. Submicron size Si. C. No use of toxic-chemicals in electrode fabrication. D. High reversible capacity (1423 mAh g^{-1}) and cycling stability (Capacity retention at 100th cycle, 84%)

The enhanced electrochemical performance can be attributed to the effective encapsulation of sm-Si particles by graphene. As discussed in section.1, the graphene has a good mechanical strength and high electrical conductivity. Therefore, the graphene can be an ideal coating material for such a material which has a poor electrical conductivity and suffer from large volume change during lithiation and delithiation.

2.3 Experimental Methods

2.3.1 Sample Preparation

The sm-Si was recovered from industrial Si waste through mild centrifugation and removal of impurities.[90] The Si waste from a Korean semiconductor company was dried at 180 °C to remove a lubricant (diethylene glycol). 2g of the dried Si waste was sonicated for 5 h (40 kHz, Bransonic co.) in 200 mL of deionized (DI) water. Then, centrifugation (VS-5500N, Vision Science) was applied to the Si waste colloid at 500 rpm for 12 min. After the mild centrifugation, the Si waste colloid was separated into two parts: Si-rich supernatant and SiC-rich sediment. The supernatant was subjected to the 2M hydrochloric acid treatment at 100 °C for 5 h. After rinsing the supernatant with DI water several times, the Si particles with the size range from hundred nanometers to several micrometers were obtained. These Si particles were slightly ground by beads-mill (Ultra Apex Mill UAM-015, Kotobuki) for 9 cycles, crating sm-Si particles close to 1 μm. The recovered sm-Si particles were used for Si sources for the electrode fabrication. 400 mg of the recovered sm-Si was dispersed in 40 mL of DI water by sonication for 20 min and then 0.5 mL of 20 wt% Poly (diallydimethylammonium chloride) (PDDA, Sigma Aldrich) was added into the dispersion. The mixture of the sm-Si and PDDA was sonicated for 10 min. To remove

excessive PDDA, the mixture of the sm-Si and PDDA was centrifuged and rinsed with DI water for several times. The estimated concentration of the positively charged submicron Si colloid was 10 mg mL^{-1}. GO was prepared by modified Hummer's method.[91] Then, 60 mg of D-glucose (Sigma Aldrich) was dissolved in 15 mL of 2 mg mL^{-1} GO solution by sonication for 20 min. The sm-Si@C/Gr was prepared by hydrothermal one-pot synthesis. 3 mL of the positively charged sm-Si dispersion was added into the mixture of GO and D-glucose. Then, the mixture was sealed in a Teflon-lined autoclave and maintained at a temperature of 180 °C for 12 h.

2.3.2 Material Characterization

The morphology of the composite was investigated by SEM (Hitachi SU8230). HRTEM images were taken on JEOL JEM-2010F field emission electron microscope at an acceleration voltage of 200 kV. The Si content in the sm-Si@C/Gr was measured from the weight loss curve in TGA (PerkinElmer Pyris 1 TGA) with a heating rate of 5 °C min^{-1} under air. The elemental analysis of the composites was characterized by SEM equipped with EDX (Hitachi SU8230) and XPS (Thermal Scientific K-alpha XPS instrument). XRD patterns were measured with Cu Kα radiation in the 2θ range of 10°~80° (X'Pert Pro Alpha). Raman spectrum was collected from 400 cm^{-1} to 2000 cm^{-1} by Thermo Nicolet Almega XR Dispersive Raman Spectrometer (488 nm excitation laser).

2.3.3 Electrochemical Measurement

The sm-Si@C/Gr was mixed with conductive carbon black (MTI Corporation) and sodium carboxymethyl cellulose (Sodium CMC, Sigma Aldrich) binder (weight ratio,

65:12:23) in DI water. The prepared slurry was coated on a copper foil using a doctor blade. The working electrodes were assembled into Swagelok-type cells in a high purity Ar-filled glovebox (MBraun, O_2 and H_2O < 0.1 ppm). 100 μL of 1M $LiPF_6$ in a EC and DMC (volume ratio, 3:7, BASF) with 10 vol% of FEC (Sigma Aldrich) was adopted for the electrolyte. Celgard 2500 was used as a separator. Li metal was employed as the counter/reference electrode. Electrochemical charge storage characteristics of the working electrodes were investigated by CV in the voltage window of 0.01-1.5 V vs. Li/Li^+ with a scan rate of 0.1 mV s^{-1} (Bio Logic VMP3). Rate- capabilities were examined in varied current density values from 0.1 A g^{-1} to 10 A g^{-1}. To investigate cycling stability, the working electrodes were cycled at 1 A g^{-1} without initial stabilization cycles (charging/discharging a cell at low current density). Electrochemical impedance spectroscopy was measured over a series of cycles in a frequency range of 10 mHz – 100 kHz with an amplitude of 10 mV using Bio Logic VM3.

2.4 Results and Discussion

The fabrication process of the submicron Si encapsulated with graphene and carbon (sm-Si@C/Gr) anode is illustrated in **Fig. 2.1**. First, the sm-Si particles were recovered from the Si waste slurry which was generated during the slicing process of Si ingots into Si wafers. The mud-like Si waste slurry mainly contains Si, SiC and metallic impurities in a polyethylene glycol lubricant. After drying the Si waste slurry, it was dispersed in DI water. As the SiC has higher specific gravity than Si, the dispersion can be readily separated into Si-rich supernatant and SiC-rich sediment using a centrifugal force.[90] After drying the Si-rich supernatant part, obtained Si particles were treated with 2M hydrochloric acid to

remove metallic impurities. The recovered Si particles displayed wide size distribution from several hundred nanometers to several micrometers. To homogenize their size distribution, the recovered Si particles were slightly ground using a beads-mill, yielding the sm-Si particles close to 1 μm. The obtained sm-Si particles were dispersed in DI water via sonication. Because Si particles have intrinsic silicon oxide (SiO_x) layers on their surface, the dispersed sm-Si particles exhibit negative surface charge in water.[24, 76] To convert the surface charge of the sm-Si, positively charged polyelectrolyte (PDDA), was added into the sm-Si dispersion. This surface charge inversion process of the sm-Si enables the robust assembly of the positively charged sm-Si particle and negatively charged GO through electrostatic interaction.[74]

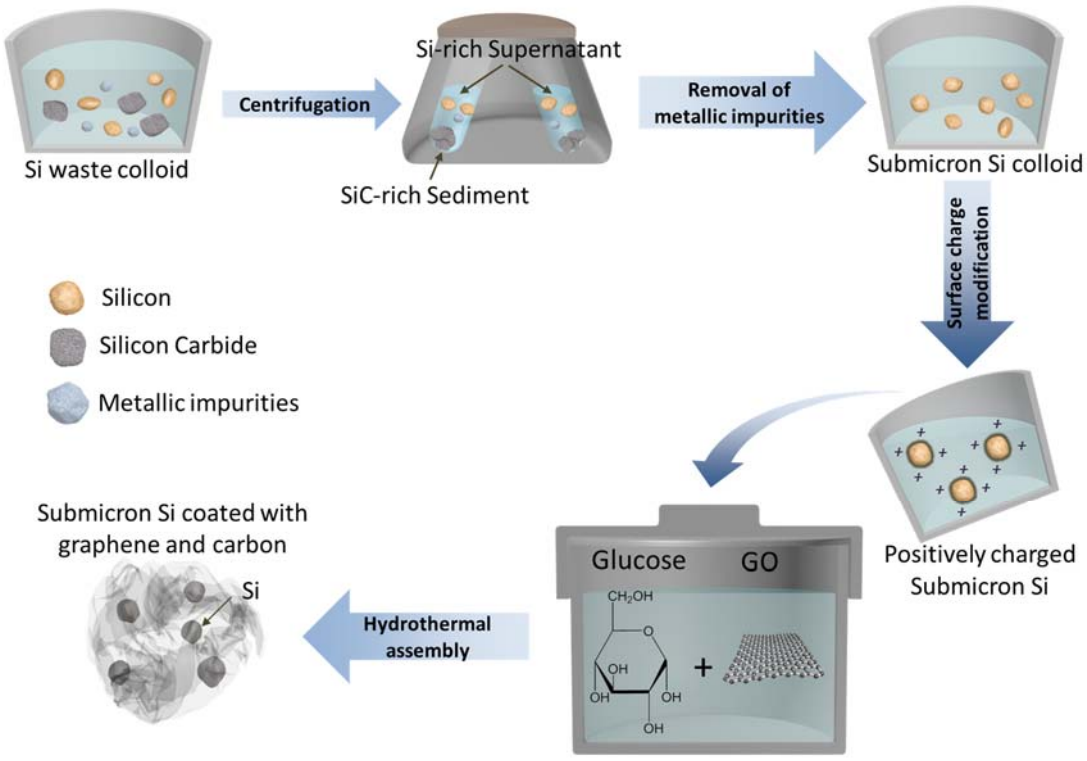

Figure 2.1 Schematic procedure for the preparation of the recovered submicron Si coated with graphene and carbon (sm-Si@C/Gr).

It is noteworthy mentioning that the conversion of the Si's surface charge is critical to enhance the dispersibility. When the sm-Si particles were dispersed in water by sonication, they were largely precipitated after a day due to a higher density of Si with respect to water (**Fig. 2.2a**). Therefore, direct use of the sm-Si particles without its surface charge conversion as a Si source may yield the biased distribution of the sm-Si particles during the fabrication of the composite electrode. On the other hands, the mixture of the positively charged sm-Si particle and GO well maintained their dispersion over a week (**Fig. 2.2b**). This stable dispersion can be attributed to repulsive force among excessive negative charges of the attached GO sheets on the sm-Si, improving colloidal stability.[92] The surface charge modified sm-Si, GO and D-glucose water were mixed in DI water and the mixture was transferred into a Teflon-lined autoclave for hydrothermal assembly. During the hydrothermal process at 180 ºC for 12 h, the GO sheets were reduced and coalesced, while D-glucose was carbonized on the surface of sm-Si.[43, 93] The obtained composite was further reduced through thermal treatment at 450 ºC for 3 h under argon environment, finally producing the sm-Si@C/Gr.

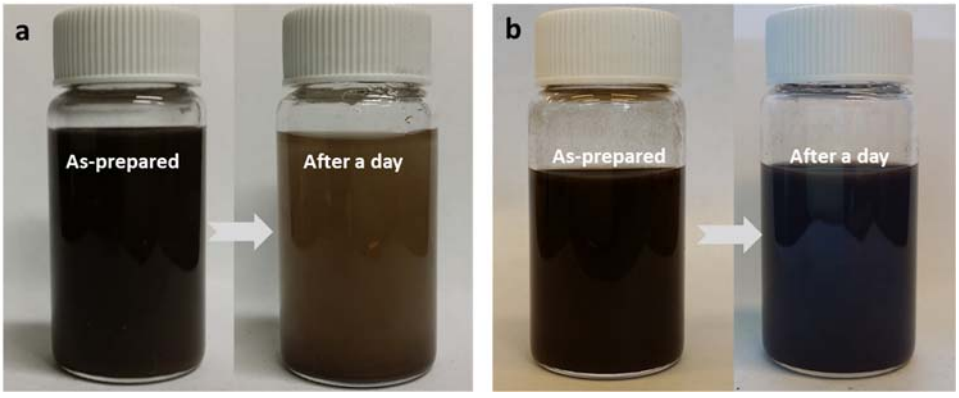

Figure 2.2 (a) As-prepared sm-Si colloid and its precipitation after a day. The color of the colloid was faded. (b) The mixture of the positively charged sm-Si and graphene oxide, showing stable dispersion over a week.

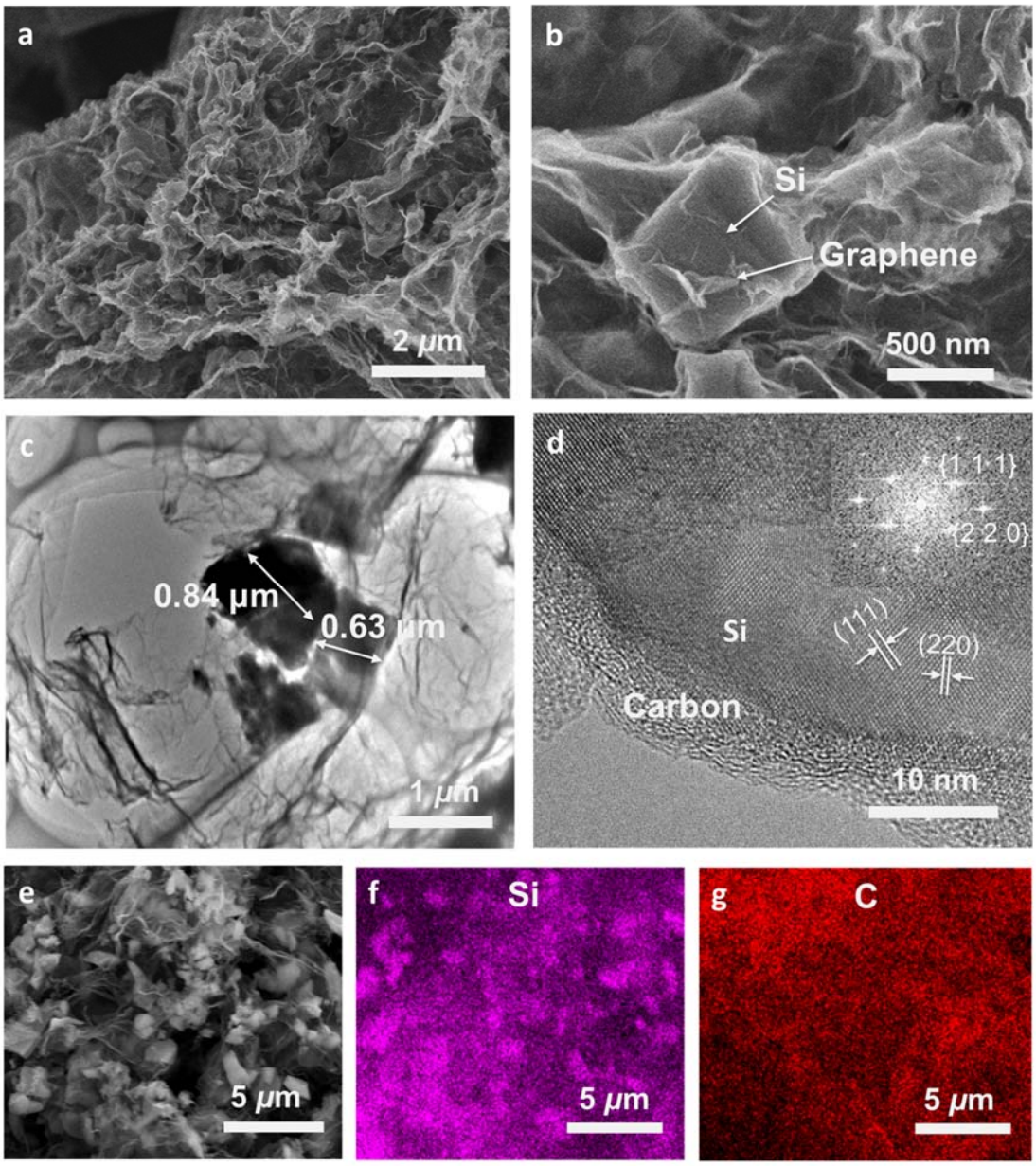

Figure 2.3 (a) Low- and (b) high-magnification scanning electron microscopy (SEM) images of the sm-Si@C/Gr. (c) Low- and (d) high-magnification HRTEM images with the fast Fourier transformation analysis of the sm-Si@C/Gr. (e) SEM image of the sm-Si@C/Gr for energy-dispersive X-ray (EDX) analysis and corresponding elemental mapping of (f) silicon and (g) carbon.

The morphology of the sm-Si@C/Gr was studied by SEM equipped with EDX and HRTEM (**Fig. 2.3**). Low-magnification SEM image showed that graphene sheets were interconnected with each other to form a 3D porous network structure (**Fig. 2.3a**). High-magnification SEM image displayed that the sm-Si particles were well encapsulated by the interconnected graphene sheets (**Fig. 2.3b**). Low-magnification HRTEM image also showed that sm-Si particles with sizes of 840 nm and 630 nm were entirely confined within the graphene layers (**Fig. 2.3c**). Moreover, thin carbon layers, which were derived from the hydrothermal carbonization of the D-glucose, were found from the high-magnification HRTEM investigation (**Fig. 2.3d**). The crystalline structure of the sm-Si in the composite was characterized by FFT analysis and was indexed as the (111) and (220) faces. The measured spacing values of the lattice plane were 0.311 nm and 0.195 nm, which respectively matches with the (111) and (220) planes of the cubic diamond structure of Si.[94] The EDX analysis showed the elemental maps for Si and carbon on the sm-Si@C/Gr (Fig. **2.3e-2.3g**), indicating the homogeneous distribution of the elements within the composite electrode. The EDX map for Si and the corresponding SEM image further exhibited the size distribution of the encapsulated sm-Si particles, showing their particle sizes are close to 1 μm (**Fig. 2.3e**).

The crystal structure of the sm-Si@C/Gr was further confirmed by XRD investigation (**Fig. 2.4a**). The sm-Si@C/Gr displayed a small peak around 24° and two intense peaks at 28.5° and 47.3°. For comparison, a carbon-graphene composite (C@Gr) was also prepared through the same synthetic procedures of the sm-Si@C/Gr without the positively charged sm-Si particles. The C@Gr showed a minute peak around 24°, indicating that this peak is attributed to the amorphous carbon and disordered graphene.[2,

[95] In addition, the pristine sm-Si showed the intense peaks at 2θ = 28.5° and 47.3°, which are corresponding to crystal planes of (111) and (220), respectively.[80] The presented XRD pattern of the sm-Si@C/Gr including characteristic peaks of both the sm-Si and C@gr indicates that the sm-Si@C/Gr consists of pure Si, carbon, and graphene. Calculation with the Bragg's law gave d-spacing of 0.31 nm at (111) plane and 0.19 nm at (220) plane, which are consistent with the TEM results.

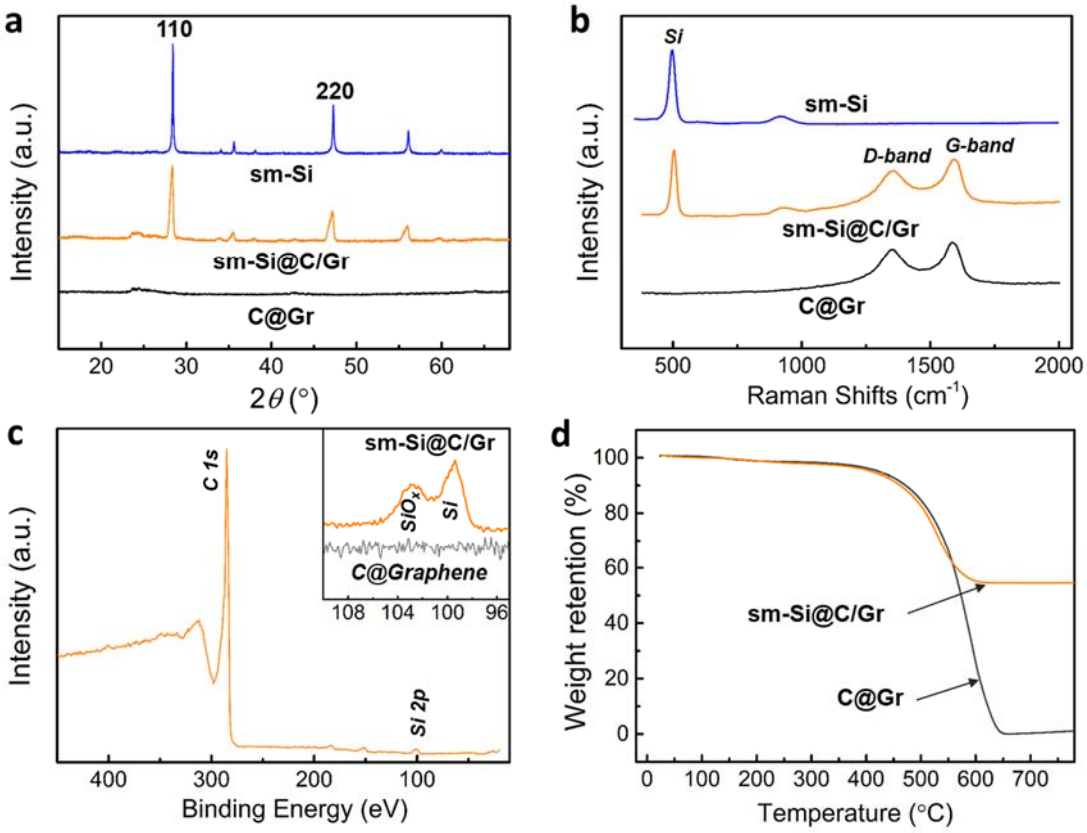

Figure 2.4 (a) X-ray diffraction (XRD) and (b) Raman spectra of the sm-Si, C@Gr and sm-Si@C/Gr. (c) XPS wide scan survey of the sm-Si@C/Gr. The inset shows high-resolution Si 2p spectra of the sm-Si@C/Gr and C@Gr. (d) Thermogravimetric measurements of the sm-Si@C/Gr and C@Gr electrodes in air at a heating rate of 5 °C min^{-1}.

Raman spectroscopy of the sm-Si@C/Gr displayed three characteristic peaks at 497, 1350 and 1592 cm^{-1} (**Fig. 2.4b**). The intense peak at 497 cm^{-1} corresponds to crystal Si.[80] The two broaden bands at 1350 (D-band) and 1592 cm^{-1} (G-Band) are originated from disordered sp^2-carbon and stretching of the C-C bond in graphitic materials, respectively.[73] A wide scan survey of XPS confirmed the coexistence of Si and carbon (**Fig. 2.4c**). The negligible peak of Si 2p in the wide scan survey indicates a low surface atomic percentage of Si due to the graphene and thin carbon layers on outer surface of Si.[80] The high-resolution Si 2p spectrum of the sm-Si@C/Gr displayed two noticeable peaks of Si at 99.4 eV and SiO_x ($x<2$) at 103 eV.[76] To estimate the weight percentage of the sm-Si in the sm-Si@C/Gr, the weight loss curves of the sm-Si@C/Gr and C@Gr were measured by TGA (**Fig. 2.4d**). The weight losses of the sm-Si@C/Gr and C@Gr were initiated around 400 °C and continued till ~650 °C, which is associated with the decomposition of graphene and carbon. The calculated mass percentage of Si in the sm-Si@C/Gr was found to be 58%.

The lithiation/delithiation characteristics of the sm-Si@C/Gr were evaluated using CV at a scan rate 0.1 mV s^{-1} in the voltage window of 0.01-1.5 V vs. Li on a Li half-cell (**Fig. 2.5a**). The first cathodic sweep showed a gentle slope at potential below 1.0 V vs. Li due to the formation of SEI, which is similar to that of the reported Si-C composite.[89] Additionally, a large reduction wave at potential below 0.1 V vs. Li can be attributed to the alloying process of Li and Si, forming amorphous Li_xSi.[76] In the subsequent CV cycles, two anodic bumps at 0.35 V and 0.6 V, and one reduction peak at 0.2 V vs. Li were found, which corresponds to dealloying and alloying of the sm-Si with Li, respectively.[59, 76] It is noteworthy mentioning that the anodic and cathodic peak currents gradually intensified

and approached stable values after 10 cycles. These increased peak currents can be attributed to the gradual kinetic activation of Si upon discharging and charging.[96]

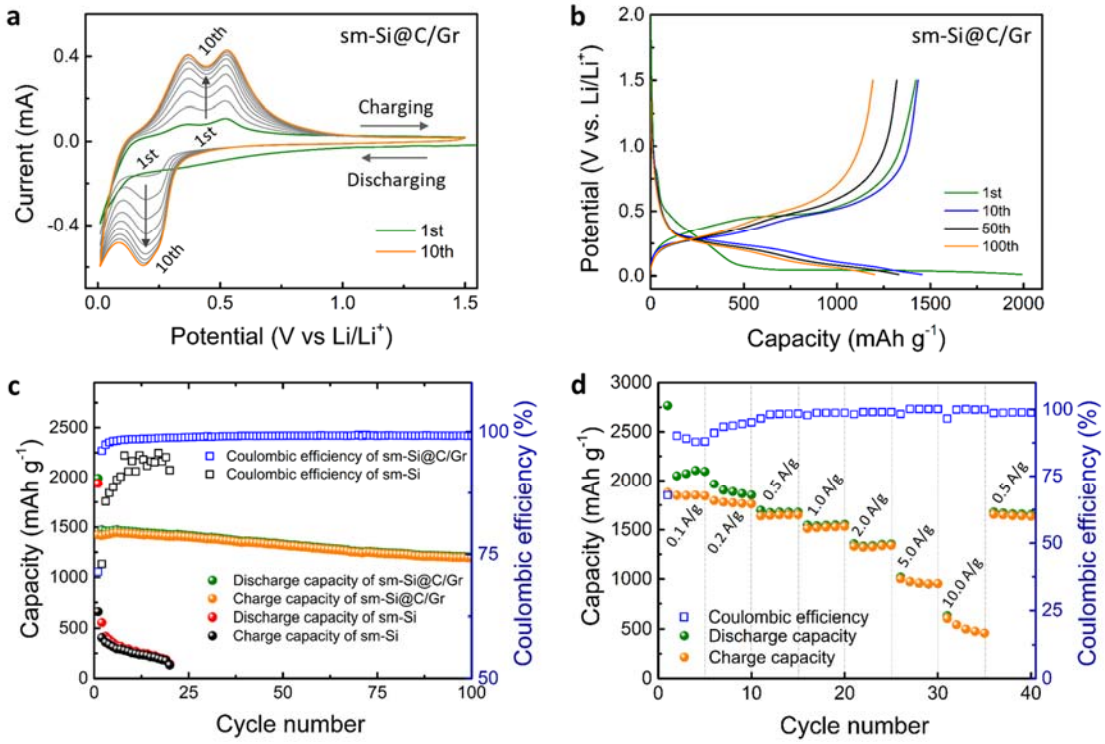

Figure 2.5 (a) CV scans of the sm-Si@C/Gr during 10 cycles at a scan rate of 0.1 mV s^{-1} (b) Galvanostatic discharge and charge profiles of the sm-Si@C/Gr at the current density of 1 A g^{-1} (c) Cycling stability of the sm-Si@C/Gr and pristine sm-Si. (d) Rate-capability of the sm-Si@C/Gr measured at the current densities of 0.1~10 A g^{-1}.

The galvanostatic discharge and charge profiles of the sm-Si@C/Gr electrodes were investigated in the voltage window of 0.01-1.5 V vs. Li/Li^+ at a current density of 1 A g^{-1} (**Fig. 2.5b**). In general, cycling stabilities of Si-based electrodes are investigated after pre-stabilization process[60, 97] by cycling at the low current density in the range of 0.1 – 0.4 A g^{-1}.[48, 80] It should be mentioned that the cycling stability of the sm-Si@C/Gr electrode was directly investigated at 1 A g^{-1} without the pre-slow cycling process. The first discharge

and charge capacities of the composite electrode were 1991 mAh g^{-1} and 1423 mAh g^{-1}, respectively. The capacity loss in the first cycle can be attributed to the formations of the SEI and amorphous Li_xSi.[59, 76] On subsequent galvanostatic cycling, the sm-Si@C/Gr electrode displayed a lithiation plateau at 0-0.2 V and a delithiation plateau at 0.2-0.6 V vs. Li.[59, 80] The charge capacity slightly increased up to 10 cycles owing to the gradual kinetic activation of Si, which is consistent with the CV result. The sm-Si@C/Gr electrodes exhibited excellent cycling stability up to 100 cycles, retaining 84% of its initial charge capacity (**Fig. 2.5c**). The coulombic efficiency of the sm-Si@C/Gr electrode in the first cycle was 71.5%. Upon subsequent galvanostatic cycles, it rapidly approached a high value over 99%.

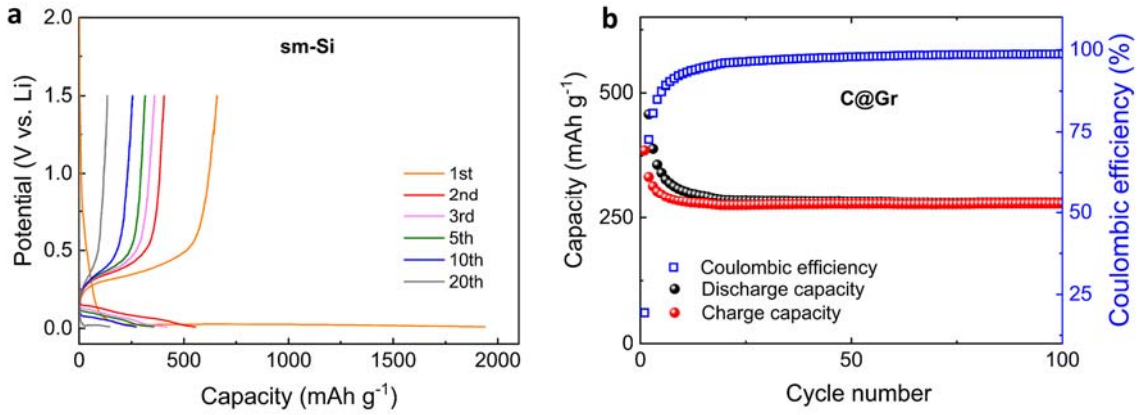

Figure 2.6 (a) Galvanostatic discharge and charge profiles of the pristine sm-Si electrode at a current density of 1 A g^{-1} with a cut-off window 0.01-1.5 V vs. Li. (b) Specific discharge and charge capacity of the C@Gr and corresponding Coulombic efficiencies as a function of cycle number.

When the recovered sm-Si was directly employed as an anode material, the first discharge capacity of the electrode was 1938 mAh g^{-1}, which is comparable to that of the

sm-Si@C/Gr (**Fig. 2.6a**) However, the first charge capacity was just 659 mAh g^{-1} and both charge and discharge capacities rapidly decreased on the subsequent cycles. This can be attributed to the surface crack typically found in Si particles bigger than 150 nm.[62] To estimate the capacity contribution of the sm-Si in the sm-Si@C/Gr electrode, a C@Gr electrode was also cycled at 1 A g^{-1} in the voltage window of 0.01-1.5 V vs. Li/Li^+. The C@Gr electrode delivered a charge capacity of 385 mAh g^{-1} in the first cycle and was quickly stabilized to 277 mAh g^{-1} (**Fig. 2.6b**). Based on the weight percentage of Si (58 wt%) in the sm-Si@C/Gr, the contribution of the sm-Si was calculated as the charge capacities of 2175 mAh g^{-1} and 1855 mAh g^{-1} the 1st and 100th cycle, respectively. The rate-capability of the sm-Si@C/Gr electrode was evaluated at varied current densities from 0.1 to 10 A g^{-1} (**Fig. 2.5d**). The sm-Si@C/Gr electrode well maintained its high gravimetric charge capacities with increased current densities: 1877 mAh g^{-1} at 0.1 A g^{-1}, 1652 mAh g^{-1} at 0.5 A g^{-1}, 1534 mAh g^{-1} at 1 A g^{-1}, and 950 mAh g^{-1} at 5 A g^{-1}. When the current density was redirected back to 0.5 A g^{-1}, the charge capacity of the sm-Si@C/Gr was recovered to 1650 mAh g^{-1}. The cycling stability and rate-capability of the sm-Si@C/Gr electrode are comparable to those of the Si waste utilized reported Si-based electrodes[60, 64-65, 75-78, 98] and definitely highest among all of the recovered Si electrodes[79, 86] (**Table 2.1**).

Table 2.1 Comparison of the electrochemical performances for the various Si-based electrodes.

Materials (Si size)	Synthesis methods	Capacity retention (cycle#)	Capacity (Current density) [mAh g^{-1}]
This work (~ 1 μm)	one-pot assembly	84% (100)	950 mAh g-1 (5 A g^{-1})
Nano Si@G[79] (10-100 nm)	High energy ball mill	73% (150)	< 250 mAh g^{-1} (4.5 A g^{-1})
Crumpled Graphene-Si[75] (50-100 nm)	Aerosol-assisted assembly	83% (250)	700 mAh g^{-1} (4 A g^{-1})
Crumpled Graphene-Si[86] (100 nm)	Aerosol-assisted assembly	~85% (50)	-
3D Graphene-Si[77] (< 6 nm)	Magnesium vapor reduction	83.7% (200)	950 mAh g^{-1} (3.2 A g^{-1})
Si-C yolk shell[64] (100 nm)	Chemical etching	85% (100)	-
Si-rGO-C[60] (70 nm)	Freeze-drying and CVD	94% (300)	770 mAh g^{-1} (2.8 A g^{-1})
Si-Encapsulating Hollow Carbon[65] (100nm)	Electroless etching	< 80% (50)	< 1200 mAh g-1 (4 A g^{-1})
Si/CNF/G[78] (50-100 nm)	Electrospinning	91% (50)	< 600 mAh g^{-1} (1 A g^{-1})
SiNPs@GNS–GrTr[98]	MPECVD	88.6% (50)	< 500 mAh g^{-1} (8 A g^{-1})
Si/RGP[76] (<100nm)	Steam etching	<70% (50)	<1500 mAh g^{-1} (0.2 A g-1)

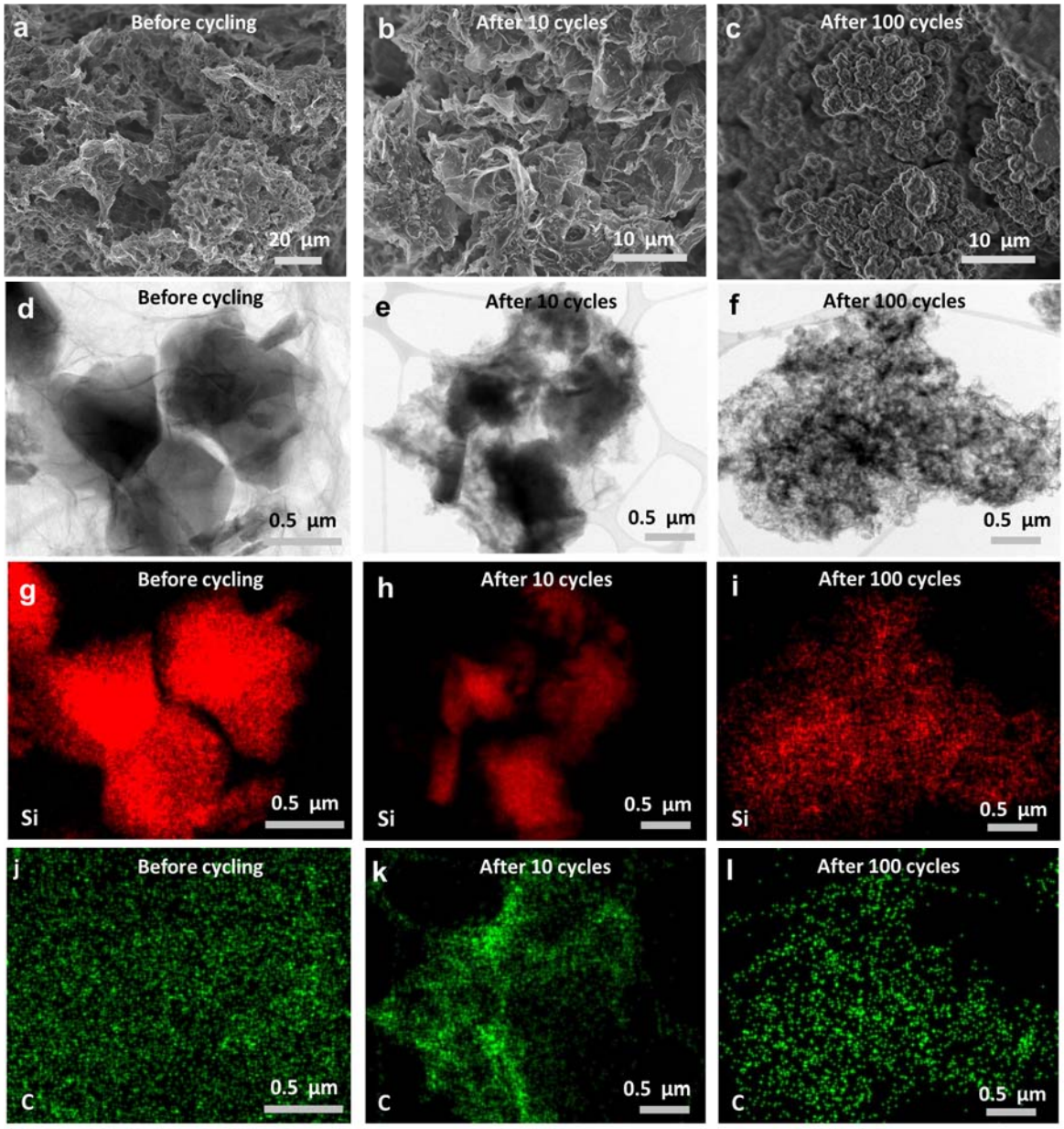

Figure 2.7 Morphology investigation of the sm-Si@C/Gr electrodes before and after cycling. (a, b, and c) *ex-situ* SEM images of the sm-Si@C/Gr electrodes. (d, e and f) *ex-situ* TEM investigation of the sm-Si @C/Gr electrodes. EDX maps of the composites at 0th, 10th and 100th cycles for (g, h and i) Si and (j, k and l) carbon. The cycling was carried out at the current density of 1 A g^{-1} with a cut-off window of 0.01-1.5 V vs. Li.

To understand the role of the graphene and carbon layers for the improved stability, the sm-Si@C/Gr electrodes at 0th, 10th and 100th cycles were analyzed by *ex-situ* SEM and TEM, and compared with the pristine sm-Si electrodes (**Fig. 2.7** and **Fig. 2.8**). Comparison of the SEM images for the sm-Si@C/Gr electrode before and after cycles showed that the 3D carbon network structure was well maintained with the moderate formation of the SEI layer 3D porous structure during cycling (**Fig. 2.7a-2.7c**). The HRTEM images showed that the submicron Si particles in the sm-Si@C/Gr electrodes were pulverized during cycling (**Fig. 2.7d-2.7l**). Despite this pulverization process, the pulverized Si particles were securely encapsulated with the graphene layers, keeping Si particles electrochemically active within the carbon network and preventing their exposure to electrolyte. On the other hand, the sm-Si electrode without the protection of the graphene and carbon showed that the pulverized Si particles were electrically disconnected after 10 cycles (**Fig. 2.8**).

Recent study using waste Si showed that micro-sized Si particles with carbon coating still suffer from low cycling stability with the thick SEI formation.[79] Thus, they employed nano-sized Si particles to improve the cycling stability.[79] This study indicates that only graphene coating on the micro-sized Si particles cannot accommodate the large volume change of the Si during cycling. Thus, the excellent cycling stability of the sm-Si electrode can be attributed to its unique 3D structure consisting of porous graphene network and amorphous carbon layers which effectively encapsulates the Si particles.

To further understand such enhanced electrochemical performance of the sm-Si@C/Gr electrodes, EIS was employed (**Fig. 2.9**). The Nyquist plot of the sm-Si@C/Gr electrodes consist of two semicircles and a low-frequency tail. Using the equivalent circuit

model, we can evaluate the SEI resistance (R_{SEI}) that indicates the ionic diffusion resistance of Li ions in the SEI layer.[60, 99] The calculated R_{SEI} values of the sm-Si@C/Gr were 75 and 92 Ω after 1st and 10th cycles, respectively. On the other hands, the pristine sm-Si electrode showed a higher R_{SEI} value of 2033 Ω after 1st cycle and this was immensely increased to 9199 Ω after 10th cycle, indicating a large R_{SEI} as well as its fast increase during cycling. This comparison shows the fast surface kinetics of the sm-Si@C/Gr with the effective suppression of the SEI layer formation, further confirming the effective roles of the 3D carbon network surrounding sm-Si particles.

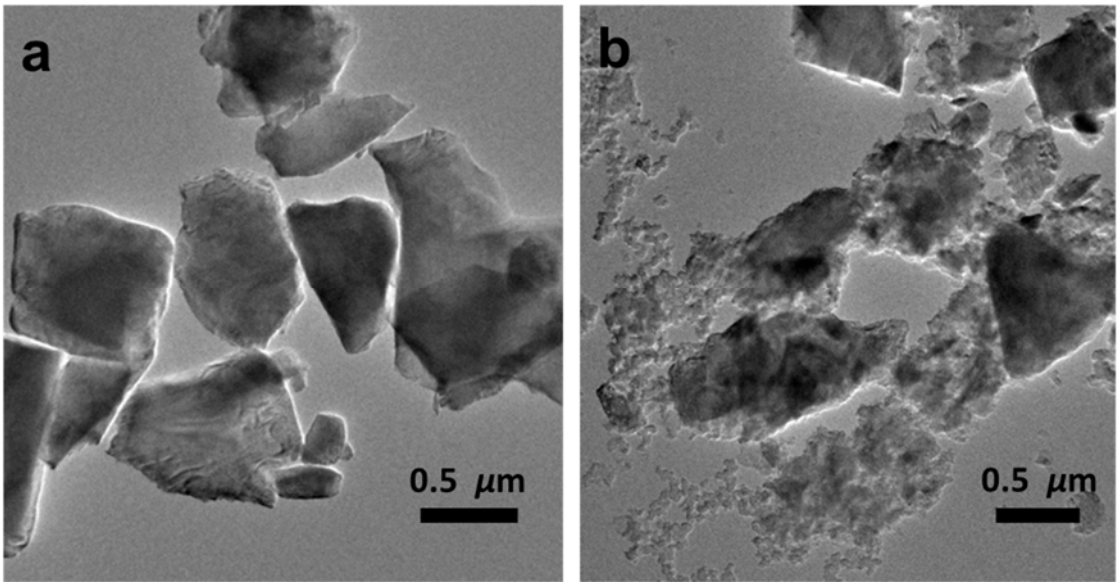

Figure 2.8 *ex-situ* HRTEM images of the bare submicron Si. (a) Submicron Si particles before cycling. (b) Pulverized Si particles after 10 cycles. The cycling was carried out at current density of 1 A g^{-1} with a cut-off window 0.01-1.5 V vs. Li.

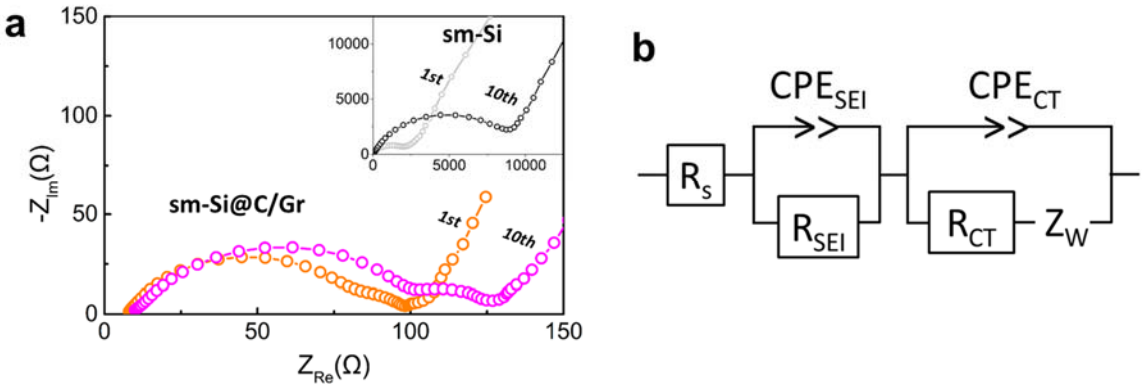

Figure 2.9 Electrochemical impedance spectroscopy of the sm-Si@C/Gr (a) Nyquist plot after the 1st and 10th cycles. (Inset: Nyquist plot of the pristine sm-Si electrode). (b) Equivalent circuit model comprised of electrolyte resistance (R_S), SEI film resistance (R_{SEI}), charge transfer resistance (R_{CT}), and Warburg diffusion impedance (Z_W).

2.5 Conclusions

In conclusion, we revealed that sm-Si particles recovered from Si waste can be fabricated as a high-performance anode for LIBs. From the versatile hydrothermal assembly, sm-Si particles were securely encapsulated with multilayer carbon network including both carbon coating and three-dimensional porous graphene. Despite their large sizes of sm-Si particles, the composite electrodes exhibited excellent cycling stability, retaining 84% of the initial capacity at the 100th cycles. In addition, they showed high rate-capability of 950 mAh g^{-1} at 5 A g^{-1} owing to the carbon network, which is comparable to or even higher than nano-sized Si anodes. We further revealed that the pulverized sm-Si particles upon cycling were securely encapsulated within the carbon network, which can maintain their charge storage capability during cycling. Our design approach based on Si waste and simple fabrication process suggests a scalable route for developing cost-effective and high-performance anodes for LIBs.

CHAPTER 3.

GRAPHENE AS A TWO-DIMENSIONAL TEMPLATE

Reproduced from Tianyuan Liu, Byeongyong Lee, Michael J. Lee, Jinho Park, Zhongming Chen, Suguru Noda and, Seung Woo Lee, Improved capacity of redox-active functional carbon cathodes by dimension reduction for hybrid supercapacitors. J. Mater. Chem. A., 2018, **6**, 3367-3375. Royal Society of Chemistry specifies that permission request for reproduction if the reproduction is for thesis.

3.1 Overview

Various ACs have been adopted as a capacitor-type cathode for HSC due to their high electrical conductivity and large surface area.[14] However, the poor capacity of activated carbon cathodes (~38 mAh g^{-1})[100] which is much lower than intercalation-type anodes, has limited the energy density of the HSC system. As such, much effort has been devoted to increasing the capacity of ACs by tailoring the pore structure or by doping with heterogeneous atoms such as nitrogen and oxygen.[101-102] These strategies have increased the capacity of ACs (71~120 mAh g^{-1}), but is still much lower than the counter anodes.[102] Furthermore, under the unbalanced capacities, high-mass loading cathode is required. Thus, it is imperative to develop a high-capacity cathode, in particular a thick electrode with high areal mass loading, in order to improve the performance of HSCs.[103]

The synthesis of AC materials requires complex chemical treatments and high-temperature heating processes.[14, 104] Therefore, it is desirable to simplify the synthesis processes of carbon electrodes based on the sustainable source such as naturally grown

biomass. Heat treatment of an aqueous solution of saccharides, such as glucose and sucrose, in a closed container at a moderate temperature (150-350 °C) produces carbonaceous microspheres containing copious surface oxygen functional groups, so-called hydrochars.[105-106] This process, called HTC, has been studied since the early 20th century to understand coal formation mechanisms.[105] Recently, HTC has received new attention due to its versatility to synthesize functional carbon materials for environmental, catalytic, biological, and electrochemical applications.[106] Recent studies on HTC have focused on controlling the physical and chemical structures of the hydrochars, and also synthesizing hybrid materials with various metal nanoparticles.[107-108] However, the resulting carbonaceous products could not be used as active electrode materials for energy storage applications due to their insulating property. Recently, we have fabricated a composite electrode composed of the CSs produced by HTC of glucose and conductive carbon nanotubes (CNTs).[109] In the conductive CNT network, CSs showed redox reactions between the surface oxygen functional groups and Li-ions in the voltage of 1.5-4.5 V vs. Li/Li^+. Utilizing the redox reactions, these CS based electrodes exhibited high capacities of ~153 mAh g^{-1}, but their capacity enhancement was not significant compared to the previously reported AC based cathodes.

3.2 Approach

Recently, 2D heterostructured materials prepared by combining conductive graphene sheets[110] and various redox-active nanosheets have been studied for energy storage applications.[110-111] These 2D systems can take the advantage of improved kinetics for electrochemical charge storage reactions due to the easy transport of electrons and ions

compared to the bulk 3D intercalation-type electrode.[111] Herein, we envision that integrating the redox-active carbonaceous product into a controlled 2D structure. We prepared a heterostructured two-dimensional functional carbon (TDFC) by a simple HTC of biomass (glucose) at a mild temperature (200 °C) and GO was used as two-dimensional template. The physical and chemical structures of the carbonaceous product can be manipulated by adjusting the concentration of the GO templates. The TDFC exhibits a very high capacity of ~250 mAh g^{-1} in a Li-cell, which is significantly higher than those of the hydrothermally synthesized CS (~153 mAh g^{-1}) and modified AC (~120 mAh g^{-1}) [101]. Even with a commercial level mass-loading of ~9.3 mg/cm^2, TDFC maintains a high capacity of ~243 mAh g^{-1} in a Li-cell. The hybrid supercapacitor, which consists of the high-mass loading TDFC cathode and Si-based anode, delivers a high-energy density of ~182 Wh/kg at a high-power density of 1 kW kg^{-1} and maintain its performance over 3,000 cycles.

3.3 Experimental Methods

3.3.1 Material Preparation

Graphene oxide (GO) was synthesized by the Modified Hummer's method. To prepare the two-dimensional functional carbon sheets (TDFC-X), D-(+)-Glucose (Sigma Aldrich) of 3 mg mL^{-1} was mixed with GO of 0.X mg mL^{-1} (X= 1 or 5) in deionized (DI) water by short sonication for 10 min. The glucose solution with the GO templates was then sealed in a Teflon-lined autoclave for the template-assisted hydrothermal carbonization at 200 °C for 18 h. After the autoclave was naturally cooled down to room temperature, carbonaceous products (TDFC-X) were collected by filtration. Carbon spheres (CSs) were also synthesized by the same process to the TDFC without GO.

The Si-based anode was prepared by hydrothermal assembly of Si nanoparticle and GO. In brief, Si nanoparticles (US Research Nanomaterials, Inc, 50-70 nm) were dispersed in DI water (10 mg mL^{-1} of Si nanoparticle dispersion) and then, 0.1 mL of Poly (diallyldimethylammonium chloride) was added into the Si nanoparticle dispersion to convert change the surface charge from negative to positive. 3 mL of the Si nanoparticle dispersion was added into 30 mL of 2 mg mL^{-1} GO dispersion. The mixture of the Si nanoparticle and GO was hydrothermally assembled at 180 ºC for 12 h. After the hydrothermal reaction, the obtained hydrogel (Si/RGO) was freeze-dried subsequent thermal annealing at 450 ºC for 3.5 h under Ar environment.

3.3.2 Material Characterization

The microstructures of the carbonaceous products and composite films were characterized using SEM (Hitachi SU8010, operated at 5 kV), TEM (Hitachi HT7700, operated at 120 kV), and AFM (Veeco AFM). The Raman spectra of carbon materials were collected by a Thermo Nicolet Almega XR Dispersive Raman Spectrometer using a 488-nm wavelength laser. FTIR spectra were measured by Thermo Scientific Nicolet iS50 at ATR mode. XPS (Thermal Scientific K-alpha XPS instrument) was employed to analyze the chemical composition of the carbon materials. High-resolution C 1s peaks were fitted using XPSPEAKS 4.1 software. Electrical conductivities of the films were measured by a standard four-point probe configuration (Signatone). TGA of carbon materials was carried out by Q600 TGA/DSC in a temperature range of 50~700°C under air environment with a ramping rate of 5°C min^{-1}.

3.3.3 Electrochemical Measurement

TDFC-X or CS were mixed with few-walled carbon nanotubes (CNTs, 30 wt%) [112] by a sonication. Then vacuum-filtration was performed to prepare free-standing TDFC-X and CS electrodes. In this structure, the CNTs serve as internal current collectors to enable electron transport to the carbonaceous products. The films were dried in a vacuum oven at 70 °C overnight before use. The densities of electrodes were 0.30~0.4 g cm^{-3}. Loading densities of the prepared electrodes were 2.7~9.3 mg cm^{-2} based on the mass of the carbonaceous products. Two-electrode type Swagelok cells were used for electrochemical measurements. Both Li- and Na-cells were assembled in an Argon-filled glovebox (MBraun). The free-standing TDFC (or CS) electrode and a piece of Li (or Na) were used as cathode and anode, respectively. The separators for Li-cells are two pieces of Celgard 2500, while a piece of glass fiber membrane (Whatman) was used for Na-cells. 1 M $LiPF_6$ in a mixture of EC and DMC (3:7 volume ratio, BASF) was used as an electrolyte for Li-cells and 1 M $NaPF_6$ in EC:DMC (3:7 volume ratio) was used as electrolyte in Na-cells. The voltage window was kept at 1.5-4.5 V vs. Li for Li-cells and 1.3-4.2 V vs. Na for Na-cells, respectively. Current densities were controlled from 0.05 to 5 A/g during the rate-dependent GCD tests. At each end of charging and discharging, the voltage was held for 30 min at either 4.5 V or 1.5 V vs. Li for Li-cells (4.2 V or 1.3 V vs. Na for Na-cells). The cycling stability of the carbon electrodes was tested *via* an accelerated cycling method up to 10,000 cycles based on previous reports.[113-114] The measurement current density was 0.1 A g^{-1} and cycling current density was 10A g^{-1}. Capacitance and capacity in half-cells were normalized by the mass of carbonaceous products (TDFC-X or CS). EIS measurement was performed in the frequency range of 10 mHz-100 kHz with a voltage amplitude of 10 mV.

For the full-cell assembly, the Si anode was prepared by mixing 82 wt% of the Si/RGO with super P carbon black as a conductive additive and sodium carboxylic cellulose as a binder. The Si/graphene electrode was assembled with a piece of Li metal and then, pre-lithiated to 0.03 V vs. Li in 1M $LiPF_6$ in EC:DMC with 10% FEC additive. The lithiated Si electrodes were employed as counter electrodes for TDFC-1 electrodes.

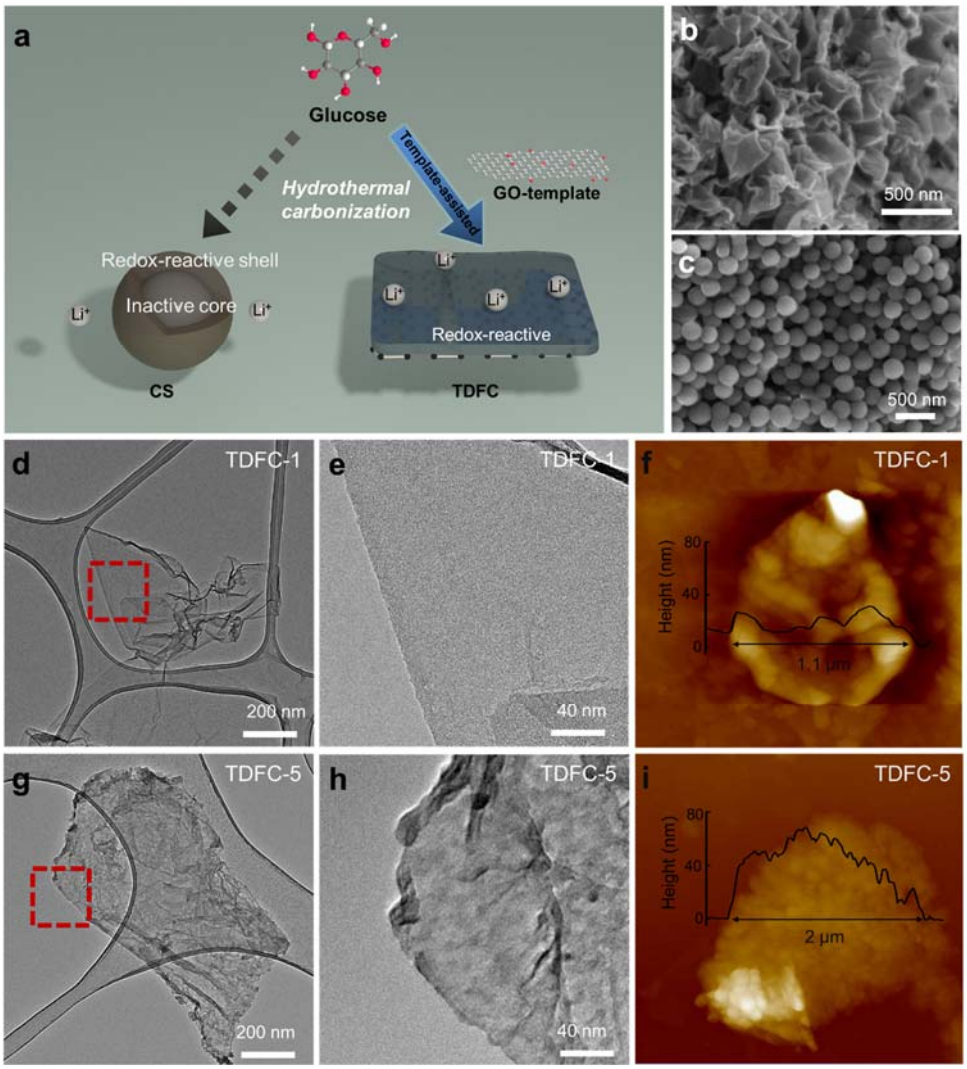

Figure 3.1 Schematic illustration and morphology characterization of TDFC. (a) Schematic preparation of TDFC via template-assisted HTC process of glucose. SEM images of (b) TDFC and (c) CS. TEM investigation of (d, e) TDFC-1 and (g, h) TDFC-5. AFM of (f) TDFC-1 and (i) TDFC-5.

3.4 Results and Discussion

The general HTC process of saccharides undergoes dehydration, condensation, polymerization and aromatization reactions through a self-nucleation, producing carbonaceous microspheres.[105-106, 109] Assuming that the redox reactions take place at the surface oxygen functional groups,[115] we cannot efficiently utilize the bulk core of the carbon spheres for the redox reactions (**Fig. 3.1a**). Therefore, in order to utilize the surface redox reactions effectively, we synthesized ultra-thin TDFC by a template-assited HTC process of glucose. The GO sheets (0.1 or 0.5 mg mL^{-1}) were dispersed as 2D templates in an aqueous solution of glucose (3 mg mL^{-1}). While the glucose solution was transparent, the mixture of glucose and GO templates showed a light yellow color similar to the GO dispersion (**Fig. 3.2**). After a hydrothermal reaction at 200 ºC for 18 h, the color of the GO dispersion (0.1 mg mL^{-1}) turned black without appreciable precipitation. In contrast, the glucose solution and the mixture of glucose and GO templates were converted to brown dispersions with many precipitates (**Fig. 3.2**). The precipitates represent the formation of carbonaceous materials under the hydrothermal condition. Scanning electron microscopy (SEM) images reveal the morphologies of the synthesized carbonaceous products (**Fig. 3.1b,c**). The carbonaceous product obtained from the pristine glucose solution showed typical CSs having a size of 80~200 nm. On the other hand, we observed the planar shape of the carbonaceous products obtained from the mixture of glucose and GO template. This transition indicates that a small amount of GO plays a crucial role in the nucleation and growth of the carbonaceous product, generating the TDFC on the GO.[93] We labeled the TDFC as a function of the GO concentration (TDFC-X), where X indicates the concentration of the GO template (0.X mg mL^{-1}, X=1 or 5).

Figure 3.2 Digital images before and after the hydrothermal carbonization process. Before the hydrothermal reaction, GO (0.1 mg mL^{-1}, top left), glucose (3 mg mL^{-1}, top middle), and the mixture of GO and glucose (top right) displayed transparent colors.

The morphologies of the TDFC-X were investigated by TEM andAFM. At a low GO concentration of 0.1 mg mL^{-1}, the synthesized TDFC-1 showed a smooth and thin carbon film similar to GO surface (**Fig. 3.1d-f**). The AFM height profile of the individual TDFC-1 was found to be 15~30 nm, which is higher than GO (~2 nm) (**Fig. 3.3**). Assuming the uniform deposition of TDFCs on both sides of the GO surface, the thickness of the TDFC is only about 7~15 nm, which is significantly reduced dimension compared to that of the CS (80~200 nm). As the concentration of GO increased to 0.5 mg mL^{-1}, the thickness of the TDFC-5 increased and its surface became rougher (**Fig. 3.1g-i**). We postulate that an excess amount of the GO template can lead to self-assembly of the RGO sheets, which may result in non-uniform nucleation and growth of the carbonaceous product on the stacked RGO substrates. The previous study showed that monolithic gel is formed by self-

assembly of the RGO during the HTC process when the concentration of GO is high enough (1~2 mg mL^{-1}), [93] supporting the rough morphology of the TDFC at high GO concentrations.

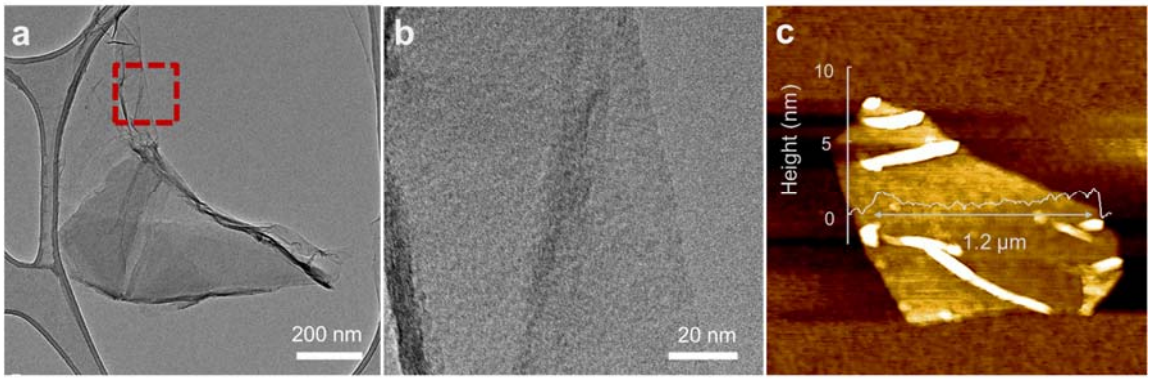

Figure 3.3 Morphology characterization of GO. TEM images of GO at (a) low and (b) high magnification. (c) AFM image of GO. GO shows planar morphology and thin thickness of ~2 nm.

The chemical and physical structure of TDFC and CS was investigated by various techniques, including XPS, FTIR spectroscopy, XRD, Raman spectroscopy and TGA. XPS wide scan survey was used to compare the atomic ratio of oxygen to carbon (O/C) of the carbon materials (Fig. 3.4). GO powder showed the highest O/C ratio of 0.5 and the ratio decreased to ~0.12 after the hydrothermal process. The CS, prepared without the GO templates, showed a high O/C ratio of ~0.32. The ratio gradually decreased to 0.21 (TDFC-1) and 0.18 (TDFC-5) as the concentration of the GO-template increased. The surface oxygen chemistries of the carbonaceous products were investigated by high-resolution C 1s spectra fitted by five carbon peaks: sp^2-hybridized carbon at 284.5 eV, sp^3-hybridized carbon at 285.2±0.2 eV, -C-O at 286±0.2 eV, -C=O at 286.9±0.2 eV, and -COOH or -

COOR at 288.9±0.2 eV (Fig. 3.5a-d).[116] The portion of sp^2-hybridized carbon gradually increased from CS to TDFC-5, while the amount of surface oxygen functional groups decreased with increasing GO-template concentration. Consistent with the XPS results, the FTIR spectra also showed various oxygen functional groups, including -OH (3000-3700, 1020 cm^{-1}), -C=O (1710 cm^{-1}), and -COOH (1620 cm^{-1}) (Fig. 3.6). CS showed clear –OH band peak at 3400 cm^{-1}. The TDFCs showed a significantly reduced peak intensity for -OH (3000-3700 cm^{-1}), indicating that the GO-template can promote the formation of hydrocarbon.[105]

The XRD patterns of the GO powder displayed a sharp peak at 10.4°, which corresponds to (002) diffraction with an interlayer distance of 0.85 nm. This peak was broadened and shifted to ~25° corresponding to an interplanar spacing of 3.56 Å as the GO was hydrothermally reduced to RGO (**Fig. 3.7**).[117] This broad peak of RGO is due to the poorly ordered graphene layers along the stacking direction.[118] The TDFC and CS also displayed a broad peak around 25°, but the TDFCs showed slightly sharper peak than that of the CS due to the incorporated RGO. Raman spectra of the carbon materials exhibited two characteristic peaks at ~1380 cm^{-1} (D band) and ~1600 cm^{-1} (G band) (**Fig. 3.5e**).[119] The G band of the carbonaceous products corresponds to E_{2g} mode of graphite and sp^2 stretch vibration, while the D band attributes to A_{1g} breathing mode of benzene or condensed benzene regions in amorphous carbon.[105] Thus, these bands on both CS and TDFC indicate the formation of small aromatic clusters during the HTC process of glucose. The TGA weight loss curves of the carbon materials were compared in **Fig. 3.5f**. The maximum weight loss temperature[120] was found to increase from 425 °C for CS to 490 °C for TDFC-5 as the concentration of GO-template increased. This indicates the enhanced

thermal stability of the TDFCs compared to CS due to the enhanced carbonization and increased amount of the graphitic carbons.

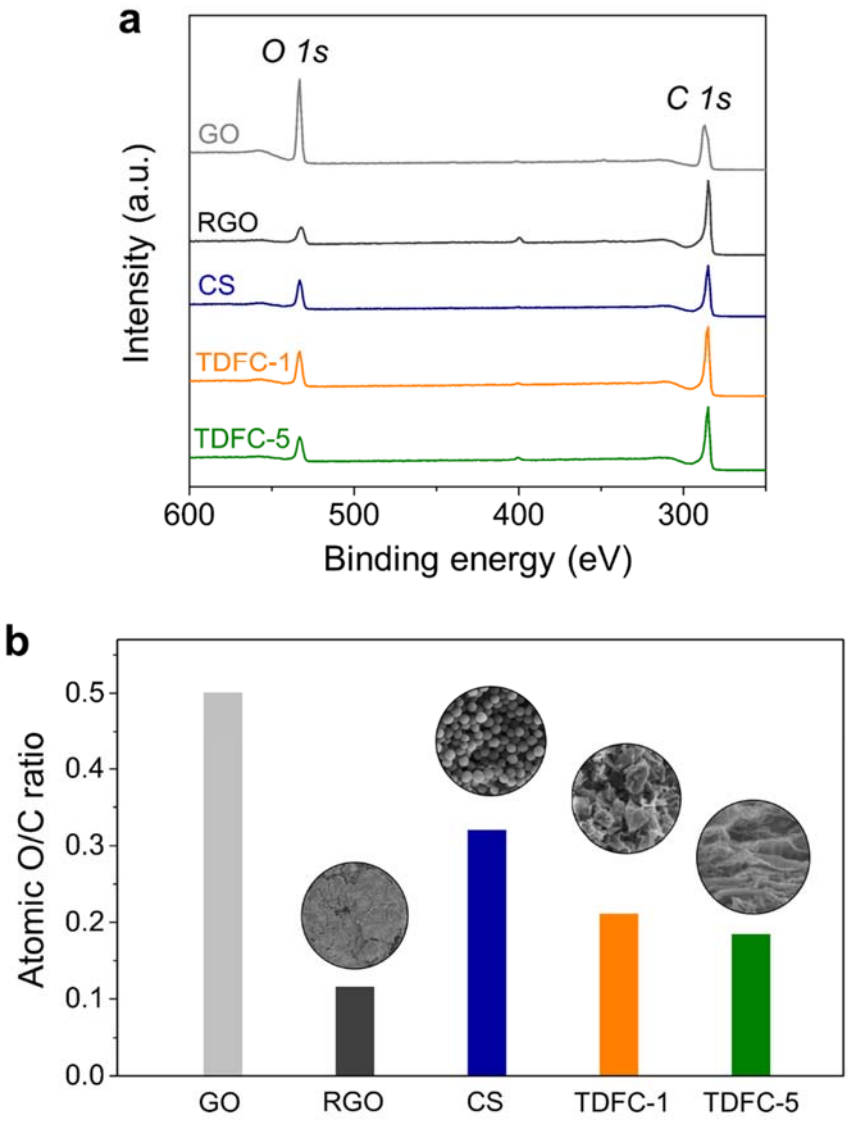

Figure 3.4 XPS characterization of TDFCs and CS. (a) Wide scan surveys and (b) atomic O/C ratios of the carbonaceous products.

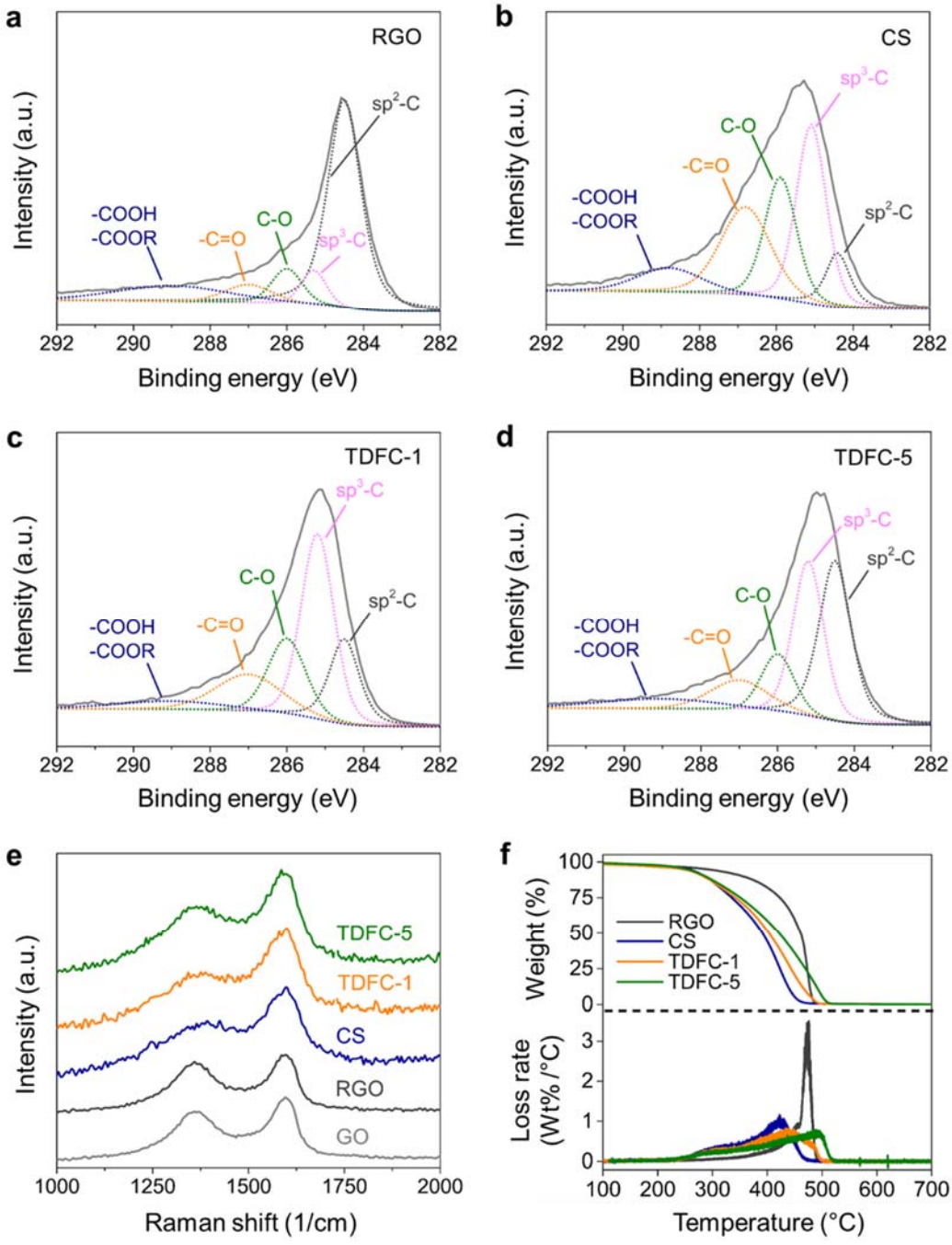

Figure 3.5 Various characterization of the carbonaceous products. High-resolution C 1s spectra of (a) RGO, (b) CS, (c) TDFC-1 and (d) TDFC-5. (e) Raman spectra investigation of the carbonaceous products. (f) TGA of the various carbonaceous products at ramping rate of 5°C min^{-1} (top: weight loss, bottom: weight loss rate).

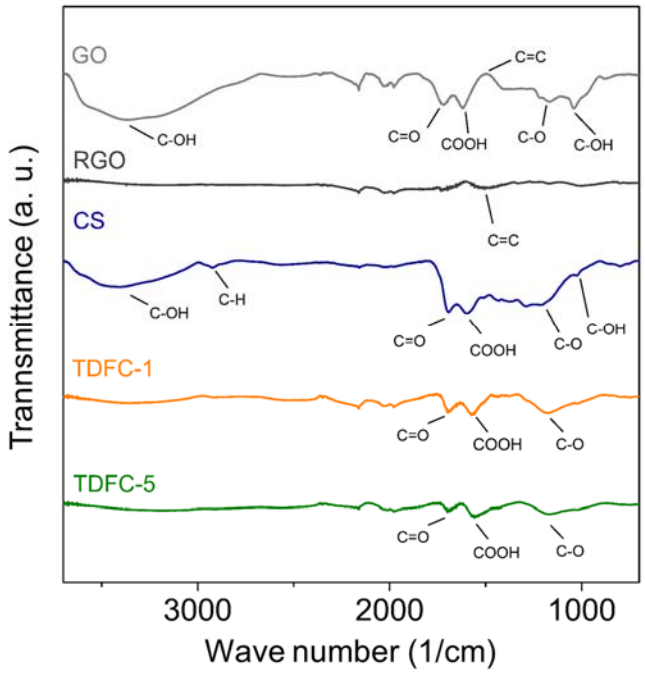

Figure 3.6 Fourier transform infrared (FT-IR) spectra of the various carbonaceous products.

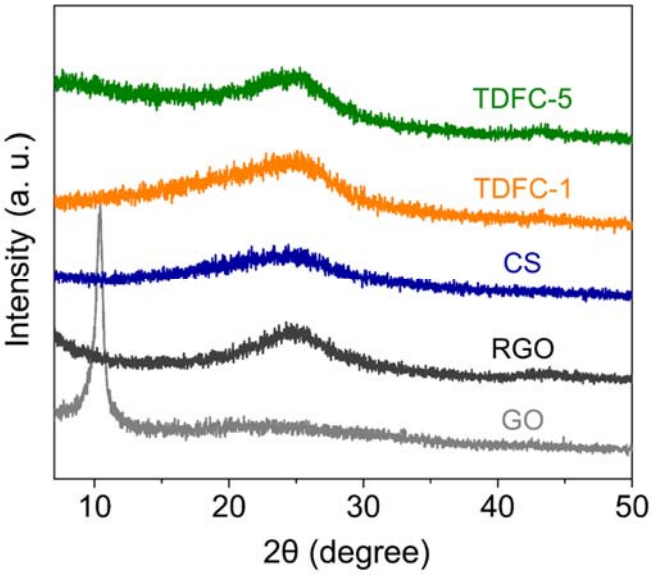

Figure 3.7 XRD investigation of the carbonaceous products.

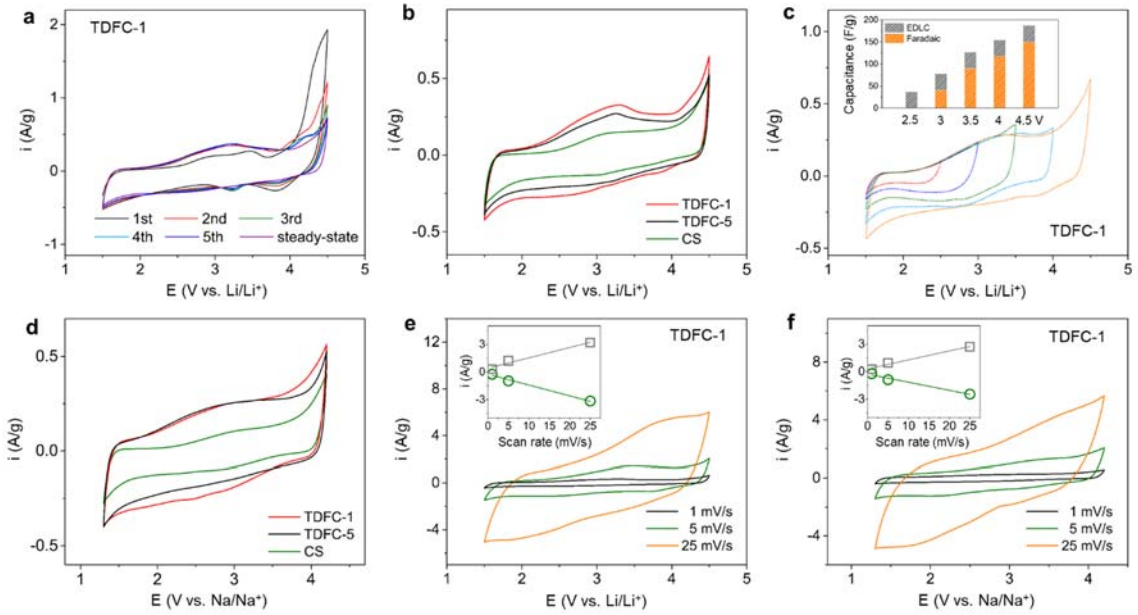

Figure 3.8 Electrochemical characterization of TDFC by cyclic voltammetry. (a) Initial CV scans of TDFC-1 at 1 mV s^{-1}. (b) Steady-state CV scans of CS, TDFCs at 1 mV/s in Li-cells. (c) Potential-dependent CV scans of TDFC-1. (Inset: estimated contributions of Faradaic capacitance and electrical double layer capacitance). (d) Steady-state CV scans of TDFC-1 and CS at 1 mV s^{-1} in Na-cells. Rate-dependent CV scans of TDFC-1 in (e) Li- and (f) Na-cells. Insets in (e) and (f) are anodic and cathodic currents of TDFC-1 in Li- and Na-cell, respectively.

To investigate the charge storage characteristics of the carbonaceous products, free-standing electrodes were prepared by filtering an aqueous dispersion of the TDFCs (or CSs) and sub-millimeter long few-walled CNTs. CV measurements were carried out in the voltage range of 1.5-4.5 V vs. Li for Li-cells and 1.3-4.2 V vs. Na for Na-cells (**Fig. 3.8**). The first forward CV scans of the TDFC and CS electrodes showed a broad oxidation peak centered at ~3.2 V vs. Li and a subsequent oxidation wave at the onset potential of ~4 V vs. Li (**Fig. 3.8a** and **Fig. 3.9**). The oxidation wave in the high potential region can be attributed to the anodic polymerization of the polycyclic aromatic hydrocarbons in the carbonaceous products.[121] The oxidation wave gradually decreased to steady-state in

several cycles and the stable redox peak was developed around 3.2 V vs. Li, which can be ascribed to the redox reactions between oxygen functional groups and Li ions.[113-114] A recent density functional theory (DFT) computation study on reduced graphene oxide have showed that the carbonyl group among various oxygen functional groups has the highest redox potential of ~3 V vs. Li.[122]

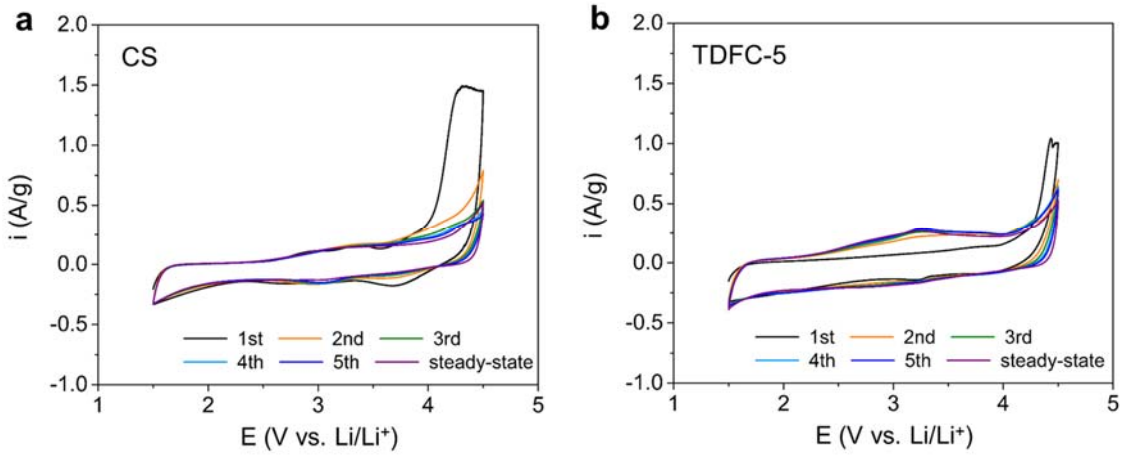

Figure 3.9 Electrochemical characterization of CS and TDFC-5 by cyclic voltammetry (CV) scans in Li-cells. Initial and steady-state CV scans of (a) CS and (b) TDFC-5 at 1 mV s^{-1} in Li-cells. CV scans were carried out in the voltage range of 1.5-4.5 V vs. Li.

The TDFC-1 exhibited the highest capacitance of ~196 F g^{-1}, which is almost 2-fold higher than that of the CS (~109 F g^{-1}) (**Fig. 3.8b**). The enhanced capacitance of the TDFC indicates that the 2D thin film structure of the oxygen-rich carbonaceous material allows a more efficient utilization of the redox reactions than the larger spherical product due to the reduced diffusion length of the electrolyte ions into the redox-active region. In addition, the higher capacitance of the TDFC-1 (~196 F g^{-1}) compared to that of the TDFC-5 (~163 F g^{-1}) may be attributed to the higher concentration of the redox-active oxygen

functional groups. Potential dependent CV measurement was performed to estimate the contribution of redox reactions to the overall capacitance of the TDFC-1 (**Fig. 3.8c**). In the low potential region of 1.5-2.5 V vs. Li/Li^+, the CV scan of TDFC-1 showed a low capacitance of ~37.2 F g^{-1}. The box-like CV shape indicates that the charge storage in this low potential region is mainly due to double layer capacitance.[113] As the potential window sequentially increased from 1.5-2.5 to 1.5-4.5 V vs. Li, the redox peaks were progressively developed in the CV scans. Assuming a constant double layer capacitance, which was measured in the potential region of 1.5-2.5 V vs. Li, the estimated contribution of redox reactions was found to be ~80% maximum.

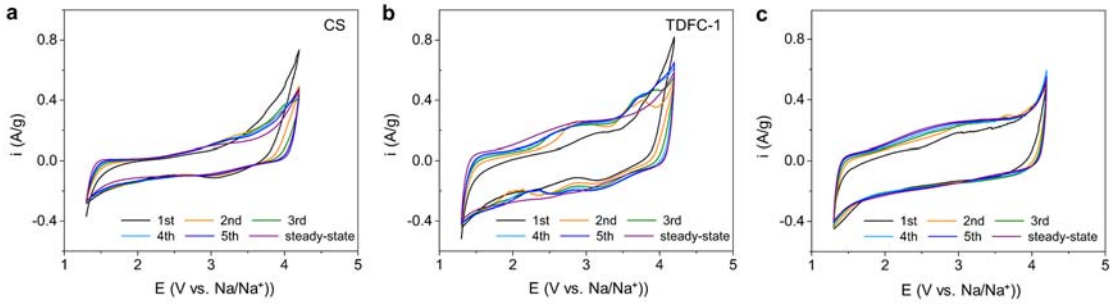

Figure 3.10 Electrochemical characterizations of the CS and TDFCs by cyclic voltammetry (CV) scans in Na-cells. Initial and steady-state CV scans of (a) CS, (b) TDFC-1 and (c) TDFC-5 at 1 mV s^{-1} in Na-cells. CV scans were carried out in the voltage range of 1.3-4.2 V vs. Na.

Similar to the CV results in Li-cells, the TDFC-1 and CS electrodes exhibited the oxidation wave at the high potential region during the first scan and subsequent stable redox peak around ~2.9 V vs. Na/Na^+ in Na-cells (**Fig. 3.10**). Interestingly, the redox peaks in Na-cells are relatively broader than those in Li-cells, which may be due to the larger size of Na-ions than that of Li-ions.[113] The TDFC-1 also exhibited a considerably higher

capacitance of ~196 F g^{-1} than that of the CS (~85 F g^{-1}) in Na-cells (**Fig. 3.8d**). Moreover, the redox characteristic of the TDFC-1 was well preserved up to a high scan rate of 25 mV s^{-1} in both Li- and Na-cells (**Fig. 3.8e,f**). The anodic and cathodic currents measured at 3.2 V in Li-cells and 3.0 V in Na-cells were found to increase linearly with the scan rates, indicating surface-controlled redox processes.[113]

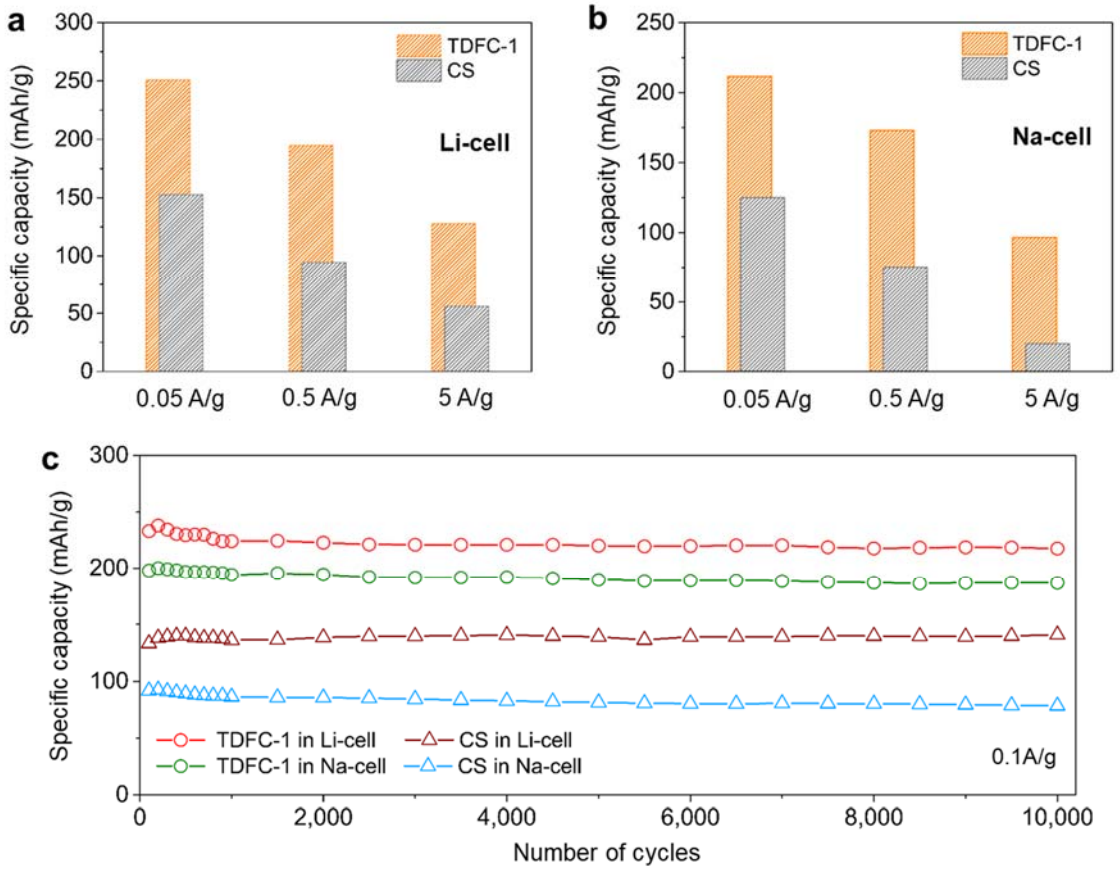

Figure 3.11 Specific discharge capacity of TDFC-1 and CS at varied current density from 0.05 A g^{-1} to 5.0 A g^{-1} in (a) Li- and (b) Na-cells. (c) Specific discharge capacity of TDFC-1 and CS in Li- and Na-cells up to 10,000 cycles. Li- and Na-cells were operated in voltage window of 1.5-4.2 V vs. Li and 1.3-4.2 V vs. Na for Li- and Na-cells, respectively.

The charge storage performances of the TDFC and CS electrodes were further assessed by galvanostatic charge/discharge tests in Li-cells (**Fig. 3.11 and Fig. 3.12**). Both the TDFC-1 and CS electrodes showed sloped charge and discharge profiles, which are originated from combination effects of double-layer capacitance and multiple redox reactions of the different oxygen functional groups and Li-ions [113, 123]. At a low current density of 0.05 A g^{-1}, the TDFC-1 delivered a high capacity of ~250 mAh g^{-1}, which is considerably higher than that of the CS (~153 mAh g^{-1}). The TDFC-1 electrode also exhibited excellent rate-performance by maintaining ~51% of its capacity (~128 mAh g^{-1}) at a 100 times higher current density (5 A g^{-1}). In contrast, the CS only retained 36% of its capacity at a high current density of 5 A g^{-1}.

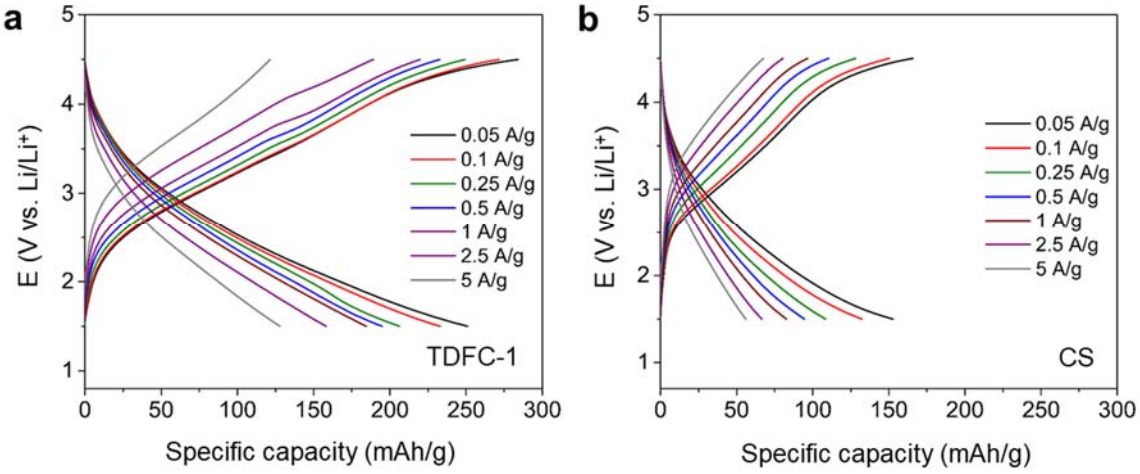

Figure 3.12 Rate-dependent GCD profiles of TDFC-1 and CS in Li-cells. (a) TDFC-1. (b) CS. Li- -cells were operated in the voltage range of 1.5-4.5 V vs. Li. The voltage profiles were measured from 0.05 to 5 A g^{-1}.

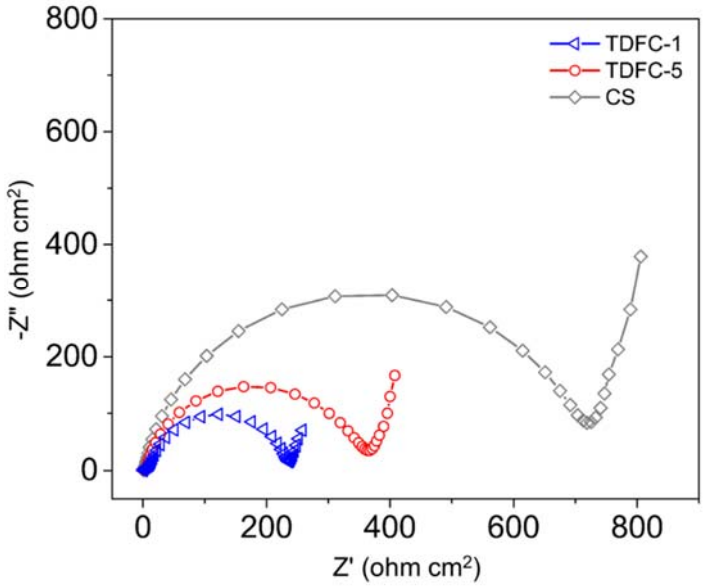

Figure 3.13 EIS measurement of the carbonaceous products. EIS measurement of TDFC-1, TDFC-5 and CS was carried out from 100 kHz to 10 mHz with an amplitude of 10 mV. The impedance was multiplied by the electrode area to obtain normalized real and imaginary impedances.

Electrochemical impedance spectroscopy (EIS) measurements were carried out to understand the difference of the rate-performance between TDFC and CS electrodes (**Fig. 13**). In the Nyquist plot, the intercept of the real Z'-axis represents the equivalent series resistance (ESR) due to bulk electrolyte/electrode resistance and contact resistance, and the semicircle at high-to-mid frequency indicates charge transfer resistances (R_{ct}). The TDFC-1, TDFC-5 and CS electrodes showed similar ESR values of 0.25~0.57. On the other hand, the R_{ct} value progressively decreased from 736 for the CS, to 354 for the TDFC-5, to 234 ohm·cm^2 for the TDFC-1, indicating facilitated charge transfer with reduced dimension of functional carbons. The electrochemical performance trends of the TDFC and CS electrodes in Na-cells were similar to those in Li-cells (**Fig. 3.11b and Fig. 3.14**). The TDFC-1 delivered a high capacity of ~210 mAh g^{-1} at a current rate of 0.05 A g^{-1} in Na-

cells, which is significantly higher than that of the CS (~125 mAh g^{-1}). Furthermore, the TDFC-1 maintained 48% of its high capacity at a high current density of 5 A g^{-1}, whereas the CS only retained ~20% of its capacity. These results indicate that the TDFC stores charge more effectively than the CS for both Li- and Na-ions.

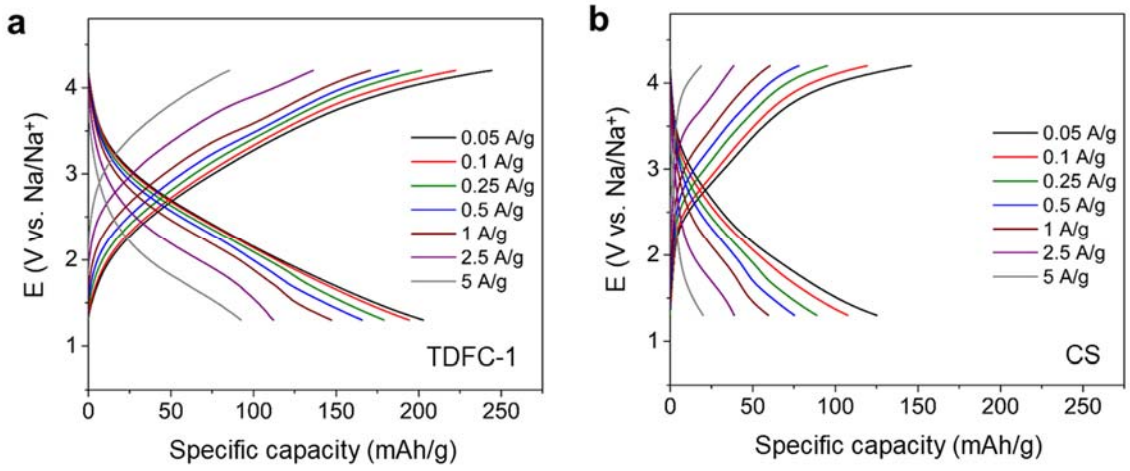

Figure 3.14 Rate-dependent galvanostatic charge/discharge (GCD) profiles of TDFC-1 and CS in Na-cells. (a) TDFC-1. (b) CS. Na-cells were operated in the voltage range of 1.3-4.2 V Na. The voltage profiles were measured from 0.05 to 5 A g^{-1}.

To investigate the mass loading effect on performance, we further increased the loading density of the TDFC-1 from 2.7 mg cm^{-2} to a commercial loading scale of 9.3 mg cm^{-2} (**Fig. 3.15**). It should be noted that loading densities of most reported carbon-based cathodes (0.4~2 mg cm^{-2}) are much lower than the commercial scale (~10 mg cm^{-2}).[104, 124] The TDFC-1 with a high loading density (9.3 mg cm^{-2}) showed no apparent capacity difference from that with an ordinary loading density (2.7 mg cm^{-2}) until the current density reached ~1 A g^{-1}, and only small differences at higher current densities. This superior rate-

performance of the TDFC even with the commercial loading-scale should be attributed to the fast redox-reactions within the ultra-thin 2D structure. Remarkably, the TDFC-1 electrode exhibited a stable cycling performance up to 10,000 cycles without noticeable differences in GCD profiles for both Li- and Na-cells (**Fig. 3.11c and Fig. 3.16**). The TDFC-1 in both Li- and Na-cells exhibited superior capacity and cycling stability compared to other organic-based cathodes (**Tables 3.1 and 3.2**).[101, 103-104, 124-130]

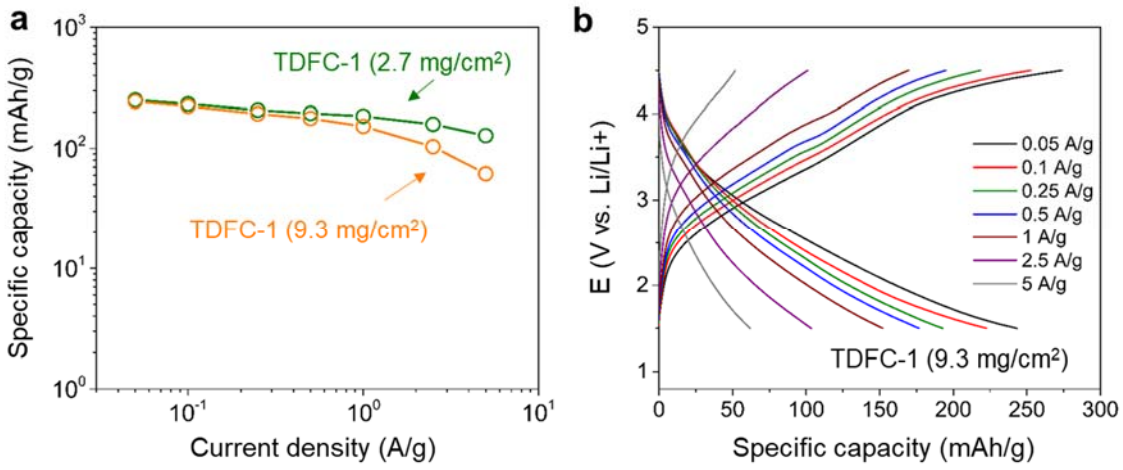

Figure 3.15 (a) Comparison of specific discharge capacity of TDFC-1 at different loading scales. (b) Rate-dependent GCD profiles of TDFC-1 at the high mass loading (9.3 mg cm^{-2}). Li-cells were operated in the voltage range of 1.5-4.5 V vs. Li at varied current density from 0.05 to 5 A g^{-1}.

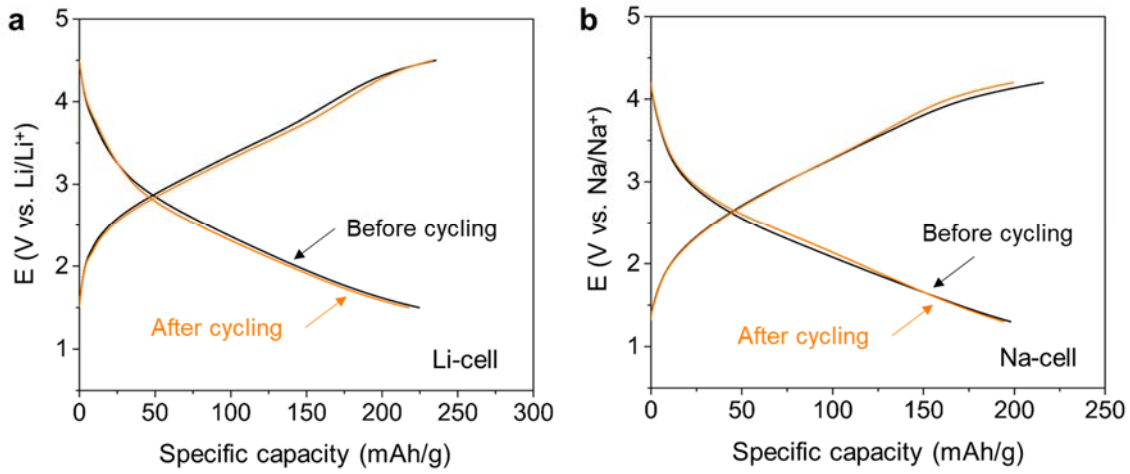

Figure 3.16 GCD of the TDFC-1 before and after cycling. (a) Li-cell at a voltage window of 1.5-4.5 V vs. Li. (b) Na-cell at a voltage window of 1.3-4.2 V vs. Na. The charge/discharge profiles were measured at a current density of 0.1 A g^{-1}.

Table 3.1. Comparison of gravimetric electrochemical performance of various electrodes.

Material	Loading density (mg/cm^2)	Capacity (mAh/g)	Cycling stability		
			Capacity (mAh/g)	Cycles	Capacity retention
Activated carbon [125]	2	~130 at 0.4A/g (Li)	110	1000	92%
Nitrogen-doped activated carbon [101]	—	130~165 at 0.4 A/g (Na)	110	500	86%
Peanut shell nanosheet carbon [104]	0.4	~165 at 0.1 A/g (Na)	<100	5000	82%
Disodium Rhodizonate [124]	2	~175 at 0. 1A/g (Li)	110	1500	88.2%
$Na_2C_6O_6$ [126]	~0.8	~190 at 0.025 A/g (Na)	<185	100	90%
Poly (benzoquinonyl sulfide) [127]	1~2	~247 at 0.1 A/g (Li) — (Na)	212 180	1000 100	86% 68%
Cuprous 7,7,8,8-tetracyanoquinodimethane [103]	0.9~1.2	~214 at 0.05 A/g (Na)	~205	50	—
$Na_4C_8H_2O_6$ [129]	0.75~1.5	~183 at 0.019 A/g (Na)	154	100	84%
perylene 3,4,9,10-tetracarboxylic dianhydride-based PI [130]	—	137 at 0.05 A/g (Na)	111	5000	87.5%
This work	**2.7~9.3**	**250 at 0.04A/g (Li)** **210 at 0.04A/g (Na)**	**217** **187**	**10000** **10000**	**93%** **94%**

Table 3.2. Comparison of areal electrochemical performance of various electrodes.

Material	Loading density (mg/cm^2)	Capacity (mAh/cm^2)	Cycling stability		
			Capacity (mAh/cm^2)	Cycles	Capacity retention
Activated carbon [125]	2	~ 0.260 at 0.8 $\mu A/cm^2$ (Li)	0.22	1000	92%
Peanut shell nanosheet carbon [104]	0.4	~ 0.066 at 0.04 $\mu A/cm^2$ (Na)	~0.04	5000	82%
Disodium Rhodizonate [124]	2	0.350 at 0.2 $\mu A/cm^2$ (Li)	0.22	1500	88.2%
$Na_2C_6O_6$ [126]	~0.8	0.152 at 0.02 $\mu A/cm^2$ (Na	~0.15	100	90%
Poly (benzoquinonyl sulfide) [127]	1~2	0.494 at ~0.2 $\mu A/cm^2$ (Li) —	0.42 0.86	1000 100	86% 68%
Cuprous 7,7,8,8-tetracyanoquinodimethane [103]	0.9~1.2	0.257 at ~0.06 $\mu A/cm^2$ (Na)	~0.25	50	—
$Na_4C_8H_2O_6$ [129]	0.75~1.5	0.275 at 0.0285 $\mu A/cm^2$ (Na)	~0.23	100	84%
This work	**2.7~9.3**	**2.28 at 0.372 $\mu A/cm^2$ (Li)** **0.567 at 0.108 $\mu A/cm^2$ (Na)**	**2.02** **0.51**	**10000** **10000**	**93%** **94%**

Areal capacity was calculated from the loading-density and gravimetric capacity in table S1.

We evaluated the performance of the Li-HSC by combining the commercial loading-scale TDFC-1 (9.3 mg cm^{-2}) cathode with a Si-based anode.[131] The Si-based anodes were pre-lithiated against a piece of Li metal to introduce Li source for the full-cell assembly. The galvanostatic charge/discharge profiles of the full-cell were investigated at different upper cut-off voltages. In the voltage window of 1.3-4.2 V, the TDFC-1 in the full-cell exhibited a capacity of ~180 mAh g^{-1} at a current density of 0.05 A g^{-1} (**Fig. 3.17**).

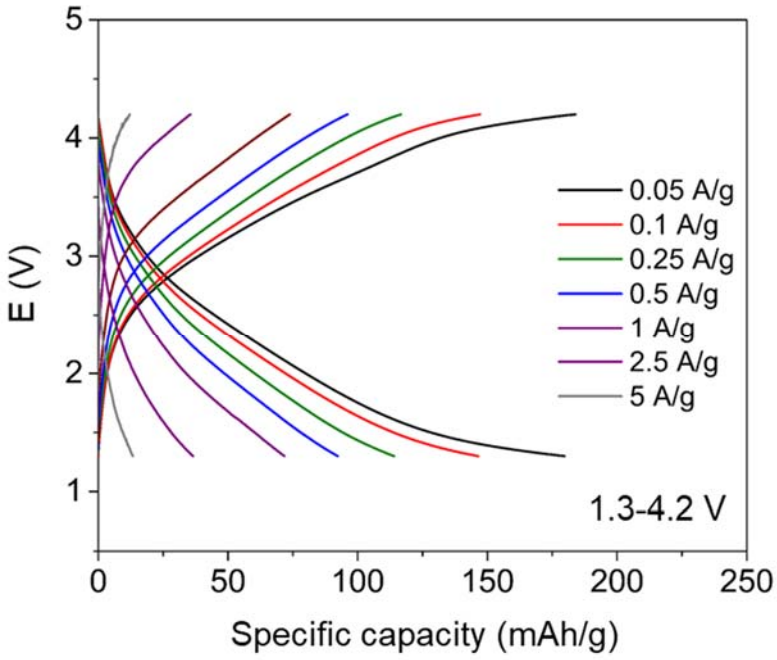

Figure 3.17 Rate-dependent galvanostatic charge/discharge (GCD) profiles of TDFC-1 in the full-cell. The full-cell were operated in the voltage range of 1.3-4.2 V at varied current density from 0.05 to 5 A g^{-1}.

As the upper cut-off voltage increased from 4.2 to 4.3 V, the TDFC-1 delivered a high capacity of ~205 mAh g^{-1} (a corresponding areal capacity of ~1.91 mAh cm^{-2}) at 0.05 A g^{-1} (Fig. 5a), which is 82% of that in Li half-cells. Based on the rate-dependent galvanostatic charge/discharge profiles (**Fig. 3.18a**), the energy and power density of the

full-cells were projected onto a Ragone plot (**Fig. 3.18b**). We calculated the energy and power density of the full-cell based on the total mass of the active materials in both the anode and cathode. The maximum energy density of the full-cell was found to be ~290 Wh kg^{-1}. At a high power density of 1 kW kg^{-1}, the full-cell can deliver a high energy density of 182 Wh kg^{-1}. It should be noted that this energy density was achieved with the commercial loading scale of the TDFC-1 (~9.3 mg cm^{-2}) and can be further increased by optimizing the mass ratio to the electrodes. In order to estimate actual device-based performance, we further divided the Ragone plot of the full-cell by factors of 3~4. It should be noted that the factors of 3~4 are applicable only to the commercial loading density of ~10 mg cm^{-2} for carbon-based electrodes.[132] The estimated energy densities were found to be 10~28 Wh/kg at high power densities of 1~2 kW kg^{-1}. This estimated performance indicates that the TDFC-based full-cell can potentially bridge the performance gap between conventional supercapacitors and LIBs.[5] The cycling stability of the full-cell was evaluated by repeating a slow charge/discharge capacity measurement cycle at 0.1 A g^{-1} and 99 accelerated cycles at 5 A g^{-1} up to 2,000 cycles at the voltage window of 1.3-4.2 V. At the end of the 2,000 cycles, the full-cell was rest at open circuit for 8 hours, and then further cycled at the voltage window of 1.3-4.3 V up to 3,000 cycles (**Fig. 3.18c**). The full-cell retained ~85% of its initial discharge capacity over 2000^{th} cycle with high Coulombic efficiency over 99%. After the rest, the full-cell showed a recovery of its capacity and a negligible change in capacity during the additional 1,000 cycles at a different voltage window of 1.3-4.3 V

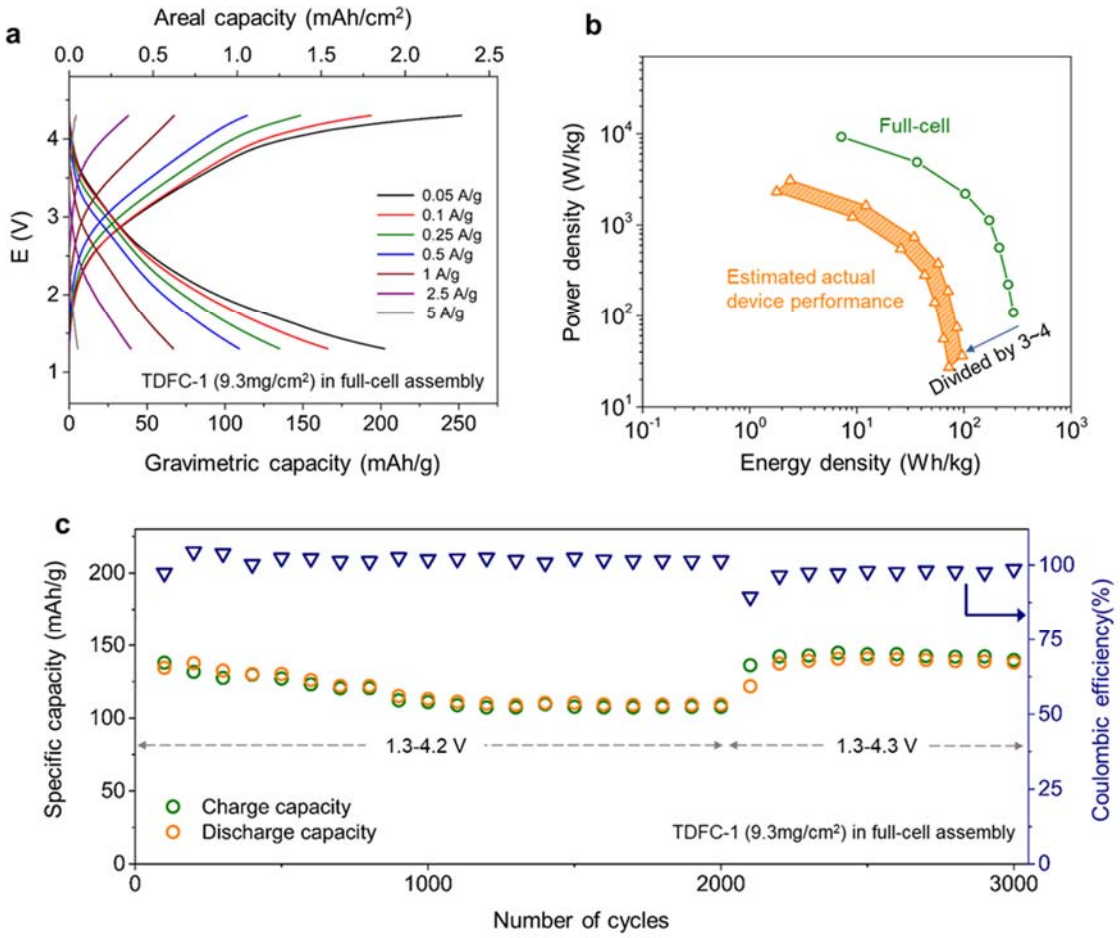

Figure 3.18 Electrochemical characterization of high-mass loading TDFC-1 in full-cell assembly. (a) Rate-dependent GCD profiles of the TDFC-1 in a full-cell assembly at a voltage window of 1.3-4.3 V. (b) Ragone plot of the full-cell calculated from (a). Power- and energy-densities of the full-cell were normalized by all electro-active material in both the anode and cathode. (c) Cycling stability of the full-cell measured by an accelerated cycling test method up to 3,000 cycles.

3.5 Conclusions

In this study, the ultra-thin (10~20nm) TDFC with abundant redox-active oxygen functional groups *via* a template-assisted hydrothermal carbonization process of glucose has been synthesized. The unique 2D thin film structure of the TDFC enables more efficient

utilization of the redox reactions compared to the conventional CS, delivering significantly enhanced capacities of ~250 mAh g^{-1}. We have therefore revealed that reducing the dimension of functional carbon is a key approach to effectively utilize their redox-reactions. In addition, the hybrid supercapacitors consisting of the commercial loading scale TDFC-1 cathode (~9.3 mg cm^{-2}) and a Si-based anode exhibited a high energy-density of 182 Wh kg^{-1} at a high-power density of 1 kW kg^{-1}. However, it should be mentioned that the performance of the hybrid supercapacitors is not fully optimized. Combining the TDFC with a capacitive anode, such as graphene, may improve the overall power performance and cycling stability of the hybrid supercapacitors. The results highlight the importance of the structure control of the carbonaceous product to enhance the charge storage performance. This strategy can be extended by further reducing the dimension of functional carbons to 1D and 0D structures to improve the utilization of the redox reactions. In addition, surface chemistry control of the carbonaceous product is required in order to improve the redox reactions with Li- and Na-ions. Furthermore, other renewable biomass beyond glucose can be employed to produce more cost-effective functional carbon electrodes.

CHAPTER 4.

CRUMPLED GRAPHENE OXIDE CATHODE FOR LI-ION BATTERIES

Reproduced from Byeongyong Lee, Chongmin Lee, Tianyuan Liu, Kwangsup Eom, Zhongming Chen, Suguru Noda, Thomas F. Fuller, Hee Dong Jang and, Seung Woo Lee, Hierarchical networks of redox-active reduced crumpled graphene oxide and functionalized few-walled carbon nanotubes for rapid electrochemical energy storage. Nanoscale 2016 **8**, 12330-12338. Royal Society of Chemistry specifies that permission request for reproduction if the reproduction is for thesis.

4.1 Overview

A critical hurdle of graphene based electrodes prepared from the GO dispersion is an irreversible restacking of graphene sheets during the preparation of electrodes due to the strong π-π interaction, decreasing electrochemically accessible surface area.[32, 133-134] Various methods have been investigated for preventing the restacking issues of graphene based electrodes.[32, 65, 92, 135-136] Nanocomposite electrodes with physical '*spacers*', such as carbon black,[40] nanodiamond,[41] and CNT,[42] were employed to separate the graphene sheets, thereby securing the active surface area. In addition, 3D graphene assembly was developed by hydrothermal reduction[43] or freeze-drying[44] processes of the GO dispersion, providing large accessible surface with an interconnected network structure.[23, 75] Recently introduced crumpled graphene has a strong aggregation-resistive characteristic

owing to its unique 3D ball morphology, proposing a promising solution to prevent the restacking problem.[32, 40] The crumpled graphene was employed as electrode materials for EDLCs, one type of ECs, demonstrating enhanced capacitance and rate-capability.[137] However, the energy density of the crumpled graphene based EDLC is still significantly lower than those of pseudocapacitor or LIBs utilizing redox (Faradaic) reactions.[114, 137]

4.2 Approach

A rising strategy to improve the energy density of carbon-based electrodes is introducing redox-active functional groups to support pseudocapacitance (surface redox reaction) on top of double layer capacitance.[57, 70, 91, 114, 116, 138-142] Previous studies showed reversible redox reactions between Li ions and oxygen functional groups, such as carbonyl groups, on the various carbon supports, including CNT,[91, 114, 116, 139-142] reduced graphene,[122, 143] and biomass derived carbon spheres,[48] at high redox potential of ~3 V vs. Li/Li^+. Thus, we envision that if these redox reactions are introduced onto the partially reduced crumpled graphene oxide (r-CGO), the energy density of the r-CGO based electrodes can be considerably improved while maintaining their high rate-capability.

4.3 Experimental Methods

4.3.1 Sample Preparation

Colloidal GO solution was prepared using the modified Hummers' method.[91, 144] Partially reduced crumpled graphene oxide (r-CGO) was synthesized from sprayed

droplets of the colloidal GO solution by aerosol spray pyrolysis.[32, 75] The 0.5 wt% of the GO solution was nebulized in an ultrasonic atomizer (Htech Co, model US-06) to generate sprayed water droplets containing GO nanosheets. The droplets were carried by Ar gas with a flow rate of 10 L/min into a pre-heated (~300 °C) tubular furnace. The as-fabricated r-CGO via evaporation of water in the droplets and concomitant thermal reduction was collected from a filter located at the end part of the tubular furnace, and the gathered r-CGO was dispersed in deionized water and ethanol (volume ratio, 1:1) in a bath sonicator for 10 min. FWNT was prepared by a chemical vapor deposition method.[129, 145] The FWNT was oxidized by an acidic treatment.[91] In brief, 100 mg of the pristine FWNT was refluxed in a mixture of 150 mL of H_2SO_4 and 50 mL of HNO_3 at 80 °C for 2 h. The f-FWNT was obtained after rinsing the mixture with 5 vol % of HCl solution in DI water and followed by rinsing with DI water. Finally, the f-FWNT dispersion was obtained by ultrasonication of f-FWNTs in water and ethanol mixture (volume ratio, 1:1) for 40 min.

The free-standing f-FWNT/r-CGO films were obtained by a vacuum filtration process.[92] The f-FWNT and r-CGO dispersions were mixed and agitated for 30 min. The mixture was vacuum-filtrated with a polypropylene separator (Celgard 2500) as a filtration membrane. After an air-drying process for 1 h, the film was detached from the membrane followed by a vacuum drying overnight at 70 °C. The f-FWNT, GO and f-FWNT/GO electrodes were also obtained by the same preparation process of the f-FWNT/r-CGO. The f-FWNT/rGO was prepared by thermally reducing the f-FWNT/GO in a tube-furnace at 200 °C for 2 h under Ar environment.

4.3.2 Material Characterization

The morphology of the electrodes was investigated by cold field emission SEM (Hitachi SU8010, operated at 3 kV). TEM was carried out by JEOL JEM-ARM200F. The elemental analysis of the films was examined by XPS (Thermal Scientific K-alpha XPS instrument) and C1s peaks were fitted by XPSPEAKS 4.1.[122] Relative intensity of D and G band was examined by Raman Spectrometer (Thermo Nicolet Almega XR Dispersive Raman Spectrometer). XRD was investigated by X'Pert Pro Alpha-1. The electrical conductivity was measured by Lucas Lab Pro 4-point systems. Electrochemical impedance analysis was carried out by AutoLab Metrohm.

4.3.3 Electrochemical measurement

The prepared electrodes were cut into a small piece with a razor blade and directly used as positive electrodes without binders and conductive additives in Swagelok-type cells. A piece of pure lithium foil was used as negative electrodes. Celgard 2500 and 1 M $LiPF_6$ in a mixture of EC and DMC (volume ratio, 3:7, BASF) were adopted for separator and electrolyte, respectively. The Li-cells were assembled in a glove box (MBraun), maintaining O_2 and H_2O < 0.1 ppm. The electrochemical performances of the Li-cells were investigated with a potentiostat/galvanostat (Bio-Logic VMP3) in the voltage range of 1.5 - 4.5 V vs. Li. The Li-cells were charged or discharged with varied galvanostatic current densities (from 0.1 to 10 A g^{-1}), and the cell voltage was held constant for 30 min, 1.5 and 4.5 V at each end of discharge and charge, respectively. The cycling stability was examined by an accelerated cycling test.[122, 146] After completing 99 cycles at 10 A g^{-1} without holding

the voltage, the Li-cells were discharged/charged at 0.1 Ag^{-1} for one cycle with holding the voltage for 30 min.

4.4 Results and Discussion

Previously, the crumpled graphene was prepared by an aerosol spray evaporation of aqueous GO droplets at a high temperature of 800 °C followed by a chemical reduction process,[137] resulting in very low oxygen contents. In this study, the partially reduced crumpled graphene oxide particle was prepared at a mild temperature of 300 °C without further chemical reduction process to maintain the oxygen-functional groups on the surface of the r-CGO. SEM and HRTEM images of the as-synthesized r-CGO displayed a wrinkled particle shape with the size range of 300~700 nm (**Fig. 4.1a,b**). High-magnification HRTEM images of the r-CGO particle displayed distorted ridges with several tens of nanometer in thicknesses (**Fig. 4.1c,d**).[32] The f-FWNT was also prepared by chemically oxidizing FWNT via previously reported protocols.[91, 129, 145] The HRTEM investigation clearly showed that the smooth outer surface of the pristine FWNT (**Fig. 4.1e**) has roughened after the oxidization process (**Fig. 4.1f**).

This surface structural change is ascribed to the introduction of the oxygen functional groups on the surface of the FWNT.[43] The composite, f-FWNT/r-CGO, films were prepared by filtering the mixture of the f-FWNT and r-CGO dispersion with varied mass ratios, yielding free-standing, additive-free electrodes with a density of ~0.4 g cm^{-3} (**Fig. 4.2**). It should be mentioned that the assembly of the r-CGO only free-standing electrode is impossible owing to its strong aggregation resistant property. Therefore, sub-millimeter long FWNT[145] was employed as a conductive binder to prepare free-standing composite

electrode. The f-FWNT/rGO composite electrode was also prepared using the mixture of the f-FWNT and conventional GO via VF process.[141] In the mixture of the f-FWNT and GO, same mass of the f-FWNT and GO was used. The GOs within this electrode were further thermally reduced at 200 °C for 2 h under Ar environment, finally producing the f-FWNT/reduced GO (rGO) composite electrodes. The microstructures of the f-FWNT/r-CGO and f-FWNT/rGO composite electrodes were compared (**Fig. 4.3**). The f-FWNT/r-CGO electrode with 1:1 mass ratio between the f-FWNT and r-CGO showed a 3D hierarchical porous structure, where the r-CGO was randomly entangled with f-FWNTs (**Fig. 4.3a-d**). We can envision fast ion and electron transport through this 3D porous network structure, enabling fast charge storage. In contrast, the f-FWNT/rGO electrode displayed a 2D alternating layered structure, where rGO sheets are separated by the inserted f-FWNTs (**Fig. 4.3e,f**). In this 2D structure, electrolyte ions can be readily transported along in-plane direction, but their fast transport through thickness direction can be restricted, potentially limiting rate-capability of the electrode.

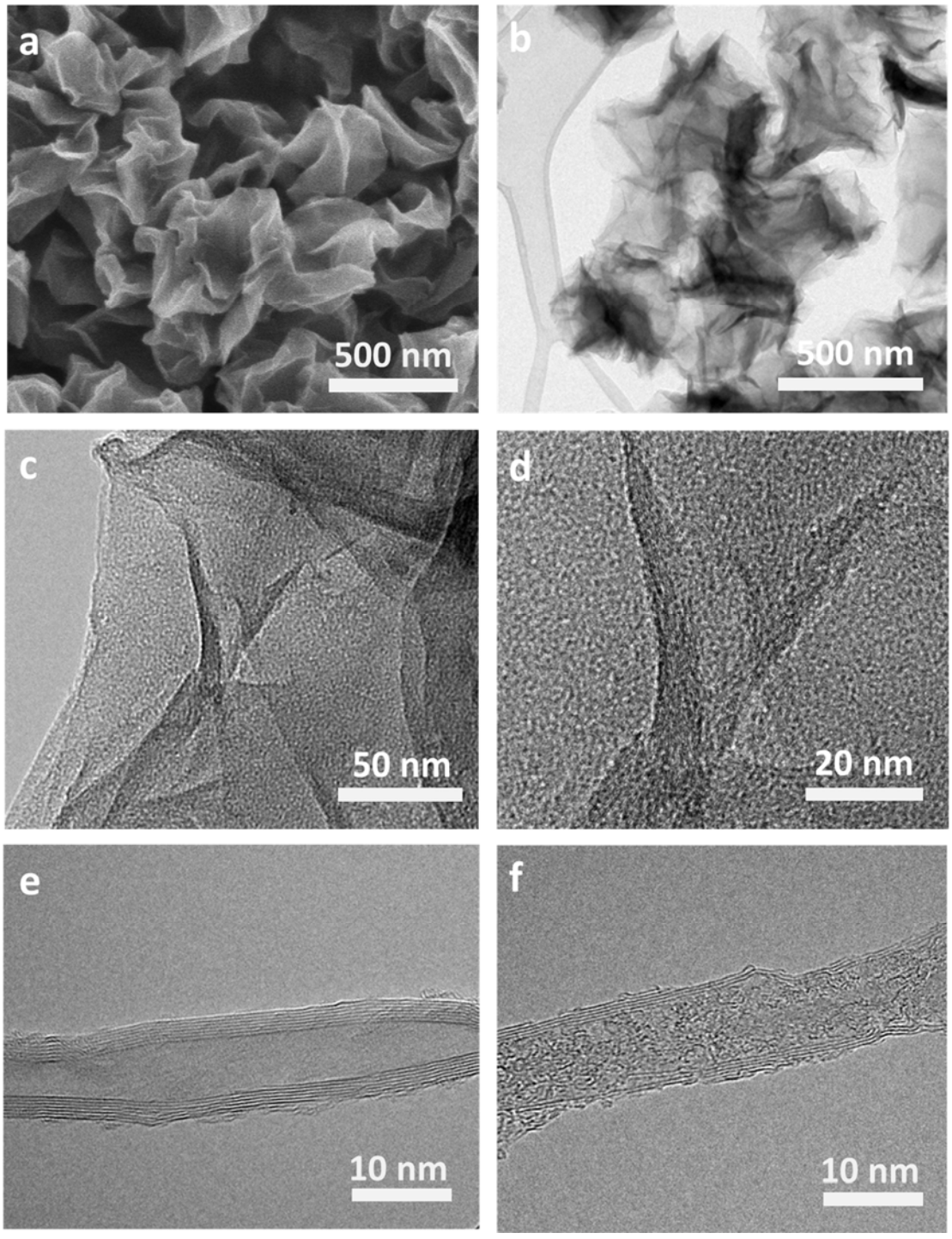

Figure 4.1 (a) SEM image of the partially reduced crumpled graphene oxide (r-CGO). HRTEM images of the (b, c, d) r-CGO, (e) few-walled carbon nanotube (FWNT) and (f) oxygen-functionalized (f-FWNT).

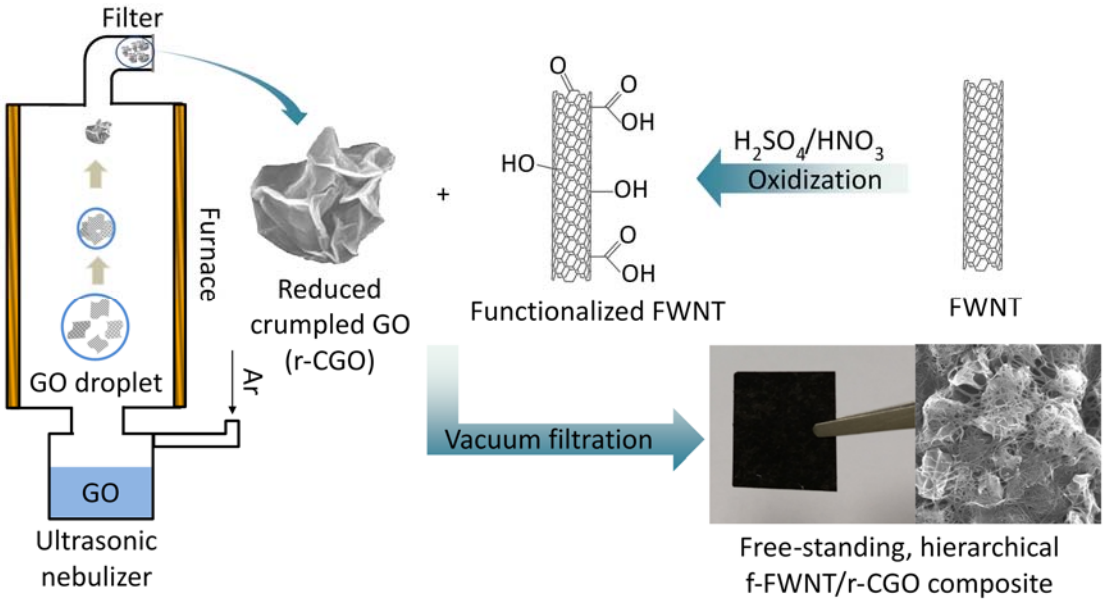

Figure 4.2 Fabrication process of the f-FWNT/r-CGO electrode.

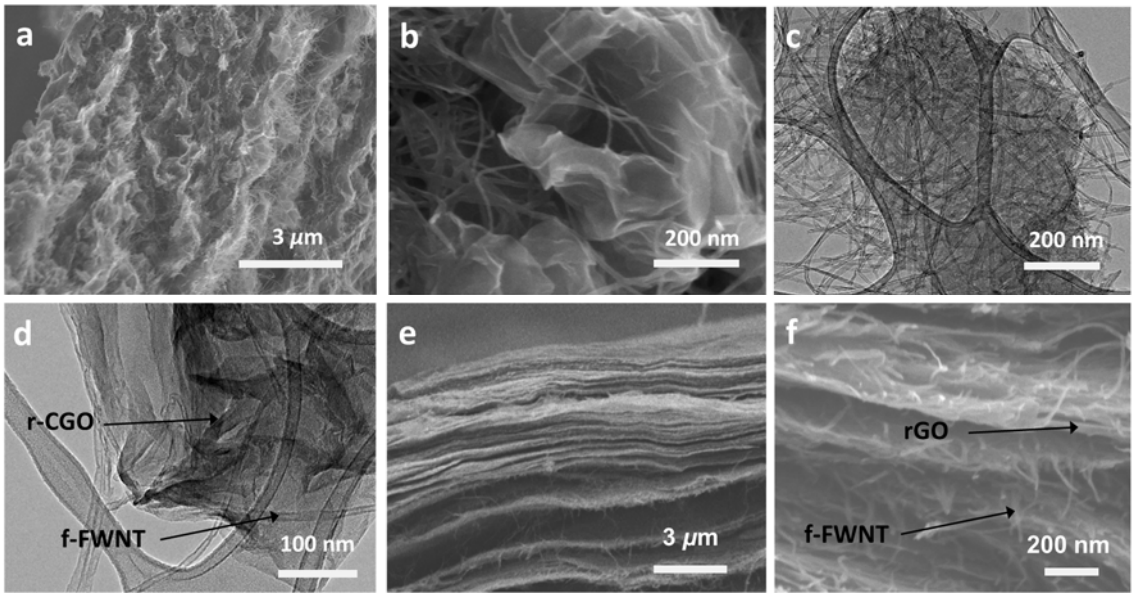

Figure 4.3 (a, b) SEM cross-section view images of the f-FWNT/r-CGO electrode. (c, d) HRTEM images of the f-FWNT/r-CGO electrode. (e, f) SEM cross-section view images of the f-FWNT/rGO electrode.

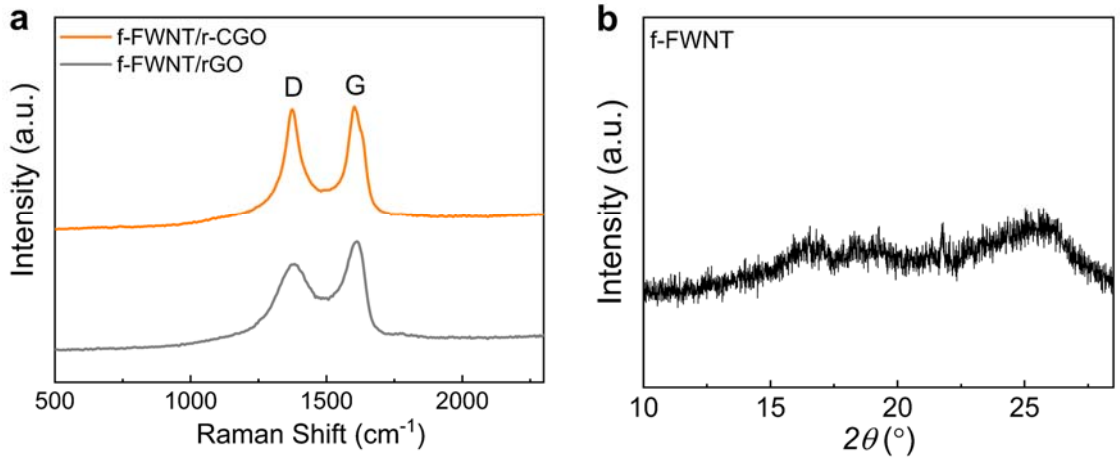

Figure 4.4 (a) Raman spectra of the f-FWNT/r-CGO and f-FWNT/rGO electrodes. (b) XRD investigation of the f-FWNT electrode.

The f-FWNT/rGO and f-FWNT/r-CGO electrodes showed both D band at ~1370 cm^{-1} and G band at ~1600 cm^{-1} (Fig. 4.4a).[147] The D band arises from disorder of sp^2-hybridized carbon in graphene, while the G band is originated from in-plane stretching mode of carbon-carbon bond in graphitic materials.[148] The relative intensity of D to G band (I_D/I_G) of the f-FWNT/r-CGO electrode was slightly higher (I_D/I_G = 0.98) than that of the f-FWNT/rGO electrode (I_D/I_G = 0.82), indicative of the more defect sites in the f-FWNT/r-CGO electrode. X-ray diffraction (XRD) analysis was used to further investigate the structure of the assembled electrodes. The f-FWNT/GO electrode showed an intense peak at 2θ = 11.6° (an interlayer distance of 0.76 nm), which is similar to that observed in stacked graphene oxide sheets (**Fig. 4.5a**).[149] This indicates that some of the GO sheets are still locally restacked, rather than the fully separated structure by the inserted f-FWNTs. A layered structure of graphitic materials can be characterized by (002) peak at the 2θ = 26.2°.[43] Previous study showed that graphite or restacked graphene sheets exhibit sharp (002) peaks at the 2θ = 26.2° due to their 2D layered structures, whereas the 3D graphene

hydrogels display broad and weak (002) peaks owing to the poor ordering along the stacking directions and their porous structure.[150] After the thermal reduction process from the f-FWNT/GO to the f-FWNT/rGO, the intense peak at 2θ = 11.6° of the f-FWNT/GO electrode disappeared and the broad peak at 2θ = 25.7° (*d*-spacing of 0.35 nm) increased, which can be attributed to the removal of oxygen groups with the concomitant formation of the loosely packed rGO structure.[150-151] In contrast, the f-FWNT/r-CGO electrode showed negligible peaks compared to those of other films, further illustrating its disordered structure.

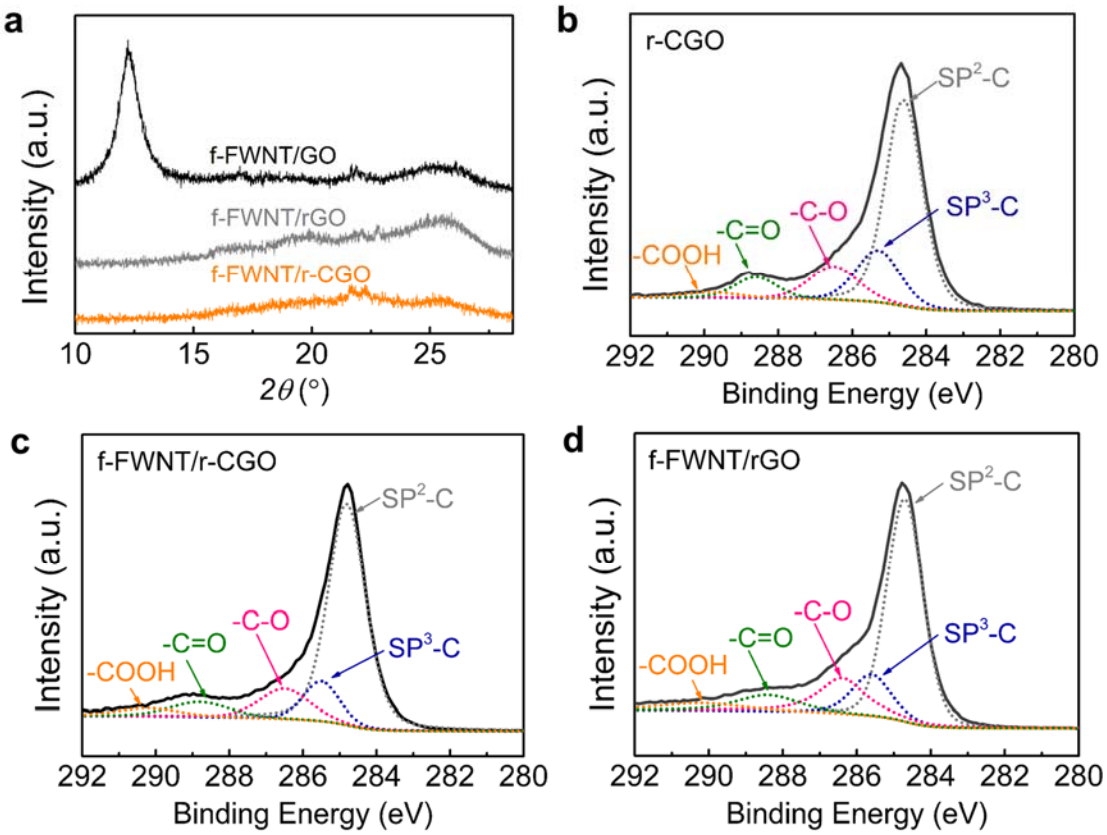

Figure 4.5 (a) X-ray diffraction (XRD) spectra of the composite electrodes. Surface chemistry investigation by high-resolution C1s spectra of the (b) partially reduced crumpled graphene oxide (r-CGO), (c) f-FWNT/r-CGO and, (d) f-FWNT/rGO.

The surface oxygen chemistry of the carbon materials was examined by XPS. Wide survey scan peaks with atomic ratios of oxygen to carbon (O/C) were compared for GO, r-CGO, f-FWNT, and the assembled electrodes (**Fig. 4.6a**). The GO had the highest O/C ratio of 0.41, while the r-CGO showed an O/C ratio of 0.26, indicative of its partially reduced structure. The O/C ratio of FWNT (0.13) is lower than those of GO and r-CGO and thus the composite electrodes showed decreased O/C ratios for f-FWNT/GO (0.28) and for f-FWNT/rGO (0.17). The f-FWNT/rGO also showed an O/C ratio of 0.17, indicating compositional similarity of the oxygen functional groups to the f-FWNT/r-CGO. The density normalized electrical conductivities of the f-FWNT/GO, f-FWNT/rGO, and f-FWNT/r-CGO electrodes were found to be 22.7, 74.9 and 67.1 S cm^2/g, respectively, showing a correlation with the O/C ratios of the electrodes.[117, 152] The main components of oxygen functional groups were investigated by the high resolution C1s spectra (**Fig. 4.5b-d and Fig. 4.6b-d**). The peaks were fitted with sp^3-hybridized carbon at 285.2 ± 0.2 eV, hydroxyl or epoxide (-C-O) at 286.5 ± 0.2 eV, carbonyl (-C=O) at 288.2 ± 0.2 eV, and carboxyl group (-COOH) at 290.2 ± 0.2 eV by setting the sp^2-hybridized carbons at 284.5 eV as the basis.[134, 149, 153] The C1s spectra of the r-CGO (**Fig. 4.5b**) displayed considerably reduced hydroxyl or epoxide group (-C-O) peak intensity and negligible change of carbonyl (-C=O) and carboxyl (-COOH) group peaks compared to those of the GO owing to the partial reduction process at a mild temperature.[141] The high resolution C1s spectra of the f-FWNT electrode showed similar oxygen functional group peaks yet slightly decreased intensities compared to those of the r-CGO. It is worth mentioning that the f-FWNT/r-CGO and

FWNT/rGO are compositionally similar as supported by the same O/C ratio of 0.17 (**Fig. 4.5c,d**), providing good model systems to compare the electrochemical performance of the 2D and 3D nanostructured carbon electrodes.

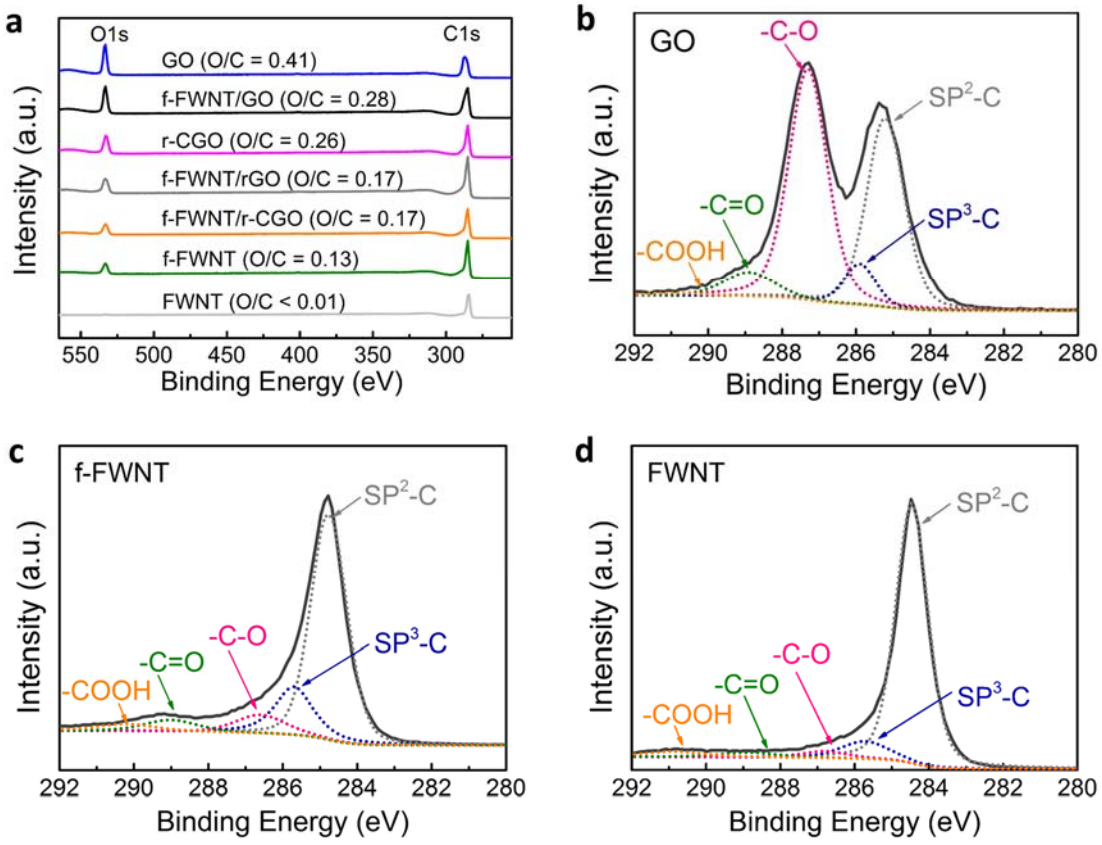

Figure 4.6 (a) Wide scan survey of the electrodes and r-CGO powder. High resolution C1s spectra of (b) the GO, (c) f-FWNT and (d) FWNT.

Electrochemical charge storage characteristics of the composite electrodes were investigated by cyclic voltammetry (CV) tests in the voltage range of 1.5 ~ 4.5 V vs. Li/Li^+ in Li-cells (**Fig. 4.7a,b** and **Fig. 4.8**). Comparison of CV scans at a slow scan rate of 1 mV/s showed that the f-FWNT/r-CGO electrode exhibited higher gravimetric current density compared to that of the f-FWNT/rGO electrode (Fig. 3a). The f-FWNT/GO

electrode displayed negligible redox peaks despite its high oxygen content (**Fig. 4.8a**), due to the poor electrical conductivity of the GO.[19] After the reduction process, the f-FWNT/rGO electrode showed indistinct redox feature in the broad voltage range of 2.5-4 V vs. Li. On the other hand, the f-FWNT/r-CGO electrode displayed significantly enhanced redox peaks centered at ~3 V vs. Li that are ascribed to the redox reactions between oxygen functional groups and Li ions.[91, 114, 122, 141, 146] The difference of the gravimetric current density between f-FWNT/r-CGO and other electrodes became prominent at a high scan rate of 5 mV/s (**Fig. 4.7b**). The f-FWNT/r-CGO electrode still maintained its redox peaks with the increased gap between oxidation and reduction peak potentials, while other f-FWNT/rGO and f-FWNT/GO electrodes only showed skewed CV shape with negligible redox behaviour. Since the O/C ratios and electrical conductivities of the f-FWNT/r-CGO and f-FWNT/rGO electrodes are similar, the enhanced charge storage performance of the f-FWNT/R-CGO can be attributed to its unique microstructure facilitating the surface redox reactions of the oxygen functional groups. We postulate that 3D hierarchical structure of the f-FWNT/r-CGO can provide continuous ion transport pathway into the inner space of the electrode for effective utilization of the oxygen functional groups, while 2D layered structure of the f-FWNT/rGO have limited ion accessibility through the rGO layers. Galvanostatic rate capability tests were carried out for the assembled electrodes, showing sloped charge and discharge curves (**Fig. 4.7c,d and Fig. 4.8b**). The sloped charge and discharge profiles of the functionalized carbon electrodes can be attributed to the coupling of the charge storage mechanisms: double-layer capacitance and the surface redox reactions of various oxygen functional groups, as reported in a previous study.[122]

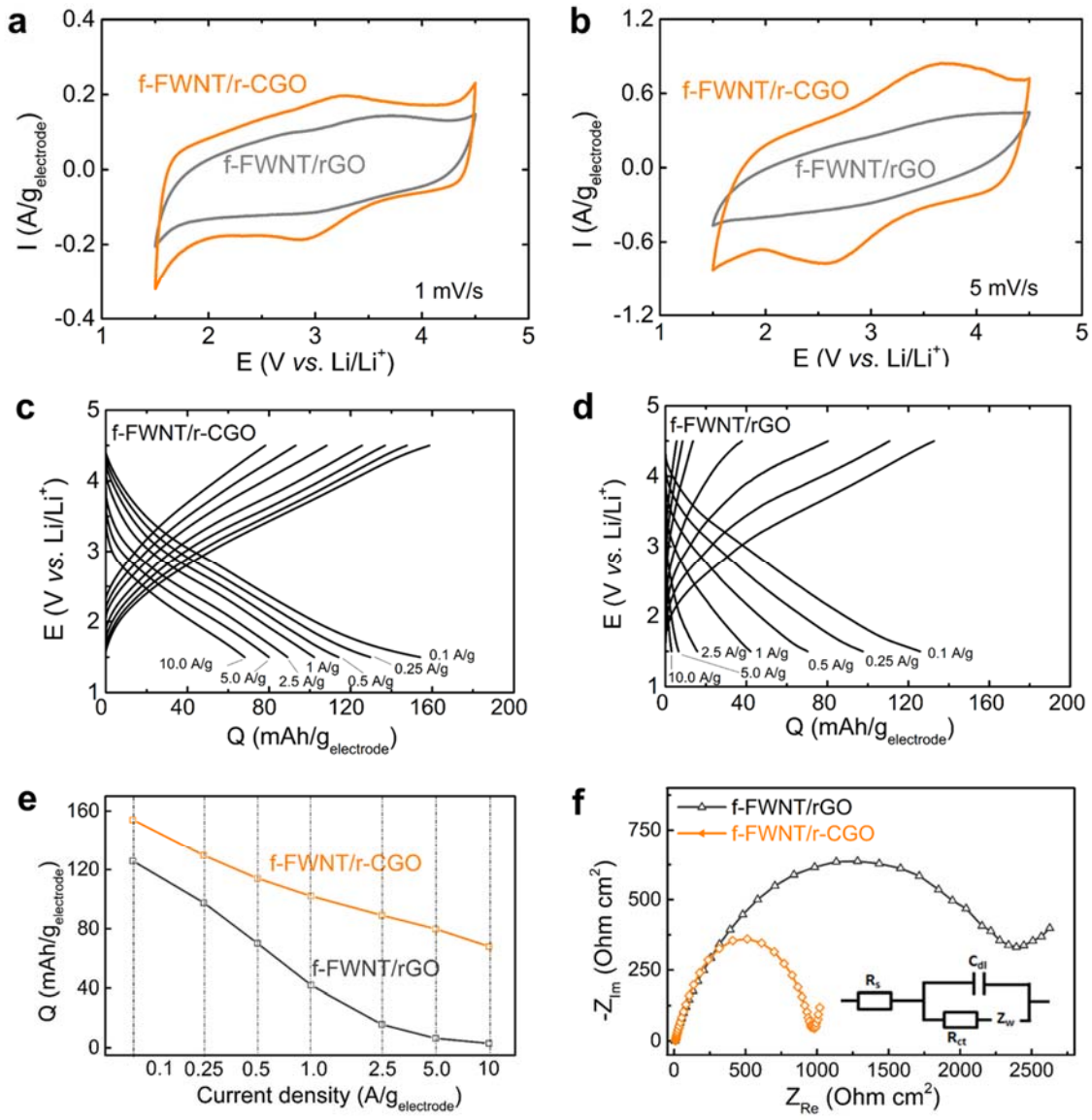

Figure 4.7 CV scans in the voltage range of 1.5-4.5 vs Li. at scan rates of (a) 1 mV s^{-1} and (b) 5 mV s^{-1} of the composite electrodes. Rate-dependent GCD profiles of (c) the f-FWNT/r-CGO and (d) f-FWNT/rGO at the varied current densities of 0.1-10 A g^{-1}. (e) Gravimetric capacity comparisons of the f-FWNT/r-CGO and f-FWNT/rGO as a function of discharge current density. (f) EIS investigation of the f-FWNT/r-CGO and f-FWNT/rGO electrodes.

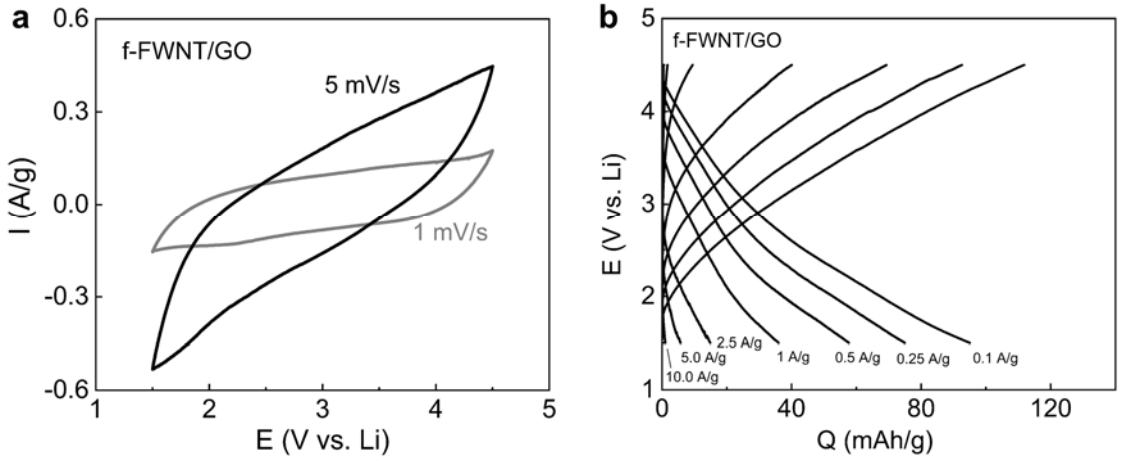

Figure 4.8 (a) CV scans of the f-FWNT/GO composite electrode at scan rates of 1 mV/s and 5 mV/s in the voltage window of 1.5-4.5 V vs. Li. (b) Rate-dependent GCD profiles of the f-FWNT/GO electrode.

At a slow discharge rate of 0.1 A/g, the f-FWNT/r-CGO electrode exhibited a gravimetric capacity of ~154 mAh/g, which is higher than those of the f-FWNT/GO (~95 mAh/g, **Fig. 4.8b**) and f-FWNT/rGO (~126 mAh/g). As the current density increased to 1 A/g, the capacity of the f-FWNT/rGO rapidly decreased to ~40 mA h/g, whereas the f-FWNT/r-CGO still retained a high capacity of ~100 mAh/g. The difference in gravimetric discharge capacities between the composite electrodes gradually increased with increasing current density (**Fig. 4.7e**). At a high current density of 10 A/g, the f-FWNT/r-CGO exhibited ~68 mA h/g, while the f-FWNT/rGO showed negligible gravimetric capacity. Consistent with the CV results, the trend in the galvanostatic discharge further supports faster charge storage performance of the f-FWNT/r-CGO electrode compared to the f-FWNT/rGO electrode owing to its unique 3D structure than can facilitate ion transport.

We employed EIS to further understand the difference of the rate-capability between the electrodes. **Fig. 4.7f** showed Nyquist plots and Randles equivalent circuit of the f-FWNT/r-CGO and f-FWNT/rGO electrodes. Charge transfer resistance (R_{ct}) typically gives information about the kinetics of the redox reactions occurring at the electrode surface.[154] The values of R_{ct} for the f-FWNT/r-CGO and f-FWNT/rGO are ~1000 and ~2350 Ω cm^2, respectively, indicating much faster redox reactions of the f-FWNT/r-CGO than f-FWNT/rGO. At the low frequency region, the f-FWNT/r-CGO electrode exhibited a steeper slope compared to that of the f-FWNT/rGO, implying that the hierarchical porous structure can efficiently support fast ion diffusion to keep up with the change of frequency.[41, 155]

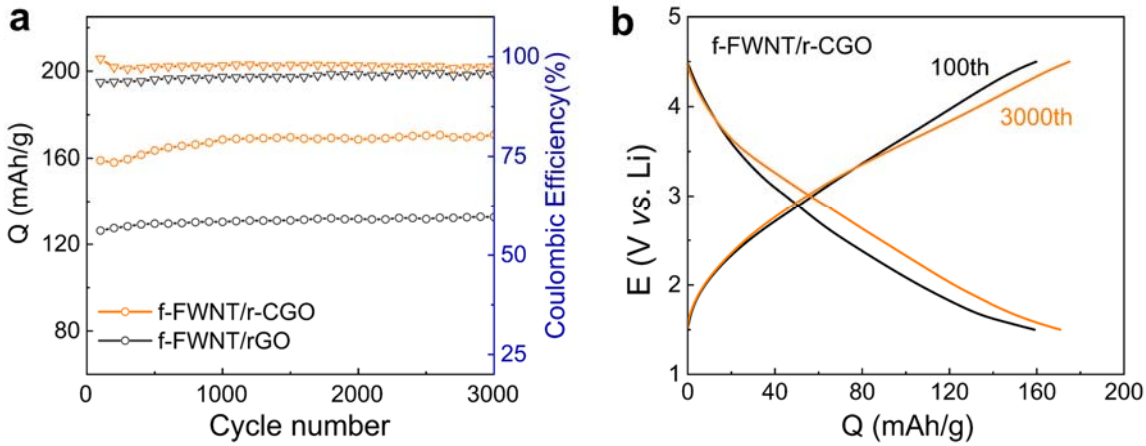

Figure 4.9 (a) Discharge capacities and Coulombic efficiencies of the f-FWNT/r-CGO at a current density of 0.1 A/g as a function of cycle number. (b) Comparisons of the galvanostatic charge and discharge voltage profiles at 100th and 3000th cycles for the f-FWNT/r-CGO electrode.

Table 4.1 Capacity comparison of various free-standing carbon-based cathodes with f-FWNT/r-CGO

Materials(Thickness)	Voltage window	Capacity based on the mass of the electrode	Reference
f-FWNT/C-rGO (30 µm)	**1.5-4.5V**	**170 mAh/g at 0.1 A/g**	**This work**
folded-graphene film (51 µm) [122]	1.5-4.5 V	160 mAh/g at 0.1 A/g	*Chem. Mater.,* **2015**, 27, 3291–3298
Oxidized CNT + graphene oxide composite electrode (4 µm)[141]	1.5-4.5 V	135 mAh/g at 0.1 A/g	*Adv. Funct. Mater*., **2013,** 23, 1037-1045.
Functionalized CNT (3.6 µm)[142]	1.5-4.5 V	117 mAh/g at 0.05 A/g	*Energy Environ. Sci*., **2013,** 6, 888-897.
Oxidized CNT (15 µm)[116]	1.5-4.5 V	118 mAh/g at 0.1 A/g	*Energy Environ.Sci*., **2012,** 5 , 5437-5444
Reduced graphene oxide(2.5 µm)[143]	1.5-4.5 V	125 mAh/g at 0.137 A/g	*ACS Appl. Mater. Interfaces*, **2013,** 5 , 12295-12303.
Biomass-derived carbon + FWNT[109]	1.5-4.5 V	150 mAh/g at 0.1 A/g	*Nanoscale*, **2016**, 8, 3671-3677.

The assembled electrodes showed stable cycling stability up to 3,000 cycles with their coulombic efficiency values close to ~100% (**Fig. 4.9a**). During the initial several hundred cycles, the specific capacities slightly increased, approaching a stable capacity of ~170 mAh/g. This capacity is comparable or higher than those of

the reported carbon based free-standing positive electrodes (117~160 mAh/g) (**Table 4.1**).[109, 116, 122, 141-143] The increased capacity during the initial several hundred cycles may be attributed to the gradual electrolyte diffusion into the electrode surface and the activation of functional groups within the electrode. Comparison of the voltage profiles of the electrodes showed no dramatic change between 100th and 3000th cycles (**Fig. 4.9b**).[5, 78, 122] During the cycling process, the electrode well maintained its initial hierarchical structure (**Fig 4.10a**). In addition, the main oxygen functional groups on the cycled electrode showed negligible difference compared to the initial surface chemistry before cycling (**Fig 4.10b**). The stabile cycling stability can be attributed to the surface limited charge storage mechanisms, including both double-layer capacitance and surface redox reactions.

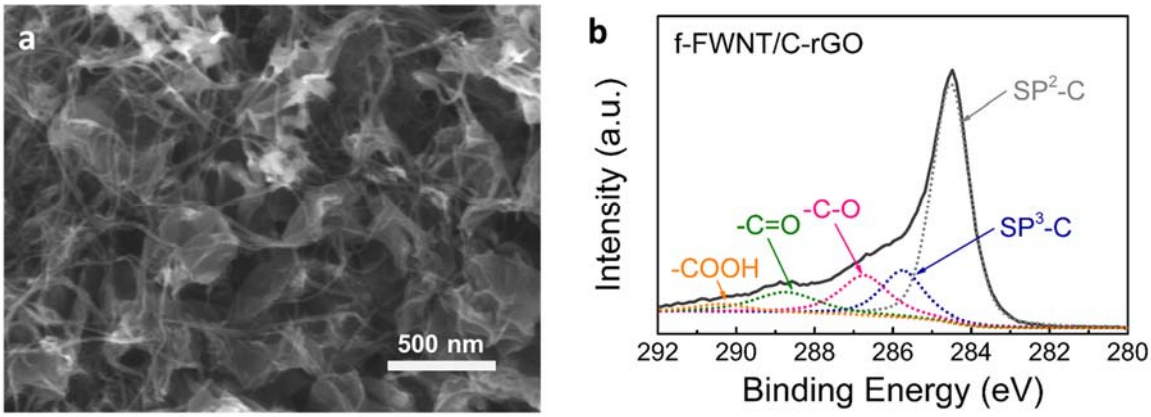

Figure 4.10 (a) SEM image of the f-FWNT/r-CGO electrode after 3000 cycles. (b) XPS high-resolution C1s spectra of the f-FWNT/r-CGO after 3,000 cycles.

4.5 Conclusions

In summary, we have demonstrated the effective utilization of the surface redox reactions on the r-CGO for enhanced electrochemical energy storage. The r-CGO was assembled as free-standing electrodes with the f-FWNT via VF process. The assembled f-FWNT/r-CGO electrode showed a 3D hierarchical porous structure, enabling fast ion and electron transport through the electrode. The f-FWNT/r-CGO electrode exhibited higher gravimetric capacity and significantly enhanced rate-capability compared to those of the compositionally similar, yet geometrically different f-FWNT/rGO electrode. Thus, the superior electrochemical performances of the f-FWNT/r-CGO electrodes can be attributed to the 3D hierarchical nanostructures, which can provide not only efficient electron pathways but also facilitate fast ion diffusion to support fast surface redox reactions. The results provide meaningful insights on the microstructure design of the functionalized carbon electrodes for the effective utilization of their surface redox reactions, which can be directly incorporated for the development of high-power Li-ion capacitors or LIBs.

CHAPTER 5.

STACKING-CONTROLLED ASSEMBLY OF CABBAGE-LIKE GRAPHENE MICROSPHERE FOR CHARGE STORAGE APPLICATION

5.1 Overview

In order to synthesize graphene (GR), the solution-based chemical oxidation process of graphite is most commonly used because it is facile, low cost, high yield, and is likely to be commercialized.[92, 156] Since the final product is an oxidized form of GR, graphene oxide, this process inevitably requires a subsequent chemical or thermal reduction reaction to convert GO to reduced GR.[24, 157] However, during the drying process for electrode preparation, as-prepared GR sheets tend to be restacked by the π-π stacking and van der Waals attraction to form agglomerates, thereby reducing the available surface area and ion diffusion channels within electrodes.[47, 92] As such, preventing restacking of the GR sheets has been considered to be an important issue to maximize charge storage performance for GR-based energy storage devices.[32]

To address the restacking issue, various 3D-structured GR electrodes have been explored. For example, the physical spacers, such as carbon black and carbon nanotube,

were inserted between GR sheets during the vacuum filtration process.[40, 141] In addition, self-assembled hydrogel was synthesized via hydrothermal process, producing the 3D aerogel electrodes after the freezing-drying process.[32, 124, 158-159] Despite their enhanced electrochemical performances,[159] the size of the 3D-structured GR is largely limited by the apparatus, such as filtration funnels and hydrothermal reactors, limiting the large-scale production. Exceptionally, crumpled GR, which has an aggregation-resistive characteristic, has been shown to be capable of large-scale production through a continuous aerosol-pyrolysis process of GO solution.[2, 32, 137] However, the density (<0.5 g cm^{-3}) of the 3D-structured GR including crumpled GR is relatively low due to the presence of the internal bulk void space compared to that of conventional activated carbon (0.5~0.8 g cm^{-3}).[137, 160] Thus, these 3D-structured GR electrodes have limited volumetric energy density, which can increase the form factor of the energy storage devices. Improving the packing density of the GR electrode inevitably involves stacking of the GR sheet. Therefore, it is urgently required to develop a scalable production process of high-density GR through an optimized stacking process that maximizes electrochemical charge storage performance of electrodes.

5.2 Approach

Herein, we introduce a controllable and scalable stacking-engineering process of GR to produce high-density cabbage-like GR microsphere with a promising charge storage performance. The cabbage-like graphene (C-GR) microspheres can be continuously produced in powder form through solution-based pre-stacking process and subsequent aerosol densification process. The C-GR shows a mesoporous structure with a high density of 0.75 g cm^{-3}, which is comparable to that of the conventional activated carbon (0.5~0.8

g cm^{-3}).[137, 160] The C-GR electrodes for aqueous symmetric supercapacitor show higher gravimetric (177 F g^{-1}) and volumetric (117 F cm^{-3}) capacitances than those of 3D crumpled GR electrode (156 F g^{-1} and 42 F cm^{-3}). Moreover, the C-GR electrodes exhibit a high specific capacity of ~176 mAh g^{-1} when applied to the cathode of a Li-half cell. We believe that the introduced stacking-control strategy of GR could be expanded to other 2D materials to enhance the charge storage performance for various energy storage applications.

5.3 Experimental Methods

5.3.1 Sample Preparation

Colloidal graphene oxide (GO) was synthesized from graphite (Alfa Aesar, 74 μm) by modified Hummers and Offeman's method [144]. The GO dispersion of 0.5 wt.% was reacted with a controlled concentration of urea (≥98% purity, Alfa Aesar) at 100 ºC with stirring for 12h to convert the GO sheets to moderately stacked GR particles. After the liquid phase reduction, the GR colloid was nebulized into a pre-heated chamber (200 ˚C) by aerosol spray process using a standard nozzle (0.7 mm in diameter). The nebulized droplets are rapidly evaporated inside the pre-heated chamber to produce cabbage-like graphene (C-GR) powder. The collected C-GR powder was thermally annealed at 250 ºC for 2 h under Ar environment. The crumpled GR was prepared by the similar method to the C-GR without the liquid phase reduction process with urea.

5.3.2 Material Characterization

Morphology of the C-GR microsphere was characterized by SEM equipped with EDX (Hitachi SU8230) and TEM (JSM-6380LA, JEOL). The specific surface area and pore size were characterized by analyzing the N_2 adsorption-desorption isotherms (Tristar 3000, Micromeritics). Surface chemistry was analyzed by XP) (Thermo Fisher Scientific).

5.3.3 Electrochemical Measurement

The electrochemical behavior of the C-GR for ECs was characterized by CV scan, GCD and EIS measurements using symmetric configuration of the two C-GR electrodes (HS FLAT CELL, HOHSEN Corp). The C-GR electrodes were prepared with the polyvinylidene difluoride (PVDF) (mass ratio, GR: PVDF=9:1) using n-methyl-2-pyrrolidone (NMP) solvent. The C-GR electrodes were controlled with an area of ~2 cm^2 and mass loading of 5 mg per electrode. KOH solution (5 M) was used as the electrolyte; a piece of filter paper (Waterman, GF/C) was used as a separator. The C-GR was also investigated as a cathode material for Li-ion batteries (LIBs). The C-GR particles (75 wt.%) were mixed with CNTs in deionized water and ethanol (volume ratio, 1:3). The mixture was filtrated and then the obtained free-standing film was mechanically pressed. The density of the free-standing film was found to be ~0.65 g cm^{-3} and loading density of the film based on the mass of C-GR was controlled to ~6 mg cm^{-2}. Two-electrode type Swagelok cells were employed for Li-cell assembly. A piece of Li and the free-standing film were used as the anode and the cathode, respectively. Two pieces of Celgard 2500 and 1 M $LiPF_6$ in EC:DMC (3:7 volume ratio, BASF) were used as separators and an electrolyte, respectively. The CV scans were performed in the potential window of 1.5-4.5 V vs. Li. GCD tests were carried out in the voltage window of 1.5-4.4 V vs. Li at the varied

current density from 0.1 A g^{-1} to 5 A g^{-1}. At each end of charge and discharge, the potential was held for 30 min at either 4.4 V or 1.5 V vs. Li. The cycling stability was tested using an accelerated cycling method.[161] First, the cell was cycled for 99 cycles at 5 A g^{-1} and then capacity was measured at 0.1 A g^{-1}. The capacity was normalized based on the mass of C-GR.

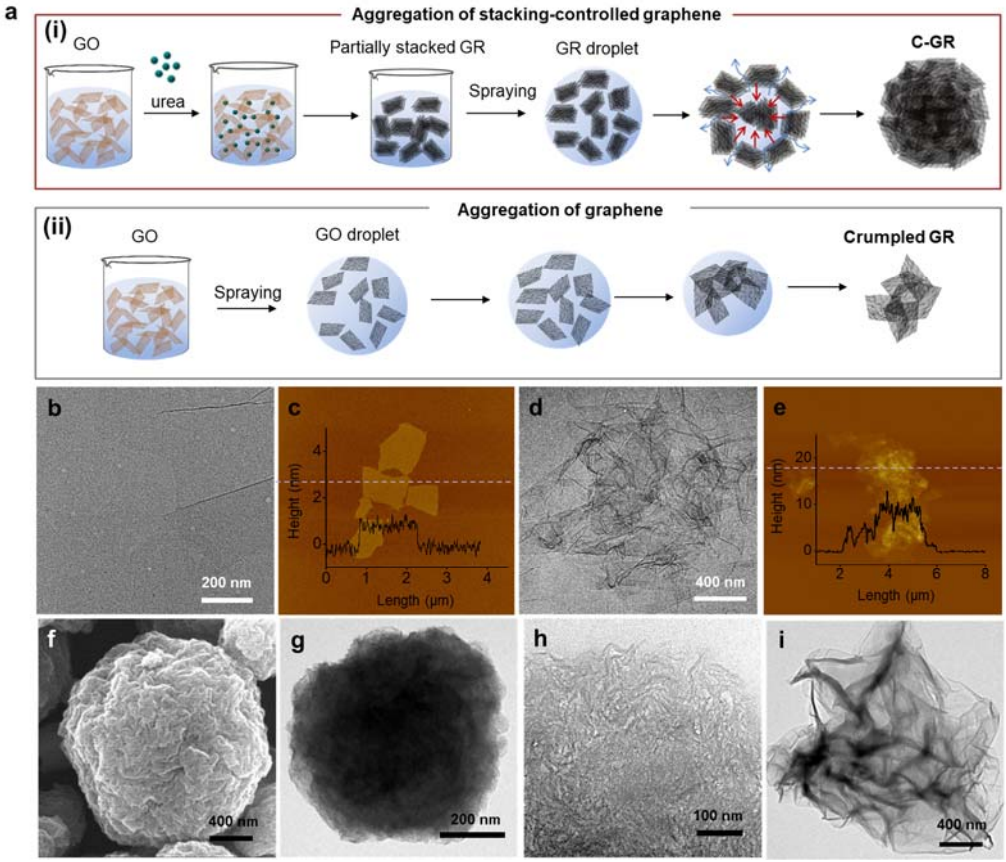

Figure 5.1 (a) Schematic illustrations of the stacking-controlled C-GR microsphere and crumpled GR synthesis. Morphologies of (b,c) GO and (d,e) moderately sacked graphene by TEM and AFM. (f) Morphology investigation of the C-GR by SEM. (g) Cross-sectional TEM image of the C-GR. The specimen for cross-sectional imaging was prepared by ion-milling. TEM images of the (h) C-GR and (i) crumpled GR. The C-GR was prepared from the liquid phase reaction of 0.5 wt.% GO and 1 wt.% urea for 12 h.

5.4 Results and Discussion

A schematic diagram of the C-GR synthesis is illustrated in **Fig. 5.1a**. The C-GR was prepared by liquid phase mild-reduction of GO with urea and subsequent densification of the partially reduced and stacked GO through an aerosol spray process. First, GO was dispersed in water and then a controlled amount of urea as a mild reduction agent was dissolved where the concentration of GO and urea were 0.5 wt.% (5 mg mL^{-1}) and 1 wt.% (10 mg mL^{-1}), respectively. Then, the mixture was maintained at 100°C for 12 h with stirring. In aqueous solvent, the monolayer GO sheets can maintain a stable dispersion due to the electrostatic repulsion between GO sheets.[92] However, during the liquid phase reduction reaction with urea, the oxygen functional groups of GO, which is the origin of the electrostatic repulsion, is partially removed and reduced.[92, 162] At this stage, the repulsion force between the GR sheets can be considerably weaken and van der Waals (vdW) interaction between them increases. When the graphene-solvent interaction is insufficient to compensate for the vdW interaction, aggregation of graphene sheets can occur. It is known that water molecules cannot efficiently solvate graphene sheets owing to the high steric repulsion between the water molecule and graphene, and the uncompensated vdW interaction between the GR sheets induces agglomeration of the GR sheets.[163-164] Before the liquid phase reduction process, the GO sheet showed a flat shape with a thickness of 1 nm (**Fig. 5.1b,c**). On the other hand, after the liquid phase reduction with urea, the obtained products displayed a winkled, partially aggregated morphology with a size of about 1 μm and a thickness of 8 nm (**Fig. 5.1d,e**), indicating the moderate stacking of the reduced GR sheets.[157] When the colloid is sprayed into the droplets, each droplet contains a number of the partially-stacked GR sheets therein. As the droplets pass

through a pre-heated furnace with an inert carrier gas, the partially-stacked rGR sheets in the droplets are further aggregated and densified by the capillary force, generating agglomerates (C-GR) in the form of microspheres (**Fig. 5.1f,g**).[137, 165] Then, the obtained C-GR microspheres were thermally annealed at 250 °C for 2 h under an inert gas atmosphere. The C-GR microsphere showed a high density of 0.75 g cm^{-3}. Despite such high density, nano-sized void spaces were found in the C-GR (**Fig. 5.1h**), which can serve as efficient diffusion channels for charge storage. For comparison, crumpled GR was also prepared by aerosol spray pyrolysis method without the liquid phase reduction process. The crumpled GR particles exhibited a wrinkled and quasi-spherical morphology with a bulk void (**Fig. 5.1i**). Due to the bulk void, the crumpled GR showed a much lower density of ~0.30 g cm^{-3} than the C-GR.

The pore size distribution of C-GR was investigated by Barrett-Joyner-Halenda (BJH) method (**Fig. 5.2a**). The C-GR contains a narrow range of mesopores (2~4 nm), while the crumpled GR has no obvious pore structure. The pore volume of C-GR was measured to be 0.428 cm^3 g^{-1}, which was much higher than that of crumpled GR (0.075 cm^3 g^{-1}) (**Fig. 5.2a**). It is also known that the introduction of the micro-to-mesopores can improve the charge storage capability, but the large introduction of pore may decrease the low volumetric energy density.[153, 158, 166] Herein, the high density C-GR having a narrow-range mesopores can have advantages for charge-storage applications. The surface chemistry of the C-GR and crumpled GR was investigated by XPS (**Fig. 5.2b-d**). The C-GR showed the atomic ratio of oxygen to carbon (O/C) of 0.19, which is lower than that of crumpled GR (0.24), probably due to its additional liquid-phase reduction process (**Fig. 5.2b**). The C-GR exhibited a fine peak of N 1s (N/C ratio, 0.04), but the crumpled GR has

no N 1s peak. This can be attributed to a slight amount of nitrogen doping during the pre-reduction process with urea.[23] The high-resolution C 1s spectra of the C-GR and crumpled GR were fitted by five characteristic peaks: 284.6 ± 0.1 eV for sp^2-hybridized carbon, 285.5 ± 0.1 eV for C–N, 286.4 ± 0.2 eV for C-O, 287.8 ± 0.2 eV for C=O, and 288.9 ± 0.3 eV for COOH.[117, 167] The peak intensities of oxygen peaks of the C-GR were relatively lower than those of the crumpled GR, indicating more reduced state of the C-GR.

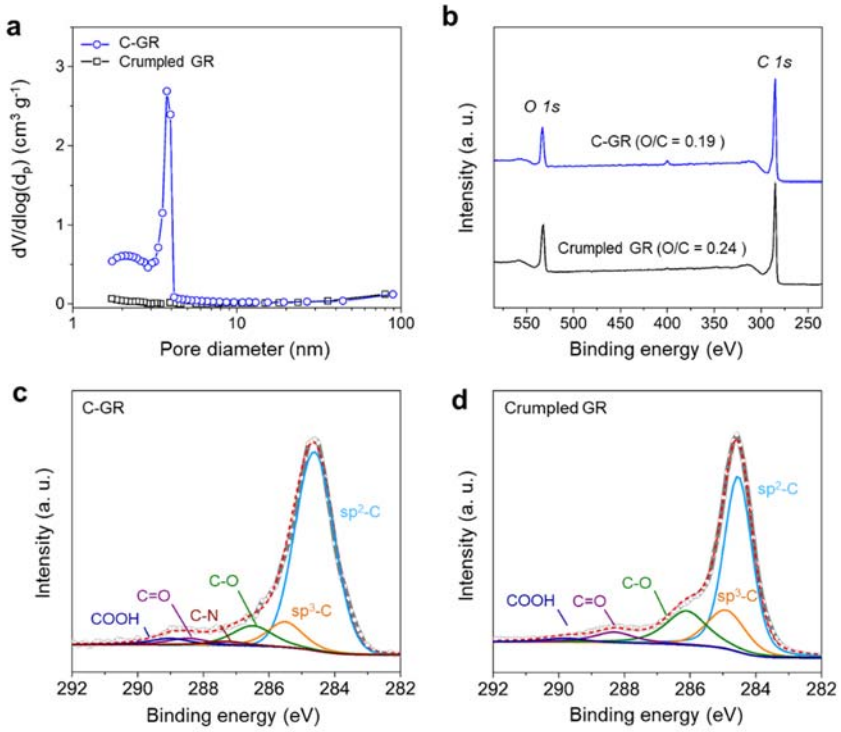

Figure 5.2 (a) Pore size distribution and (b) XPS wide scan survey of the C-GR and crumpled GR. High-resolution XPS C1s spectra of (c) C-GR and (d) crumpled GR.

To investigate the effect of the urea concentration and thermal treatment on the structure of the C-GR, we prepared various C-GR microspheres from different

concentrations of urea with or without heat treatment. As the urea concentration increased from 1 to 3 wt.%, the average particle size increased from 0.67 to 1.4 μm regardless

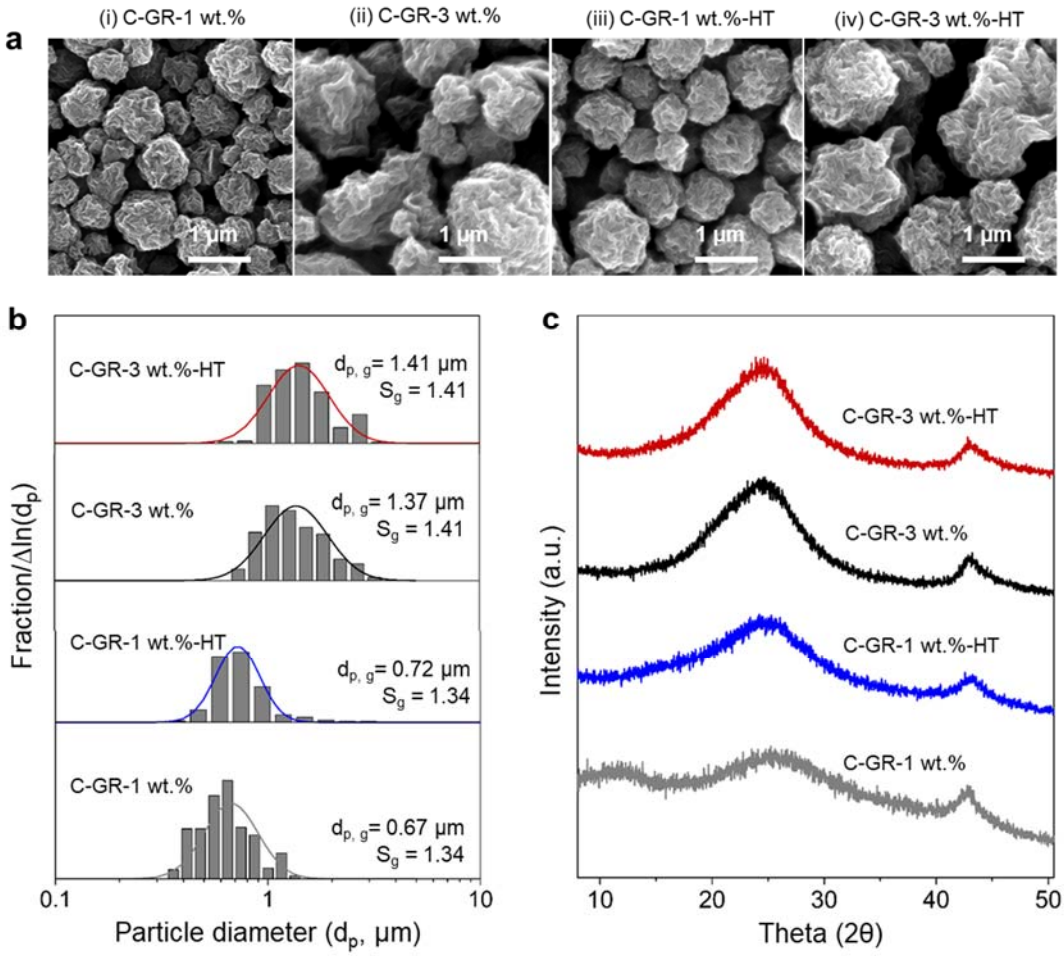

Figure 5.3 (a) Scanning electron microscope images, (b) particle size distribution, and (c) X-ray diffraction patterns of the C-GR prepared at different urea concentration with and without heat treatment.

of the heat treatment (**Fig. 5.3a,b**). Using higher concentration of urea, the GO sheets can be converted to further reduced GR sheets and more agglomerated GR flakes can be formed during the liquid phase reduction process, resulting in a larger microsphere after the aerosol densification process.[168-169] The XRD patterns of the various C-GR microsphere showed a

distinct peak around 25° with an interlayer distance of ~3.56 Å. (**Fig. 5.3c**). This peak was also found in the previous research on the highly-packed 3D reduced GR assembly.[122] This peak sharpened with increasing urea concentration, indicating more ordered packing of the GR sheets due to the more reduction process with urea. The C-GR prepared with 1 wt.% urea without heat treatment (C-GR-1 wt.%) showed a small peak at 10.5°, which is commonly found in stacked GO, indicating that GO was insufficiently reduced at the dose of low concentrated urea (**Fig. 5.3c**).[2]

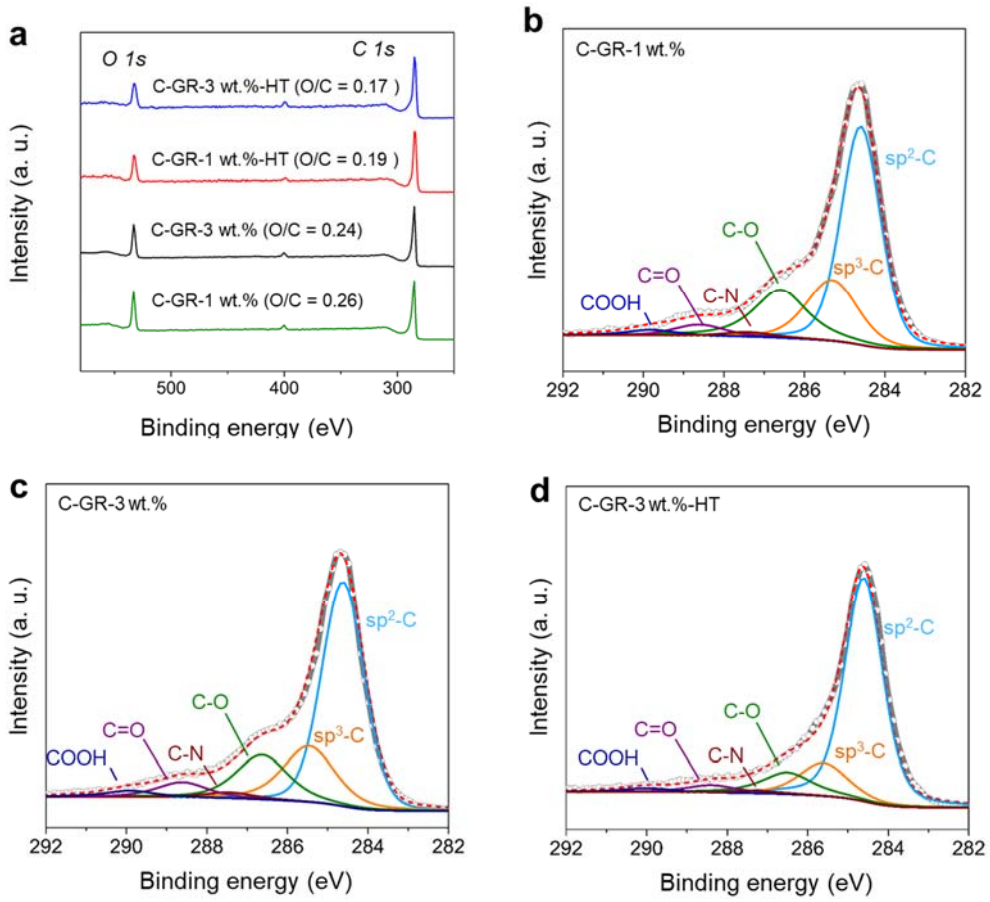

Figure 5.4 (a) XPS wide scan survey of the C-GRs prepared at different urea concentrations with/without the heat treatment (HT). C1s spectrum of the C-GR prepared at (b) 1 wt.% and (c) 3 wt.% urea. (d) C1s spectrum of the C-GR prepared at the urea concentration of 3 wt.% after the heat treatment.

Table 5.1 Atomic fraction of the functional groups on the C-GRs prepared at different urea concentrations with/without the heat treatment.

C-GR preparation	Fitting of the C 1s peak for relative atomic percentage [%]					
	C=C (sp^2)	C-C (sp^3)	C-N	C-O	C=O	O-C=O
C-GR-1 wt.%	0.54	0.20	0.02	0.18	0.04	0.02
C-GR-3 wt.%	0.57	0.18	0.02	0.16	0.05	0.02
C-GR-1 wt.%- HT	0.69	0.13	0.02	0.11	0.03	0.03
C-GR-3 wt.%-HT	0.71	0.13	0.02	0.10	0.04	0.01

After the mild thermal annealing at 250 °C for 2 h under Ar environment, the small peak disappeared, which can be attributed to the further restoration of pi-pi band on the GR sheets [19]. The surface chemistry of the various C-GRs was analyzed by XPS (**Fig. 5.4 and table 5.1**). The O/C ratio and detailed oxygen chemistry analysis showed that the oxygen functional groups gradually decreased with increasing urea concentration and thermal annealing process. The effect of GO concentration for the synthesis of the C-GR was also investigated using different concentrations of GO colloid (0.1~0.5 wt.%) (**Fig. 5.5**). Interestingly, as the GO concentration increased from 0.1 to 0.5 wt.%, the average size of the C-GR microspheres slightly increased from 0.67 to 0.81 μm (**Fig. 5.5a,b**). Such an increase in size is due to the larger numbers of GR sheets present in a single sprayed

droplet. These results indicate the possibility of finely tuning the particle size and packing degree of the C-GR.

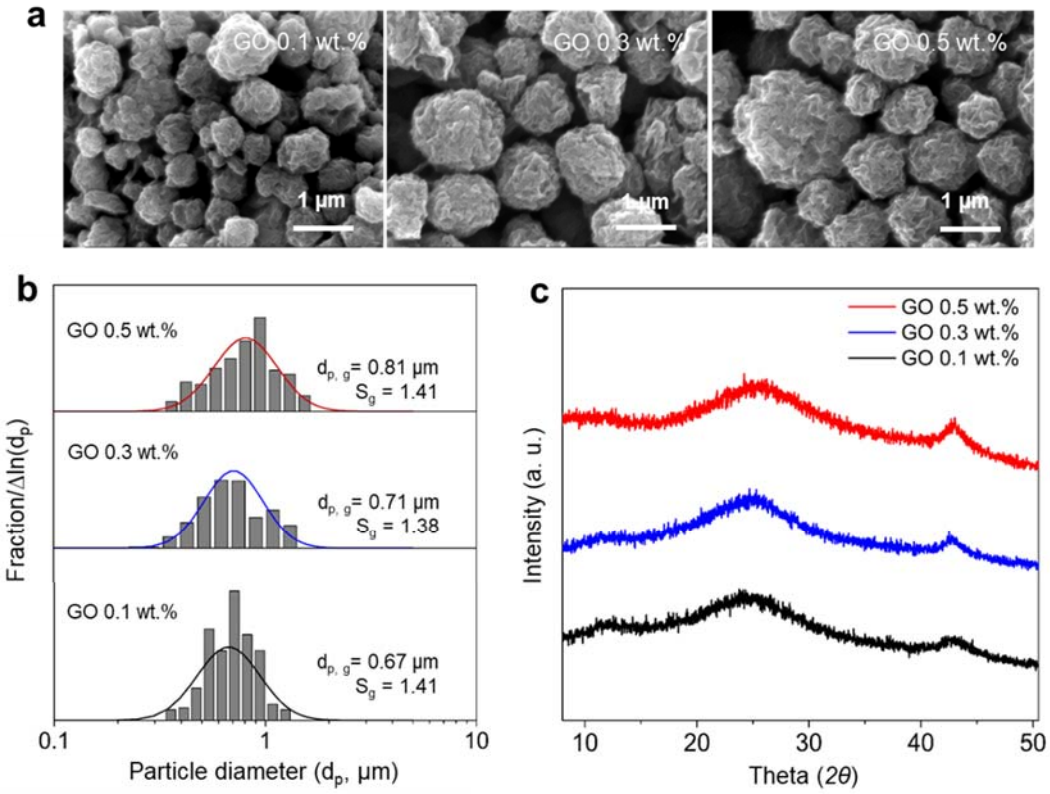

Figure 5.5 Effect of GO concentration on the C-GRs. (a) Morphology, (b) particle size distribution, and (c) XRD patterns of the C-GR prepared at different concentrations of GO (0.1~0.5 wt.%). The C-GR was prepared at a fixed urea concentration (1.5 wt.%) and liquid-phase reduction time (12 hours).

Electrochemical performance of the various C-GRs was investigated using a symmetric two-electrode electrochemical capacitor assembly (**Fig. 5.6 and Fig. 5.7**). The heat-treated C-GRs showed box-shaped CV profiles at the scan rate of 20 mV s^{-1}, indicating general capacitive charge storage behavior (**Fig. 5.6a**).[170] The GCD profiles of the C-GRs showed a shape very close to the isosceles triangle, further confirming the capacitive charge storage characteristics (**Fig. 5.6b**). The detail GCD profiles of the heat-treated C-GR

prepared with 1 wt.% urea (C-GR-1 wt.%-HT) as a function of the current density showed no apparent voltage drop near the upper cutoff voltage (**Fig. 5.6c**), indicating small internal resistance of the electrode materials [66]. From the GCD profiles, we calculated the capacitance of the C-GRs with different urea conditions as a function of the current density (**Fig. 5.6d**). Despite very similar surface chemistry of the heat-treated C-GRs prepared with different urea concentrations, the C-GR-1wt.%-HT showed the higher specific capacitance (177 F g^{-1} at 0.1 A g^{-1}) than that of the C-GR-3wt.%-HT (138 F g^{-1} at 0.1 A g^{-1}) (**Fig. 5.6d**).

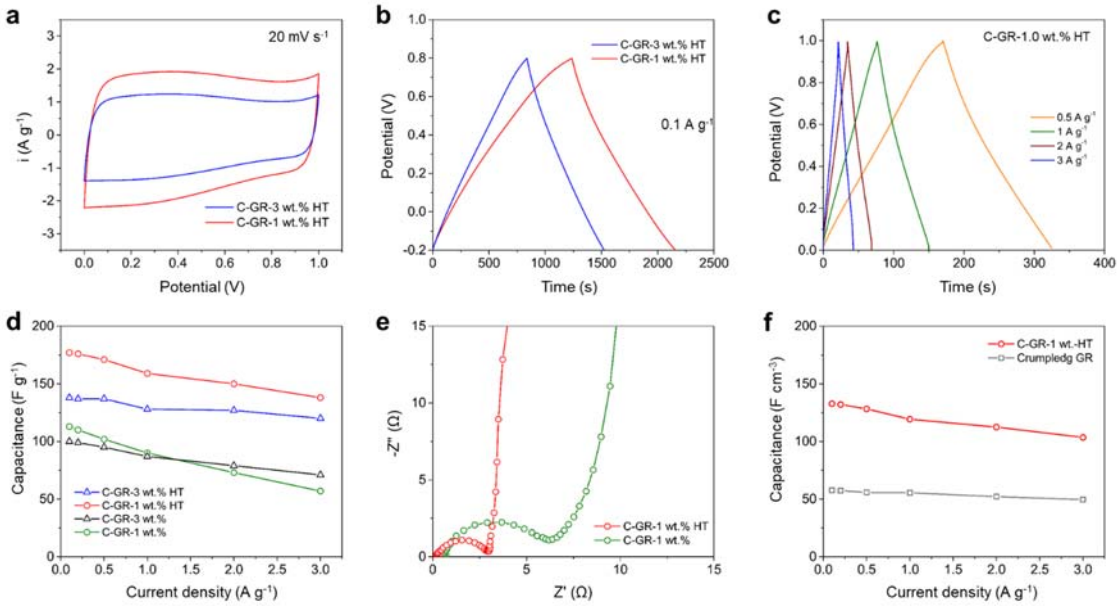

Figure 5.6 (a) CV scans and (b) GCD profiles of the heat-treated (HT) C-GRs prepared at varied urea concentrations of 1~3 wt.%. (c) GCD profiles of the heat-treated C-GR prepared with 1 wt.% urea. (d) Rate-dependent gravimetric capacitance and (e) EIS of the various C-GRs. (f) Rate-dependent volumetric capacitance of the heat-treated C-GR (1 wt.% of urea) in comparison with crumpled graphene.

It is important to note that that, prior to the heat treatment, the C-GR-1 wt.% (113 F g^{-1} at 0.1 A g^{-1}) showed similar capacitance to the C-GR-3 wt.% (100 F g^{-1} at 0.1 A g^{-1}). (**Fig. 5.6d**). However, the capacitance of the C-GR-1 wt.% was largely enhanced from 113 F g^{-1} to 177 F g^{-1} after the heat treatment, whereas the increase in capacitance was relatively small (from 100 F g^{-1} to 138 F g^{-1}) for C-GR-3 wt.%. The low capacitance of the C-GRs before the heat-treatment can be attributed to their high O/C ratios (0.24~0.26) and corresponding low electrical conductivity. To further understand the capacitance trend of the C-GRs during to the heat treatment, EIS was carried out. After the heat treatment, the C-GR-1 wt.%-HT showed significantly reduced resistance than the C-GR-1 wt.%, which is indicated by the decreased diameter of the semi-circle in the Nyquist plots (**Fig. 5.6e**). This confirms improved electrical conductivity through the thermal reduction process, which is supported by the XPS results.

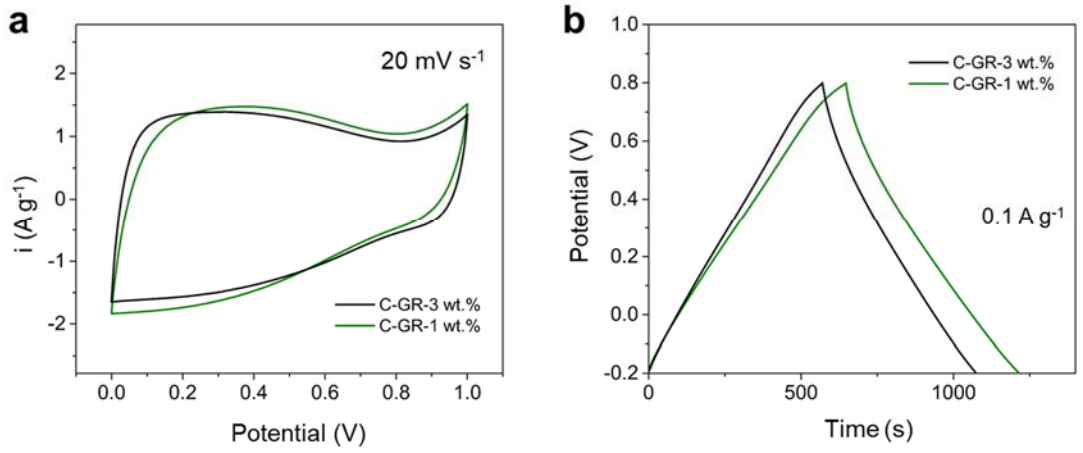

Figure 5.7 (a) CV scans and (b) GCD profiles of the C-GR prepared at varied urea concentration of 1.0~3.0 wt.% without the heat treatment.

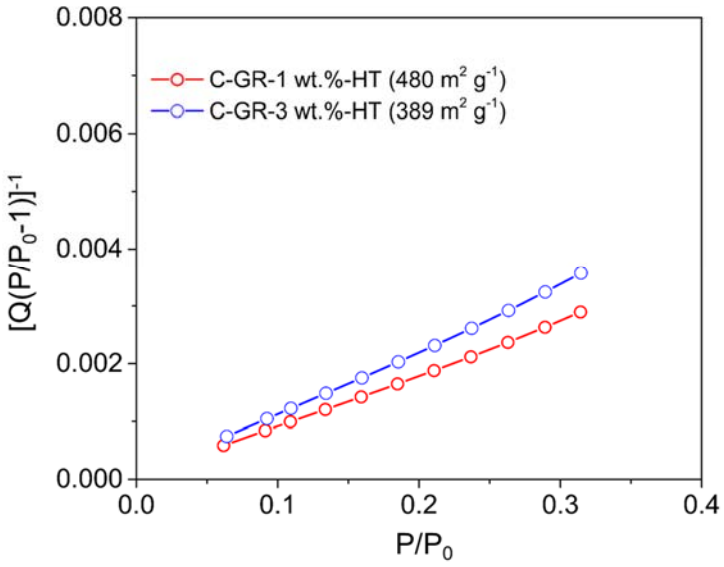

Figure 5.8 Multi-point BET plot of the heat-treated C-GRs prepared with the different concentrations of urea.

In order to understand the difference in capacitance between the C-GR-1 wt.%-HT and the C-GR-3 wt.%-HT, we measured their specific surface area. The C-GR-1 wt.%-HT showed higher surface area of 480 $m^2 g^{-1}$ than that of the C-GR-3 wt.%-HT (389 $m^2 g^{-1}$) (**Fig. 5.8**). This indicates that the use of excessive urea during the liquid-phase reduction process leads to more severe stacking, decreasing the specific surface area available for charge storage. The volumetric specific capacitances of the C-GR-1 wt.%-HT was compared with the crumpled GR (**Fig. 5.6f**). The electrode densities of the C-GR and crumpled GR were found to be ~0.66 g cm^{-3} and ~0.27 g cm^{-3}, respectively. Based on the electrode density values, the volumetric capacitances of the the C-GR-1 wt.%-HT and crumpled GR were calculated to be 117 F cm^{-3} and 42 F cm^{-3} at 0.1 A g^{-1}, respectively. The higher volumetric capacitance of the C-GR than crumpled GR suggests that high electrical performance can be achieved by controlling the stacking process of GR sheets.

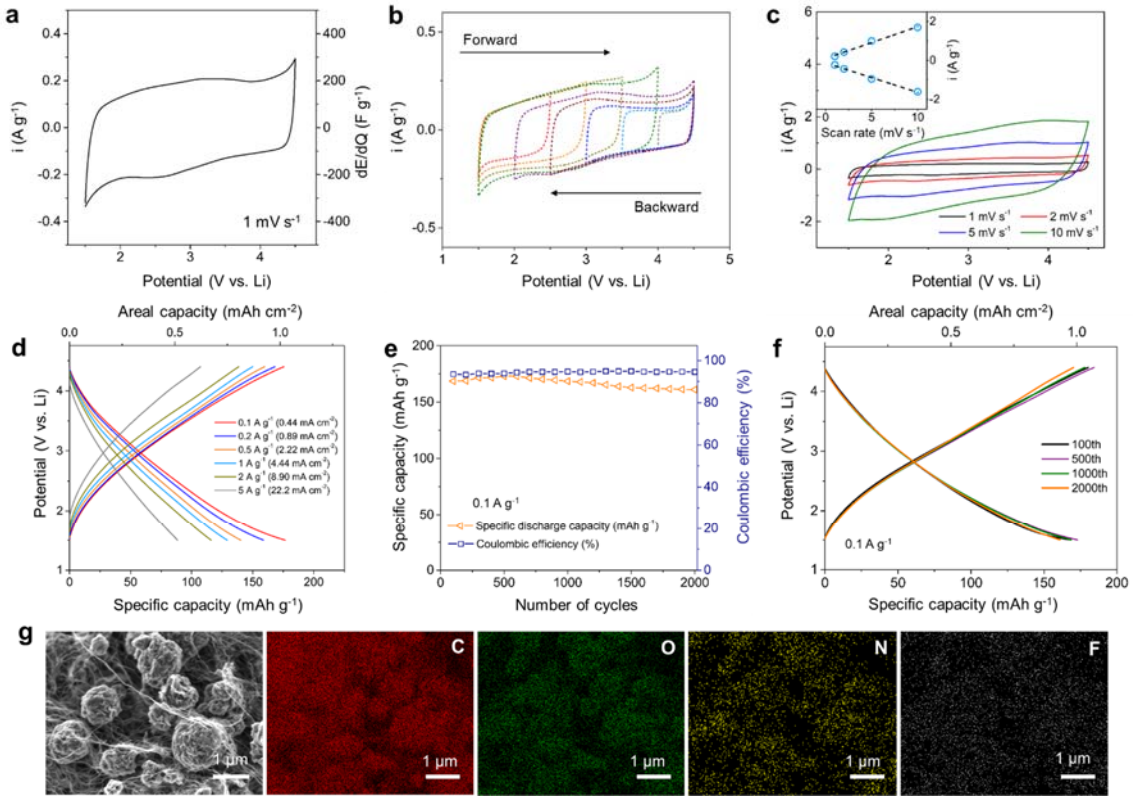

Figure 5.9 Electrochemical characterization of the C-GR-1 wt.%-HT as a cathode for LIBs. (a) CV scans at 1 mV s^{-1} in the potential window of 1.5-4.5 V vs. Li. (b) Potential-dependent and (c) rate-dependent CV scans of the C-GR. (Figure c inset shows rate-dependent cathodic and anodic peak current at 2.5 and 3.0 V vs. Li, respectively) (d) Galvanostatic charge/discharge profiles of the C-GR at different current densities from 0.1 to 5 A g^{-1} in the potential window of 1.5-4.4 V vs. Li. (e) Cycling performance test and (f) detailed voltage profiles at different cycles of the C-GR. (g) SEM image and EDX elemental mapping of the C-GR electrode after cycling.

Recently, oxygen functional group-containing nanocarbons, such as carbon nanotube and graphene, have been studied as cathodes for LIBs or Li-ion capacitors by utilizing the redox reaction between oxygen functional groups and Li-ions.[114, 116, 122] Since the heat-treated C-GR still contain a large amount of the oxygen functional groups, the electrochemical performance of the C-GR-1 wt.%-HT was evaluated as the cathode in Li-

half cells. The charge storage characteristics of the C-GR in LIBs were first investigated by CV scans at 1 mV s^{-1} in the potential window of 1.5-4.5 V vs. Li (**Fig. 5.9a**). The CV scan showed oxidation and reduction peaks around 2.5 and 3.0 V vs. Li, respectively, on top of the double-layer capacitance. These two peaks can be ascribed to the redox-reaction of the residual oxygen functional group (e.g., carbonyl group) on the C-GR surface with Li-ions.[2, 161] Thanks to the redox reactions as well as double-layer capacitance, the C-GR showed a high specific capacitance of 169 F g^{-1} (volumetric capacitance of 110 F cm^{-3}). To further confirm the charge storage mechanism, forward and backward potential-dependent CV measurements were performed for the C-GR (**Fig. 5.9b**). As the potential window increased from 1.5 to 4.0 V vs. Li or decreased from 4.5 to 2.0 vs. Li, the CV scans exhibited progressive evolution of the oxidation and reduction peaks around 2.5 and 3 V vs. Li, respectively. In the low potential region of 1.5-2.5 V vs. Li and high voltage range of 3.5-4.5 V vs. Li, the CV scans showed a box-like profile, indicating that the charge storage in these ranges mainly results from double-layer capacitance. Under the assumption of the constant double layer capacitance over the entire potential region, the estimated contribution of double-layer capacitance was found to be ~57%. The rate-dependent CV scans showed that the redox peak was well preserved up to a scan rate of 10 mV s^{-1} (**Fig. 5.9c**). The anodic and cathodic currents measured at 3.0 and 2.5 V vs. Li, respectively, were plotted as a function of scan rate (**Fig. 5.9c, inset**). These plots showed a strong linearity, indicating surface-controlled redox process.[113, 161]

Electrochemical performance of the C-GR was assessed by GCD tests in the potential window of 1.5-4.4 V vs. Li (**Fig. 5.9d**). The C-GR exhibited the sloped charge and discharge profiles due to the combined charge storage mechanisms of double layer

capacitance and redox reaction.[161] At a low current density of 0.1 A g^{-1}, the C-GR delivered a high reversible capacity of 178 mAh g^{-1} and areal capacity of 1.04 mAh cm^{-2}. As the current density increased to 1 A g^{-1}, which corresponds to a high areal current density of 4.44 mA cm^{-2}, the C-GR exhibited a discharge capacity over 125 mAh g^{-1}, maintaining 72% of its capacity. This high rate-capability can be attributed to the high surface area and hierarchical porous structure of the C-GR which promotes both capacitive and redox charge storage mechanisms. Moreover, the C-GR showed stable cycling performance up to 2,000 cycles with a high Coulombic efficiency of ~94% and an excellent capacity retention of 95.5% (**Fig. 5.9e,f and Fig. 5.10**). The SEM images of the cycled C-GR electrode showed that the cabbage-like morphology was well maintained after the intensive cycling process (**Fig. 5.9g**). Interestingly, F was found on the C-GR, which may be due to residual electrolyte salts. The stable cycling performance of the C-GR can be explained by the surface-limited charge storage mechanism that does not involve physical structural changes.[19]

5.5 Conclusions

We have synthesized that the C-GR microspheres with a high density of 0.75 g cm^{-3} using liquid-phase reduction reaction and aerosol spray drying process. Despite its high density, the C-GR had a narrow-ranged mesopores and high surface area. The C-GR showed a high specific capacitance of 177 F g^{-1} (117 F cm^{-3}) in aqueous symmetric supercapacitors. As a cathode for LIBs, the C- GR delivered a high capacity of 176 mAh g^{-1} (1.0 mAh cm^{-2}) and maintained its high capacity up to 2,000 cycles. This superior electrochemical performance demonstrates that the stacking-control approach could

provide new opportunities to achieve both high gravimetric and high volumetric performance of graphene-based electrodes. In addition, the manufacturing process of the C-GR is suitable for mass-production due to the continuous nature of the aerosol spray process. The micron-scale powder form of the C-GR can also be easily incorporated into commercial electrode fabrication process based on slurry-casting. Form a broader perspective, the introduced stacking-control approach can be extended to other 2D materials to control bulk density and charge storage properties for energy storage and conversion applications.

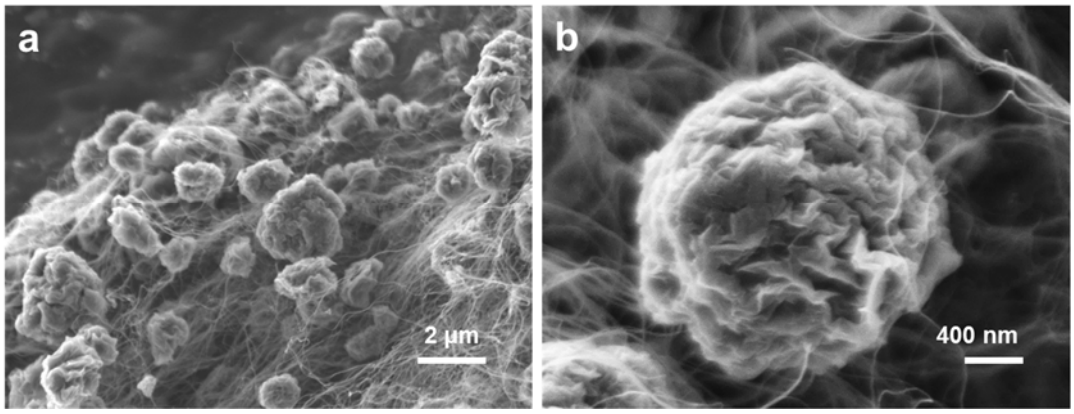

Figure 5.10 (a) Low- and (b) high-magnification scanning electron microscopy images of the heat-treated C-GR electrode after cycling test.

CHAPTER 6.

CRUMPLED GRAPHENE ANODE FOR ALKALI-ION BATTERIES

6.1 Overview

Due to growing concern over global warming in recent years, the electric vehicles (EV) market has expanded significantly.[171] Lithium-ion batteries (LIBs) have been primarily considered as the main power source for EVs.[171-172] However, the lack of mine reserves and uneven distribution of Li resources could be a central menace for sustainable growth in the EV market.[160] As such, sodium-ion batteries (SIBs) have been of great interest as a complementary option for the LIBs due to the availability of Na resources and cost advantages.[173]

Many electrode materials for LIBs cannot be applied to SIBs due to the different atomic properties between Li and Na.[174] For instance, graphite, a standard anode material for LIBs, hardly forms staged intercalation compounds with Na, showing a very limited capacity of 35 mAh g^{-1}.[175] The larger ionic size of Na (102 pm) over Li (76 pm) is often referred to as a culprit of difficulty in the formation of graphite intercalation compounds.[87] Recent study showed that intercalation of Na-ions into graphite can be achieved by expanding graphite to increase the interlayer distance of graphite.[176] This study suggested that the interlayer distance of graphite plays a crucial role for Na hosting and the minimal interlayer distance for Na-ion diffusion would be 0.37~0.43 nm.[176] Layered reduced graphene oxide materials with larger *d*-spacing of 0.37~0.38nm than ordinary graphite (0.34 nm) were also investigated for Na-ion storage.[89, 177] This approach, which increases *d*-spacing value to facilitate Na^+ insertion into graphene layers, showed an achievement of

high capacity (200~284 mAh g^{-1}) at low rates (0.1C~0.25C).[89, 176-177]. However, the expanded graphite and stacked graphene showed limited capacity less than 100 mAh g^{-1} at high rates (1C~5C). The large capacity drop at the high charge rate indicates that the Na^+ diffusion into graphitic host structure with increased *d*-spacing is still limited at high rates. Interestingly, despite the large ionic radius of potassium (137pm), graphite (*d*-spacing; 0.34nm) forms KC_8 with potassium and shows a higher capacity in K-ion batteries (KIB) than that in a SIB.[86, 178] Thus, the argument with the ionic radii is insufficient to fully understand fundamentals of alkali metal ion storage on aromatic carbon substrates. Goddard *et al.* have revealed that sodium has the weakest binding energy to an aromatic carbon substrate compared to the other alkali metal (Li and K) and accordingly graphite in SIB shows the lowest capacity.[48] This indicates that further increase of *d*-spacing may not work to improve the limited rate-capability of the expanded graphite and stacked graphene. Therefore, escaping from the thoughts of the d-spacing, totally different route for charge storage should be sought for Na storage.

6.2 Approach

One of the well-studied charge storage materials for alkali-ion batteries is hard carbon (HC). It is recognized that hard carbon (HC), which has a turbostratic structure,[97] stores Na ions through two mechanisms: A) Intercalation of Na-ions into host structure and B) surface-limited capacitive charge adsorption.[79, 179] In SIBs, charge storage of HC as an anode material is mainly done by the intercalation process so that almost all of HCs exhibit a high degree of carbonization and surface-capacitive process is considered as an ancillary charge storage source.[79] Considering the low capacity of graphite and low rate-capability

of the expanded graphite and stacked graphene in SIBs, utilization of the surface-capacitive charge storage rather than the intercalation could be a possible way to store Na-ions effectively. The surface-limited capacitive charge storage usually refers to the electrostatic charge storage found in double layer capacitors (EDLCs).[5] As such, graphene could be a promising candidate to aim the surface-limited capacitive charge storage since it has large surface area and high electrical conductivity of 2 x 10^3 S cm^{-1}.[48] Recently, it has shown that reduced graphene store charge through both of double layer capacitance and redox-reaction of oxygen functional groups to Li^+ and Na^+ in acceptable high voltage range.[78, 141, 180] However, in acceptably low voltage range for an anode (less than 2~2.5 V vs. Na), it seems that graphene's mechanisms for Na storage in a voltage range for anode application are still in veil.[89, 177, 181]

In this study, we reveal that graphene stores Na through two sub-routes of surface-capacitive charge storage: i) adsorption in a similar way of double layer capacitance on the surface of graphene and ii) adsorption on defective sites. For both scenarios, Na^+ ions exhibit the lowest adsorption energy when residing on hollow sites of the graphene rather bridge or top sites.[182] Here the defective sites refer to all what makes graphene's structure being biased from its typical structure of honeycomb-like sp^2 carbon (i.e., structural defects, nanovoids, residual functional groups, etc.). We employed crumpled graphene (CG) to avoid serious restacking of graphene sheets, which has an aggregation-resistive characteristic.[161] In SIBs, the CG, which mainly stores Na ions through the double layer capacitance on the surface, showed a limited capacity of (~74 mAh g^{-1} at 40 mA g^{-1} and ~19 mAh g^{-1} at 2 A g^{-1}). On the other hands, the activated CG (A-CG) stores Na ions through both the double layer capacitance and physical adsorption on defective sites with

a good electrochemical performance of ~ 279 mAh g^{-1} at 40 mA g^{-1} and 151 mAh g^{-1} at 2 A g^{-1}, indicating the utility of the defective sites to enhance electrochemical performance of graphene for Na-ion storage.

6.3 Experimental Methods

6.3.1 Sample Preparation

The activated crumpled graphene (A-CG) was prepared from aerosol spray pyrolysis of graphene oxide (GO) droplets and subsequent thermal annealing processes. First, GO was prepared by modified Hummer's method and the GO was adjusted to the concentration of 10 mg mL^{-1} in water. Then, the GO solution was nebulized into a pre-heated furnace chamber (100 °C) using a mini spray dryer with a flow of Ar (10 L min^{-1}). During the flight of the GO droplets inside the chamber, rapid evaporation of water occurs and crumpled graphene oxide (CGO) particles are obtained at the outlet of the chamber. The as-prepared CGO was thermally reduced at the varied temperature under Ar environment to produce crumpled graphene (CG). After calcination of the CG at the mild temperature under air, the A-CG was obtained.

6.3.2 Material Characterization

The morphology was investigated by scanning electron microscopy (SEM, Hitachi SU8230) and transmission electron microscopy (TEM, JEM-ARM200F). Surface chemistry was examined by X-ray photoelectron microscopy (XPS, Thermal Scientific K-alpha XPS instrument) and C1s peaks were fitted by XPSPEAKS 4.1. To investigation of

crystallinity, X-ray diffraction (XRD, X-Pert Pro alpha 1) and Raman spectroscopy (Thermo Nicolet Almega XR Dispersive Raman Spectrometer) were used.

6.3.3 Electrochemical measurement

Electrodes were prepared by mixing 80 wt% of the CG or A-CG with super P carbon black (MTI Corp.) and polyvinylidene fluoride (PVDF) in N-methyl-2-pyrrolidone. A small piece of alkali metals (Li, Na and K) was employed for a counter/reference electrode (two electrode set-up). Employed electrolytes and separators for a Li-, Na- and K-cell are shown in **Table 6.1**. The working electrodes were assembled into Swagelok type cells in a high purity Ar-filled glove glovebox (MBraun, O_2 and H_2O < 0.1 ppm). In Na-cells, cyclic voltammetry (CV) scans were carried out with a varied scan rate of 0.1~10 mV s^{-1} (Bio Logic VMP3). Galvanostatic charge/discharge (GCD) profiles were investigated with varied current density from 40 mA g^{-1} to 2 A g^{-1}. To evaluate cycling stability, A-CG was cycled at 0.5 A g^{-1} for 1,000 cycles. Then, the A-CG was further cycled up to 8,000 cycles using an accelerated cycling method. For comparison, rate-capability of the A-CG in Li- and K-cells was also investigated.

Table 6.1 Electrolytes and separators for Li-, Na- and K-cells

	Electrolyte	Separator	Voltage window
Li	1 M $LiPF_6$ in EC[a]:DMC[b] + 5% FEC[e]	Celgard 2500	0.01-2.5 V vs. Li
Na	1 M $NaClO_4$ in EC:PC[c] + 5% FEC	Glass fiber	0.01-2.5 V vs. Na
K	0.8 M KPF_6 in EC:DEC[d]	Glass fiber	0.01-3.0 V vs. K

a) Ethylene carbonate (EC), b) Dimethyl carbonate (DMC), c) Propylene carbonate (PC), d) Diethyl carbonate (DEC), e) Fluoroethylene carbonate (FEC)

6.4 Results and Discussion

The activated crumpled graphene (A-CG) was prepared from aerosol spray pyrolysis of the GO dispersion in water and subsequent thermal annealing processes (**Fig. 6.1a**). The aqueous GO dispersion (10 mg mL^{-1}) was sprayed into a pre-heated furnace at 100 °C with an Ar gas flow. During the flight of the GO droplets in the pre-heated furnace through the Ar gas flow, rapid evaporation of the water droplets occurs and the remaining GO sheets are partially stacked and crumpled by the capillary force, generating the 3D crumpled graphene oxide (CGO) (**Fig. 6.2**).[137, 161] The CGO showed a negligible change of oxygen functional groups during the transformation from a 2D planar structure to a 3D ball-shape due to the low-heating temperature of 100 °C and short flight time (**Fig. 6.3**). To convert CGO to crumpled graphene (CG), the CGO was thermally reduced at varied temperatures ranging from 500 to 1100 °C (denoted as CG-X, X indicates an annealing temperature) for 2h under Ar environment. Then, CG was further activated by the annealing process under air environment for 3h to introduce more defective sites on graphene. The activated CG

(A-CG) and CG maintained the unique 3D ball-shaped morphology of the CGO over the heat-treatment processes (**Fig. 6.4**). A ridge structure was observed on the surface of the A-CG, CGs, and CGO (**Fig. 6.4**). Selected area electron diffraction (SAED) analysis on the ridge area shows a (002) ring diffraction pattern corresponding to a *d*-spacing of 0.37 nm (inset, **Fig. 6.1d)**. The ridge structure is typically found in wrinkled or crumpled graphene formed by compressive forces.[137, 183] This ridge on CG can be considered as 'distortional graphite nanocrystallites'.[184] The high-resolution transmission electron microscopy (HRTEM) image of the ridge region showed a long-range disordered structure, indicating the partial stacking of graphene sheets (**Fig. 6.1e**). The *d*-spacing profiles of this region showed an average d-spacing of 0.37, which is consistent with the SAED result (**Figure 6.1f**).

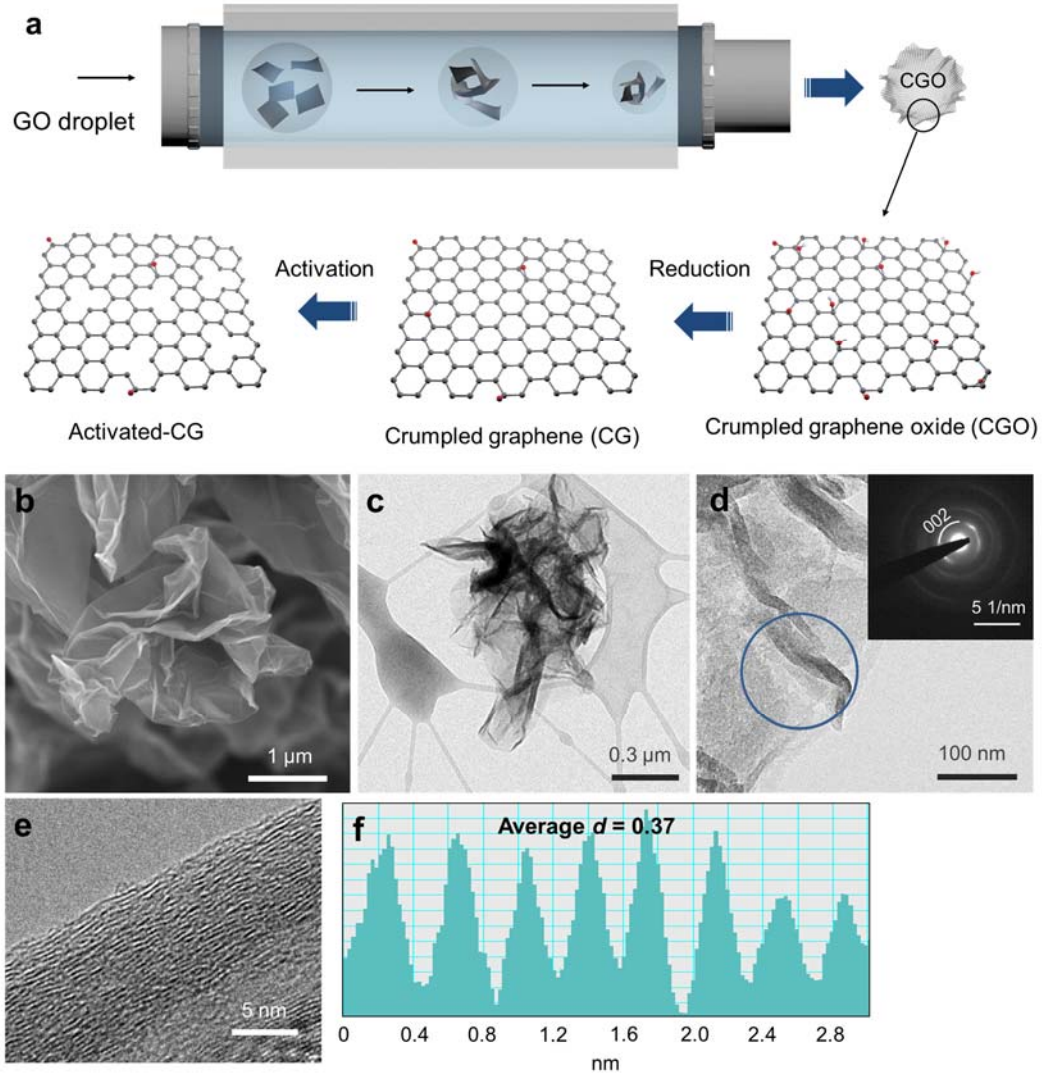

Figure 6.1 Characterization of activated crumpled graphene (A-CG) (a) Schematic illustration of the A-CG. (b) Scanning electron microscopy (SEM) and (c) transmission electron microscopy (TEM) image of the A-CG. (d) TEM image of the ridge structure on the A-CG at low magnification (Inset: Selected area electron diffraction, SAED pattern). (e) TEM image of the ridge at high magnification. (f) d-spacing profiles obtained from (e).

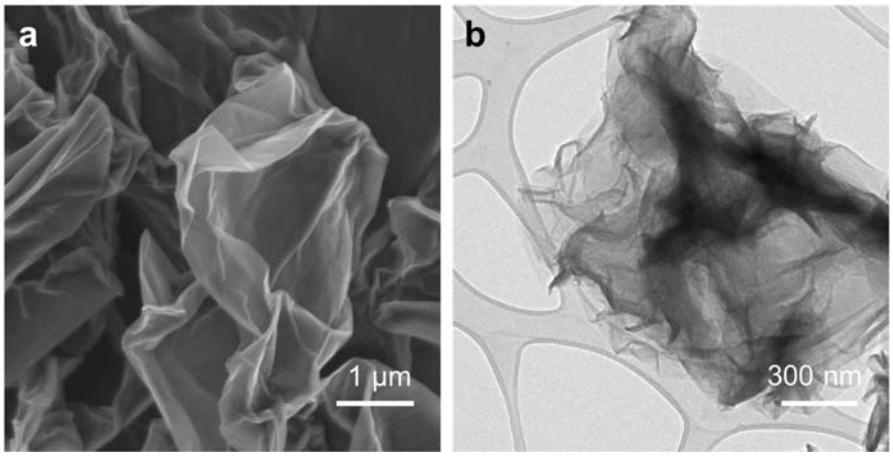

Figure 6.2 Morphology of crumpled graphene oxide. (a) Scanning electron microscopy (SEM) and (b) transmission electron microscopy (TEM) image. The crumpled graphene oxide shows a morphology like a highly wrinkled paper.

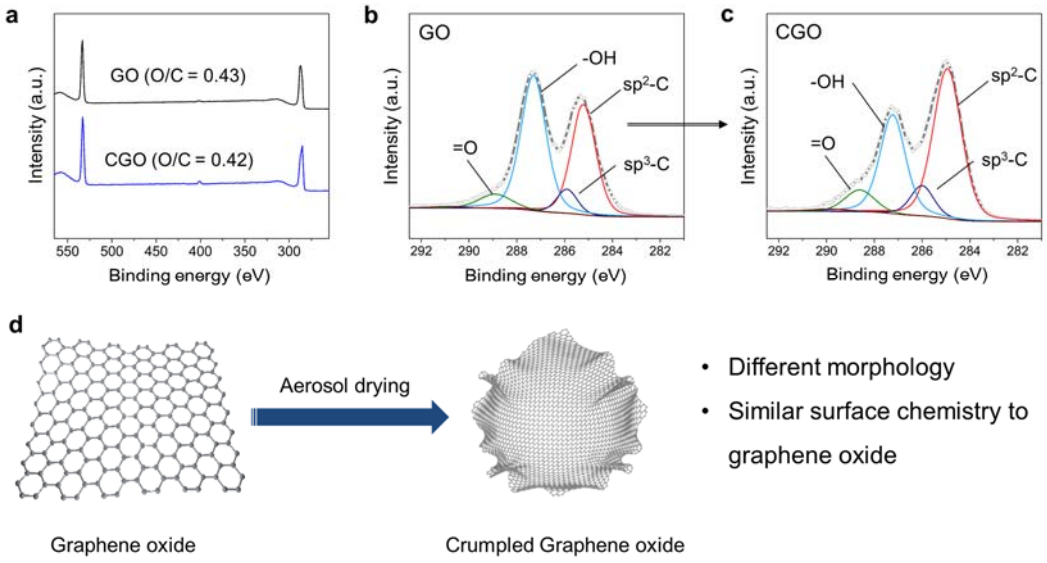

Figure 6.3 Surface chemistry of graphene oxide (GO) and crumpled graphene oxide (CG). (a) Wide scan survey of GO and CGO. High resolution C1s spectra of (b) GO and (c) CGO. C1s spectra were fitted by peaks for sp^2-C, sp^3-C, C-OH and C=O. (d) Schematic illustration of CGO compared to GO. During the aerosol drying process, planar morphology of GO is converted to being crumpled. But, surface chemistry of GO (i.e., oxygen-functional group), is reserved.

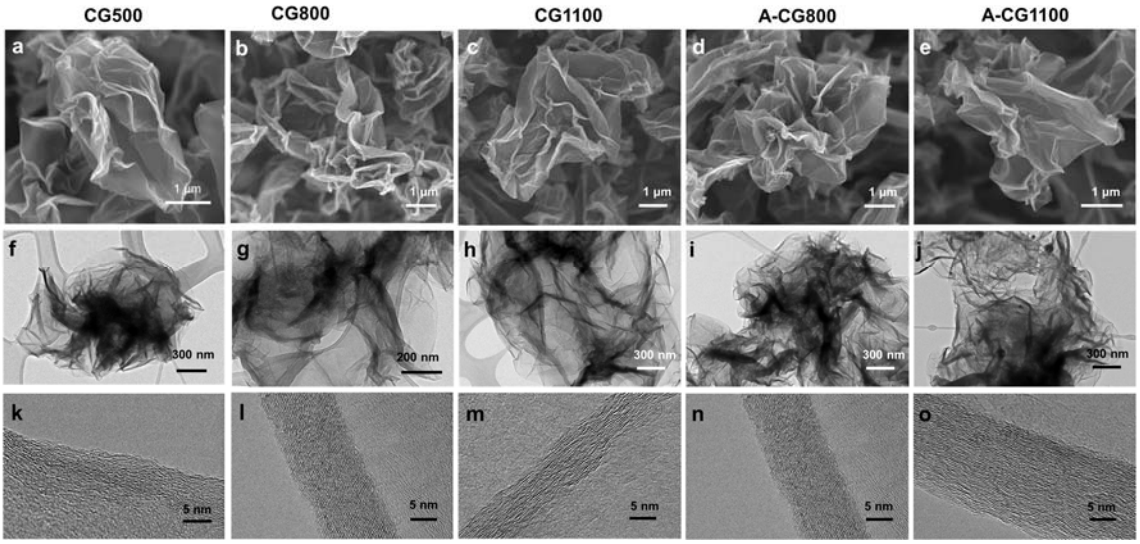

Figure 6.4 Morphology investigation of the A-CGs and CGs (a-e) Scanning electron microscopy (SEM) images and (f-j transmission electron microscopy (TEM) images of the various A-CGs and CGs. (k-o) TEM images on the ridge area of at high magnification. (a,f,k) CG500. (b,g,l) CG800. (c,h,m) CG1100. (d,i,n) A-CG800. (e,j,o) A-CG1100.

We first performed galvanostatic charge/discharge (GCD) tests for the CG-1100 at a C-rate of 40 mA g^{-1} (1C = 0.2 A g^{-1},[89]) in a Na-cell (**Fig. 6.5a**). The CG-1100 exhibited a sloped GCD profile with a discharge capacity of ~98 mAh g^{-1} in the potential region of 0~0.8 V vs. Na. Mitlin *et al.* also observed this sloping capacity in the study of carbonized peat moss anode for SIB.[185] They pointed out that the sloping capacity is associated with ion insertion into a material where the insertion sites possess a distribution of energies and a more disordered carbon could possess a wide site energy.[185] Similarly, the sloped discharge profile of the CG-1100 could be translated into a scenario that graphene store Na through capacitive way rather than intercalation process.[186] The A-CG-1100 also showed a similar sloped GCD profile, but its discharge capacity was significantly increased to ~222 mAh g^{-1} compared to that of the CG-1100 (~98 mAh g^{-1}). (**Fig. 6.5b**). Moreover, at the potential range of 0.8~2.0 V vs Na, the A-CG-1100 showed a discharge capacity of 35

mAh g^{-1} (~15.8% of total discharge capacity) whereas the discharge capacity of the CG1100 was 8 mAh g^{-1} (~8% of total discharge capacity). Considering the sloped voltage profiles of the CG1100 and A-CG1100,[185, 187] and the capacity increase of the A-CG1100 over the whole voltage window, it could be deduced that graphene store Na through two capacitive routes: I. 'Double-layer capacitive Na storage' and II. 'Na adsorption on defective sites.'[188] The route I and route II can be distinguished from their revelation voltage (**Figure 6.5a,b**). During the charge process, the CG1100 and A-CG1100 showed contrasting profiles. The charge capacity of the GG1100 was mostly delivered at 0.01~0.8 V vs. Na whereas the A-CG1100 delivered its capacity of 105 mAh g^{-1} and 70 mAh g^{-1} upon 0.01~0.8 and 0.8~2 V, respectively. Under the assumption that the reversible capacity of CG1100 refers to double layer capacitive charge storage (Route I), the estimated contribution of the route I and II in the A-CG1100 are 56% and 44%, respectively. We postulated '*defective sites*' refer to all what makes graphene's structure being biased from ideal honeycomb-like sp^2-c structure. In this regards, we evaluated the electrochemical performance of the A-CG500 and A-CG800 and compared to A-CG1100 at 0.2 A g^{-1} (**Fig. 6.5c,d)**. The discharge capacity increased from 145 mAh g^{-1} (A-CG1100) to 223 mAh g^{-1} (A-CG500) as the temperature lowered. With the decrease of temperature, the charge capacity also improved from the 139 mAh g^{-1} (A-CG1100) to 220 mAh g^{-1} (A-CG500). This indicates that the more introduction of oxygen-functional groups on the A-CG (**Fig. 6.6**) by lowering reduction temperature improve graphene's charge storage ability. The discharge and charge capacities of the A-CGs at 0.01~0.8 and 0.8~2.5 V vs. Na are shown in **Table 6.2**. The A-CGs possesses relatively similar capacities in 0.01~0.8 V vs. Na whereas they show the sharp increase of capacity at 0.8~2.5 V vs. Na with the lowering of

temperature. The apparent increase of the capacity and the change of charge/discharge profiles with more introduction of oxygen functional group presumably indicates that the oxygen-functional groups are associated with the route II and could be translated into as a certain type of defects and on graphene. The characterizations of the A-CGs (Raman spectroscopy and X-ray diffraction, XRD) are given in **Figure 6.7.**

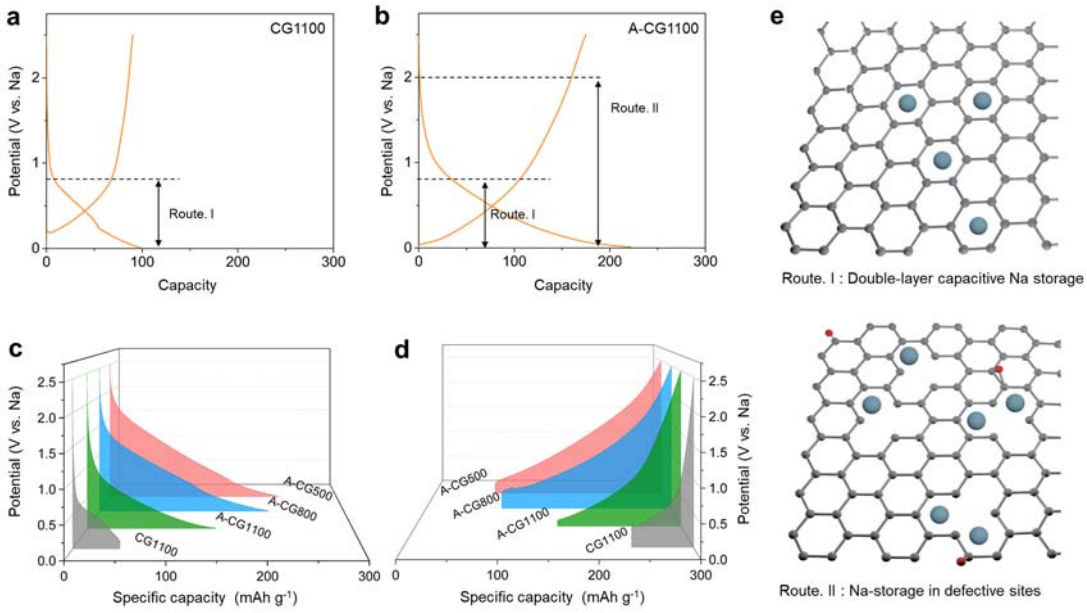

Figure 6.5 Electrochemical characterization of the CG and A-CGs. Galvanostatic charge/discharge profiles of the (a) CG1100 and (b) A-CG1100 at 0.2C. The insets are schematic illustration of Na storage on the CG and A-CG. Galvanostatic (c) discharge and (d) charge profiles of A-CGs. The charge/discharge were performed at 0.2 A g^{-1} in the voltage window of 0.01-2.5 V vs. Na. (e) Schematically illustrated morphologies of adsorbed Na^+ ions on (upper) pristine graphene and (lower) defective graphene.

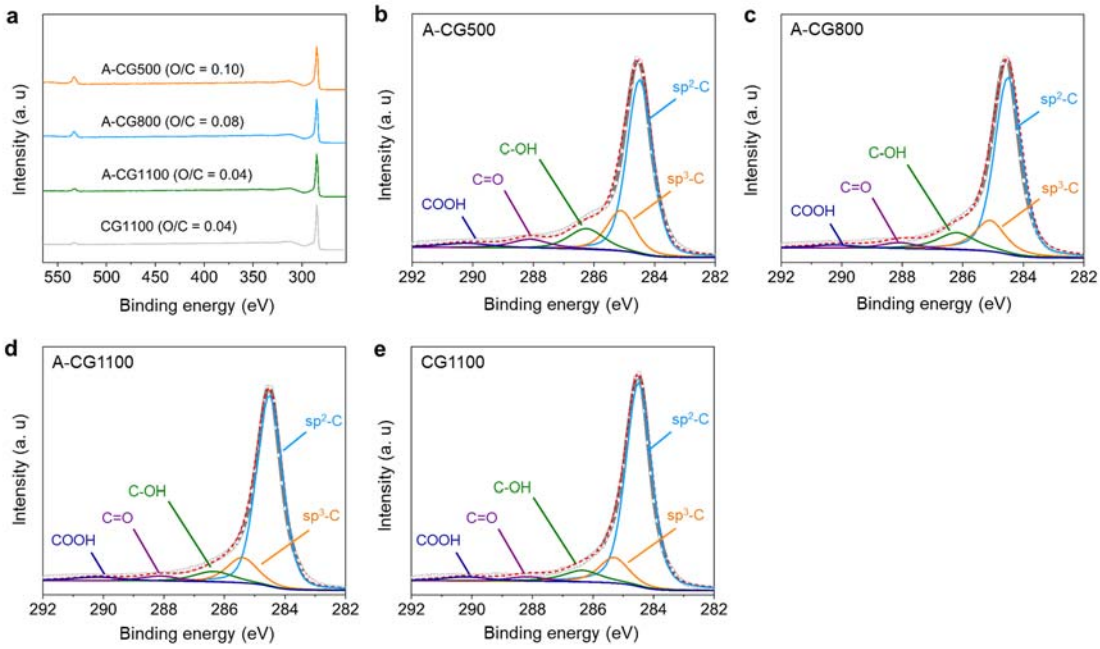

Figure 6.6 Surface chemistry of A-CGs and CG (a) Wide scan surveys. High resolution C1s spectra of (b) CG1100, (c) A-CG1100, (d) A-CG800 and (e) A-CG500. C1s spectra were fitted by 5 peaks for sp^2-C, sp^3-C, C-OH, C=O and COOH. As temperature decreases from 1100 °C to 500 °C, the ratio of oxygen to carbon (O/C ratio) increases from 0.04 to 0.10. The activation has a negligible effect on the O/C ratio as shown in the A-CG1100 and CG1100.

Table 6.2 Discharge and charge capacities of the A-CGs.

	Discharge capacity [mAh g^{-1}]		Charge capacity [mAh g^{-1}]	
	0.8~2.5 V	0.01~0.8 V	0.01~0.8 V	0.8~2.5 V
CG1100	3.7	60.7	40	17.3
A-CG1100	18.6	126.4	87.1	52.3
A-CG800	70	136	96	110
A-CG500	95	128	88	132

The GO showed the sharp peak of the GO at 10.5° which is typically found in highly restacked oxidized GO. [130, 189] The A-CGs and CGO showed no peaks at 10.5°, indicating that GO sheets were not highly restacked and ordered. [47] The A-CGs showed broad and weak peaks at 25.5~26°. These broad peaks can be attributed to due to poor ordering along the stacking directions which usually found in 3D reduced graphene oxide. [2, 150] In Raman spectroscopy analysis, all samples show a broad D-band (~1350 cm^{-1}) and G-band (~1600). With the increase of the reduction temperature, A-CGs showed increased D/G intensity ratios. This can be attributed to a decrease in the average size of the sp2 domains upon reduction of the GO.[134]

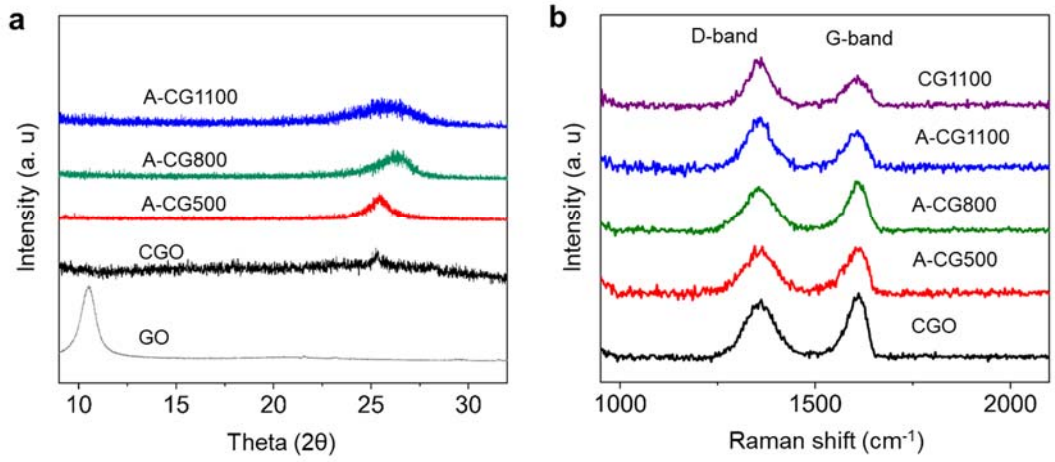

Figure 6.7 (a) X-ray diffraction (XRD) patterns. The XRD pattern of the GO is measured from film which is prepared by vacuum filtration. (b) Raman spectroscopy investigation.

Rate-capability of the A-CG500 is shown in Fig. **6.8a and 6.8b**. The A-CG500 delivered high charge capacities of ~280, ~247 and ~221 mAh g^{-1} at the current density of 0.04, 0.1, 0.2, 0.5, 1 and 2 A g^{-1}, respectively. Even at the high rate of 0.5, 1 and 2 A g^{-1}, the A-CG showed high capacities of ~191, ~172 and ~151 mAh g^{-1}, respectively.

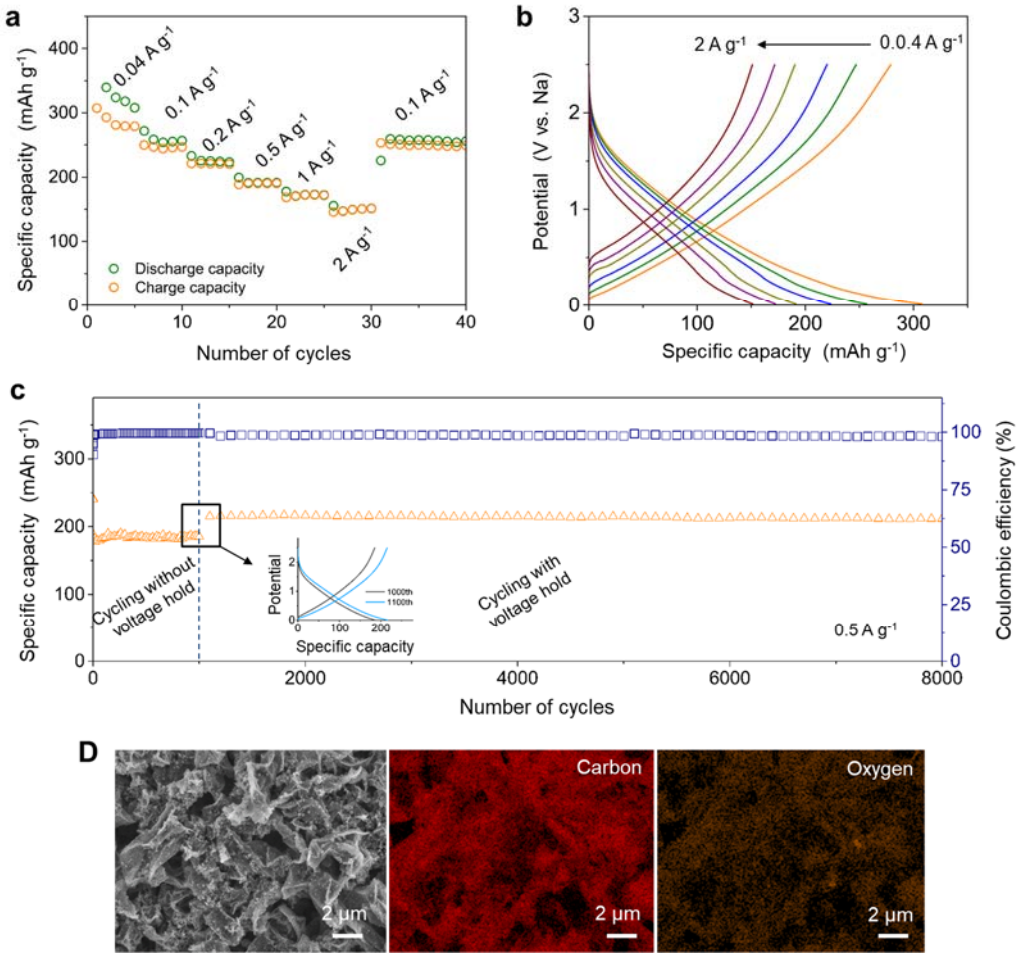

Figure 6.8 Electrochemical performance of the A-CG500. (a) Charge/discharge capacity at the varied current density of 0.04~2 Ag^{-1}. (b) Detailed charge/discharge voltage profiles. (c) Investigation of cycling stability. (Inset, detailed voltage profiles at 1000th and 1100th cycle.) The cycling was were performed at 0.5 A g^{-1} in the voltage window of 0.01-2.5 V vs. Na. (d) SEM-image and elemental mapping of the A-CG500 after the cycling.

When the current density was recovered to 0.5 C, the A-CG500 fully recovered its charge capacity of ~250 mAh g^{-1}. The A-CG500 showed superior rate-performance than the other A-CGs (**Fig. 6.9**). Best on our knowledge, the reversible capacity and rate-capability of the A-CG500 show the highest electrochemical performance among the

previous graphene reports (**Table 6.3**). The superior rate-capability and the high capacity of the A-CG500 can be attributed to capacitive charge storage nature of graphene and the utilization of the capacitive charge storage route II. Galvanostatic intermittent titration technique (GITT) results of the A-CG are in given in **Figure 6.10**. The line with the hollow circle represents the quasi-equilibrium potential. From the quasi-equilibrium potential, the reaction resistance was calculated. During the discharge (sodiation), around 0.6 V, the

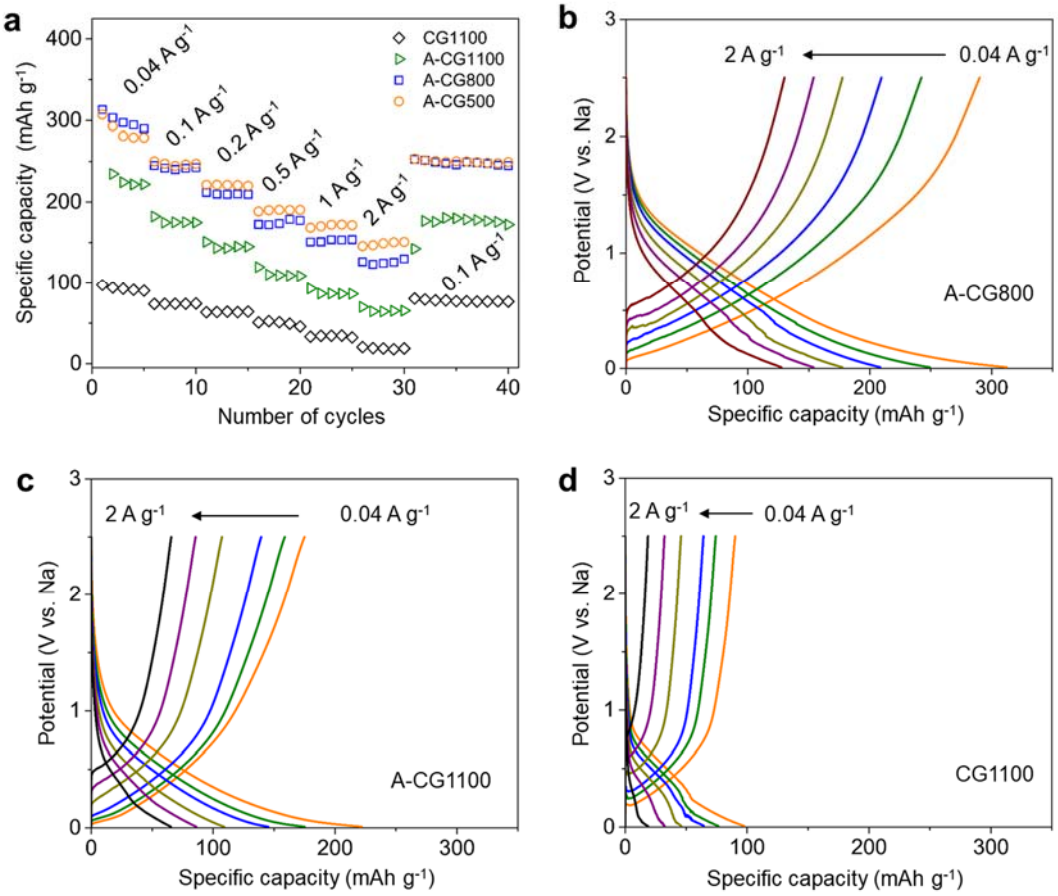

Figure 6.9 Electrochemical performance comparisons of A-CGs. (a) Charge/discharge capacity at the varied current density of 0.04~2 A g^{-1}. Detailed charge/discharge voltage profiles of the (b) A-CG800, (c) A-CG1100 and (d) CG-1100.

Table 6.3 Comparisons of graphene anodes for Na-Ion batteries

Material	Cutoff Voltage (v)	Capacity at high-rate [mAh g^{-1}]	Capacity [mAh g^{-1}] (capacity retention[a], cycle #)	Ref
Expanded Graphite	2.0	91 (0.2A/g)	~150 (<80%, 2000th)	176
Reduced graphene oxide	2.0	96 (1 A/g)	93.3 (<80%, 250th)	89
Reduced graphene oxide	3	<80 (1 A/g)	<100 (-, 300th)	177
Activated carbon/Graphene	2.5	~170 (1 A/g)	142 (83.5%, 2500th)	79
Crumpled graphene paper	2.5	<100 (1 A/g)	~100 (<70%, 500th)	181
Hydrogel derived carbon	3	181 (1.6 A/g)	~150 (79%, 5000th)	188
CNT/GO	3.0	<175 (2 A/g)	~200(<67%, 100th)	190
GO-Carbon	2.0	50 (0.5 A/g)	213(<90%, 200th)	191
Graphene	2.0	146 (1 A/g)	150~160 (80%, 300th)	86
S-doped Graphene paper	3	89 (1 A/g)	244 (<70%, 300th)	192
N-doped carbon/graphene	3	139 (2 A/g)	270 (89%, 200th)	48
Hard carbon with expanded nanographite	2.7	<100 (1 A/g)	113 (<60%, 1000th)	126
Three-dimensional carbon framework	2	~115 (1 A/g)	- (~85%, 250th)	193
Carbon nanofiber	2.0	132 (1 A/g)	134.2(<75%, 200th)	194
Carbon nanosheet	3.0	89 (1 A/g)	155.2(<50%, 260th)	195
Reduced graphene oxide	2.5	60 (1.6 A/g)	105 (<80%, 1000th)	196
Graphene nanosheets	2	~150 (1 A/g)	~150 (75%, 500th)	48
This work	2.5	~172 (1 A/g) ~151 (2 A/g)	~234 (98.3%, 8000th)	

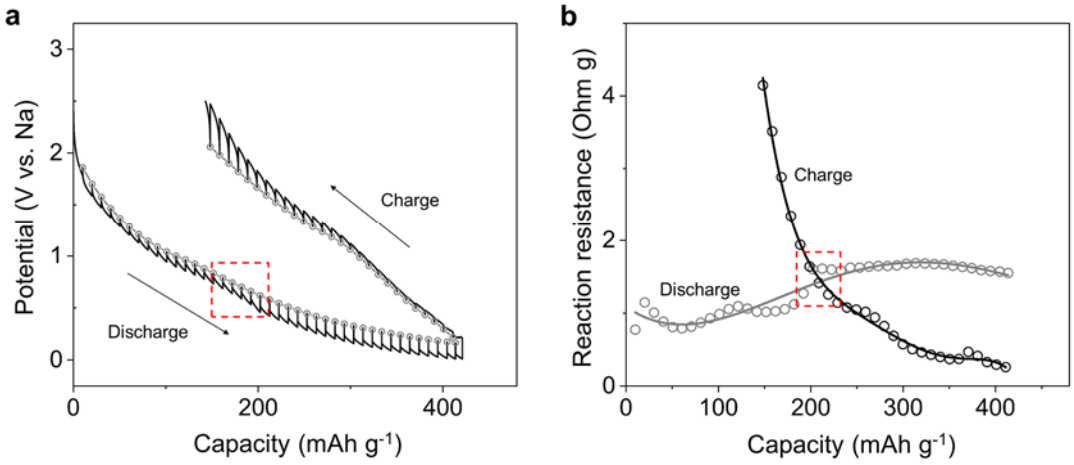

Figure 6.10 Galvanostatic intermittent titration technique (GITT) results of the A-CG500. (a) GITT curves (black line) with quasi-equilibrium potential during charge and discharge. (b) Reaction resistance. The GITT curves were obtained from a series of current pulses of 0.5C for 5 min and 1h relaxation.

quasi-equilibrium potential increases a bit. This might indicate the advent of the different stage of Na storage (such as route I) below this voltage. During the charge process, the reaction resistance gradually increases upon the voltage window of 0.01-2.5 V vs. Na. This can be attributed to the extraction of Na ions from the less favorable sites.

Cycling stability of the A-CG500 is presented in **Figure 6.8c**. The first 10 cycles were performed at 0.1 A g^{-1}. It is known that graphene anodes in batteries have a poor Coulombic efficiency (CE) in the first cycle due to the electrolyte decomposition on the large surface of graphene.[35] Although the A-CG500 showed the fairly substantial capacity loss in the first cycles, CE of the A-CG500 in the first cycle was close to 45% similar to that of the expanded graphite.[9] In the subsequent cycles, the CG-500A was rapidly stabilized with a small fluctuation in capacity (198~205 mAh g^{-1}), showing a good CE over

99%. Even at the 1000th cycle, the A-CG-500A electrodes exhibited capacity retention close to 100% with a high capacity of ~204 mAh g^{-1}. This excellent cycling stability is attributed to the capacitive charge storage mechanism which does not accompany volume change. After resting for 24h, the stability of the A-CG500A electrode was further examined up to 8,000 cycles using the accelerated cycling method.[161] In brief, the A-CG500 was cycled at 5 A g^{-1} for 99 cycles and then, the capacity was measured at 2.5C for 1cycle. At each end of charge and discharge at 0.5 A g^{-1}, the A-CG500 was kept at a constant voltage (0.01 V or 2.5V vs. Na) for 15 min. When CG-500A was operated using the accelerated cycling method, it showed the slightly increased capacity of 215 mAh g^{-1} (Inset in Fig 3C, detailed charge/discharge profiles at 1000th and 1100th cycles). During the cycling measurement, the A-CG showed the negligible capacity drop. Even at the 8000th cycle, capacity retention of the A-CG500 was ~98.3% (211.6 mAh g^{-1}). To further investigate the remarkable cycling stability of the A-CG500, the A-CG500 electrode was investigated by SEM equipped with EDX after the cycling test (**Fig. 6.8d**). After the cycling test, the A-CG500 well maintained crumpled graphene morphology with the uniform elemental (C and O) distribution. Moreover, the A-CG500 still showed a clean surface, indicating very limited side reaction has occurred over the ultra-long cycles.

The capacity increase with the accelerated cycling method presumably indicates that the A-CG500 store an extra charge through the other route. Since the A-CG500 electrode has been kept at 0.01 or 2.5 V vs. Na for 15 min during the accelerated cycling, it could be deduced that the extra Na storage is originated from Na insertion into the disordered long graphitic range at a low voltage. To elucidate the capacity increase and as well as charge storage mechanism of the A-CG, we performed potential-dependent cyclic

voltammetry (PDCV) scans at 0.2 mV s^{-1} at varied voltage window (**Fig. 6.11A**). As the potential window decreased from 2.5 to 0.16 V vs. Na, the quasi triangular CV profile has been developed with broad cathodic/anodic peaks over the potential, presumably indicating the capacitor-like feature of graphene's sodiation/desodiation over the potential. When the cut-off potential was further lowered from 0.16 to 0.01 V vs. Na, the A-CG500 showed a small protruding peak. This sharp peak at the narrow range of potential typically is found in diffusion-controlled materials such as graphite and pseudographitic carbon.[185, 187] Therefore, we can surmise the capacity increase at the accelerated cycling method comes from the Na storage into the pseudographitic carbon area, herein ridge parts, due to the voltage holding. To further understand the Na insertion into the disordered graphitic range, CV scans were performed at the varied scan rate of 0.1~10 mV s^{-1} (**Fig. 6.11B**). At the low scan rates of 0.1 and 0.2 mV s^{-1}, the CV profiles showed a triangular shape with protruding peaks at the low potential of ~0.16 V vs. Na. However, at the high scan rates faster than 0.5 mV s^{-1}, the protruding peaks disappeared. Since intercalation is considered as the diffusion-controlled process, therefore, the disappearance of the peak at the low potential indicates that charge storage on the disordered graphitic area of graphene only occurs when the current density is low. [185, 197]

To explore the nature of the charge storage features, linear relationships of logarithmic scan rates versus logarithmic currents were calculated from eq. (6.1). [197]

$$i = a\nu^b \tag{6.1}$$

where a and b are constants, i is current, and ν is the scan rate. Based on the b value, an electrochemical process can be identified as being diffusion-controlled (b=0.5) or

capacitive (b=1). Here we employed cathodic current values. At the potentials of 0.6 and 1.2 V vs. Na, the b values were found to be 0.97 and 0.99 (**Fig. 6.11C**), showing a signal of capacitive charge storage. As the measured potential decreased, the b values approached to 0.5. **Figure 6.11D** shows the plot of the b value versus potential. The b values are ranged between 0.75~1.0 over the potential and were fallen down around 0.2 V vs. Na, showing the consistency with the result of the potential dependent CV scans. Although the b value is lower than 1, the b value is close to 1 rather than 0.5. Moreover, we should aware of that actual graphene is slightly different from graphene in the dictionary (an isolated single basal plane of graphite) in that actual graphene can contain many types of things make itself being biased from the definition. Thus, we might be able to summarize that i) ideal graphene mainly stores Na through capacitor-like route over the potential and ii) actual graphene stores Na like-as a capacitor, but like-as a mixed type of a battery and capacitor at the low potential. To quantitatively estimate the contribution of the diffusion-controlled and capacitive process, Trassatti analysis (eq. 6.2) were employed.[198]

$$q(v) = q_{capacitive} + cv^{-1/2} \quad (6.2)$$

where q(v) is the total charge (Q), $q_{capacitive}$ is capacitive charge storage, and $cv^{-1/2}$ is associated with semi-infinite diffusion.[198] q(v) presents solely the capacitive charge storage when the scan rate goes to infinity, and the intercept of the extrapolated line obtained by the capacities at low scan rates indicates capacitive charge storage, herein $q_{capacitive}$.[66, 198] **Figure 6.11e** shows the plot of the normalized capacity versus $v^{-1/2}$where the capacity was normalized based on the capacity at 0.1 mV s^{-1}. At the low scan rates, the normalized capacity showed the linearity which is a characteristic of capacitor.[66] The intercept with y-

axis was found to be 0.72. In other words, the capacity of the A-CG500 can be divided into 72% from capacitive mechanism and 28% through diffusion-controlled process.

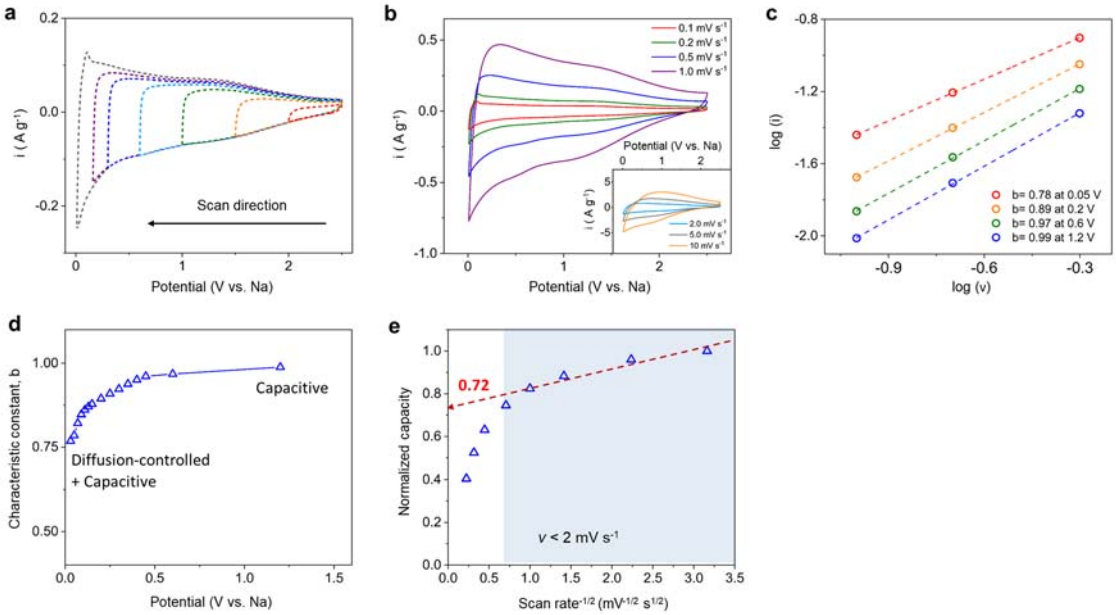

Figure 6.11 Mechanistic analysis of the A-CG500 using cyclic voltammetry (CV) (a) Potential-dependent CV scans at 0.2 mV s^{-1}. (b) CV profiles at different scan rates of 0.1~1 mV s^{-1}. Inset shows CV profiles at high scan rates of 2~10 mV s^{-1}. (c) Linear relationships of logarithmic scan rates versus logarithmic currents at varied potential of 0.05, 0.2, 0.6, 1.2 V vs. Na. (d) Characteristic constant b calculated at varied potential with a scan rate of 0.1 mV s^{-1}. (e) Normalized capacities plot with a function of $v^{-1/2}$.

Inspired by the superior electrochemical properties of the A-CG500 in Na-ion batteries, the A-CG500 was also tested in other alkali-ion batteries, such as Li- and K-ion batteries (LIBs and KIBs) (**Fig. 6.12a**). The A-CG500 delivered high capacities in LIBs and KIBs, showing ~390 and 301 mAh g^{-1} (0.1 A g^{-1}), respectively. These high capacities could be contributed to the charge storage through the route II. The charge/discharge voltage profiles of the A-CG500 in the alkali-ion batteries are shown in **Figure 6.12b**.

Interestingly, the A-CG500 showed relatively low capacity NIBs than in LIBs and KIBs. This can be attributed to the weakest binding to given structures compared to the other alkali ions.[48]

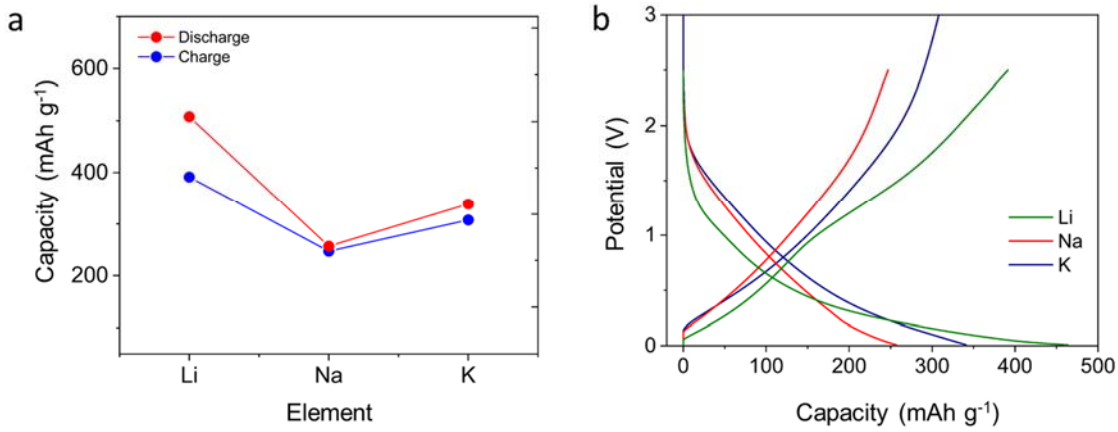

Figure 6.12 (A) Charge/discharge capacity of the defective graphene (A-CG500) with the negative of the binding energy. The binding energy of alkali ions to various defects was redrawn from ref.199 (b) Galvanostatic charge discharge profiles of the defective graphene (A-CG500) in Li-, Na-, and K-cell.

6.5 Conclusions

In this study, we showed that graphene stores Na through the capacitive mechanism with the two sub-routes of ion adsorption in a similar way of double layer capacitance on the surface of graphene and ion adsorption on defective sites. When the defective graphene prepared by air activation was investigated as anode material for SIB, it showed the high capacity of ~250 mAh g^{-1} at 0.5C. In LIB and KIB, the defective graphene also showed the high capacity of ~390 and ~301 mAh g^{-1}, respectively. The high capacity of the defective graphene in various alkali metal ion batteries suggests us that graphene can be identified

as surface-controlled material and thus, the introduction of defective sites is an efficient way to achieve superior electrochemical performance.

CHAPTER 7. CONCLUSION AND OUTLOOK

7.1 General Conclusions

We studied the various applications of graphene in energy storage applications in this dissertation as summarized in **Table 7.1**. In the first part (Chapter 2 and 3), graphene was employed as inactive component for lithium ion batteries. We encapsulated Si particles with the cage of graphene to prevent the electrical isolation of pulverized Si particles. The graphene suppressed the continuous SEI growth on the surface of pulverized Si particles by preventing the pulverized Si particles from exposure to electrolyte. This graphene-encapsulated Si composite showed a capacity retention of 84% at 100th cycle. This graphene-encapsulated Si composite was employed as anode for hybrid supercapacitor in Chapter 3. We prepared a two-dimensional functional carbon by hydrothermal carbonization of glucose with GO template. The two-dimensional functional carbon showed a high capacity of ~250 mAh g^{-1} in a Li-cell, which is higher than carbon sphere prepared without GO template (~153 mAh g^{-1}). Even with the mass-loading of ~9.3 mg cm^{-2}, the two-dimensional functional carbon exhibited the high capacity of ~243 mAh g^{-1}. The hybrid supercapacitor, the two-dimensional functional carbon and graphene-encapsulated Si anode showed a high capacity close to 150 mAh g^{-1} upto 3,000 cycles.

In the second part (Chapter 3-5), this thesis focused on the electrochemical performance and charge storage mechanisms of graphene in LIBs, SIB and supercapacitors.

As a cathode material for LIBs, we prepared the reduced crumpled graphene oxide and cabbage-like graphene using aerosol pyrolysis. Compared to stacked reduced graphene, the reduced crumpled graphene oxide showed enhanced rate-capability. The cabbage-like graphene exhibited the high specific capacity of ~176 mAh g^{-1} despite its high density of ~0.8 g cm^{-3}. In addition, crumpled graphene was employed as anode material for SIBs. To investigate the role of oxygen functional groups, including defects, we prepared crumpled graphene at various reduction temperature with/without air activation process. From the electrochemical and computational study of the crumpled graphene, we revealed that graphene stores Na through double layer capacitance and ion adsorption on defective sites. The activated crumpled graphene as a model of defective graphene showed the high capacity (~ 279 mAh g^{-1} at 0.2C) and rate-capability (151 mAh g^{-1} at 10C), indicating the utility of the defective sites to enhance electrochemical performance of graphene for Na-ion storage.

Table 7.1 Summaries of graphene as inactive component and active material in energy storage applications.

Inactive	Graphene composite with submicron Si (Si/graphene)	➢ Application: Physical/chemical protection layers for large volume change materials. ➢ The severely pulverized Si particles well confined in the graphene layers during cycling.	
	Two-dimensional biomass-derived functional carbon (TDFC)	➢ Application: Template to deposit biomass-derived carbon ➢ Shape of biomass-derived carbon (BDC) was controlled by GO templates. ➢ The shape-controlled BDC showed a high capacity in LI- and Na- cells.	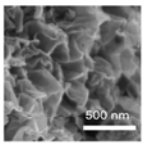
Active	Reduced crumpled graphene oxide (r-CGO)	➢ Application: Cathode for LIBs ➢ Reduced crumpled graphene oxide showed enhanced rate-capability compared to stacked reduced graphene oxide due	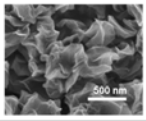
	Graphene cabbage (GR cabbage)	➢ Application: Cathode for LIBs and electrodes for supercapacitors ➢ Graphene cabbage (~0.8 g/cm^3) was prepared by two step process of pre-reduction and aerosol spray drying. ➢ Size of graphene cabbage was controllable using different concentrations of GO and urea	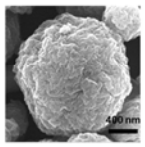
	Activated crumpled graphene (CG)	➢ Application: Anode for SIBs ➢ Activated crumpled graphene can store sodium ions. ➢ High capacity up to ~250 mAh/g and long life cycle up to 8, 000 cycles.	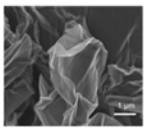

7.2 Perspective

We showed a wide potential of graphene in energy storage systems in this thesis. This thesis consists of two parts; graphene as an inactive component and graphene as an active material. In the study of graphene as the inactive component, we showed that graphene can be employed as a template to control the morphology of hydrocarbon obtained from hydrothermal carbonization of biomass (e.g., glucose and sucrose). Although the two-dimensional functional carbon prepared by hydrothermal carbonization of biomass with a small addition of graphene template showed excellent electrochemical performance (e.g., ~250 mAh g^{-1} in a Li-cell), it requires further studies to reveal chemical structure of the TDFC. For instance, we should answer the question, “Is biomass-derived carbon deposited on graphene or graphene oxide?” During the hydrothermal carbonization

of biomass, graphene oxide can be hydrothermally reduced. Moreover, the core motivation of the TDFC was started from the shell-core structure of bio-mass derived carbon (**Fig 7.1**).

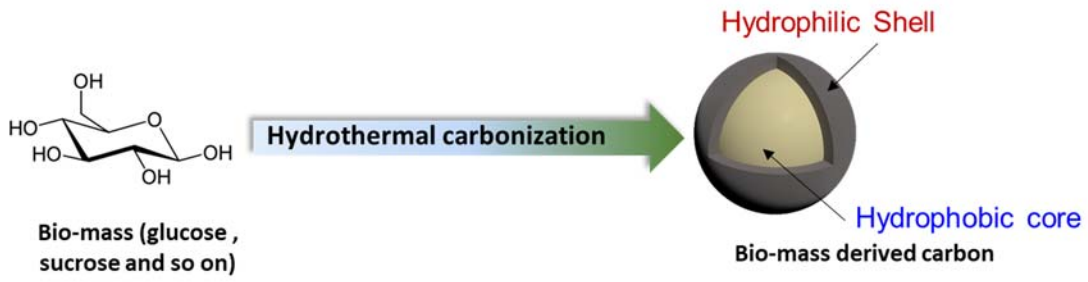

Figure 7.1 Schematic illustration of bio-mass derived carbon.

Bio-mass derived carbon has a hydrophobic core and hydrophilic shell structure. The hydrophilic shell contains a large amount of redox active oxygen functional groups.[200] Since the charge storage mechanism of hydrocarbon is based on double layer capacitance and redox-reactions of the surface functional groups, the hydrophobic core part may not contribute to charge storage. Considering the fact that TDFC (one side thickness: ~10 nm) shows a higher electrochemical performance that carbon sphere (~200nm), the thickness of hydrophilic shell would be very thin (i.e., less than 10 nm). In this regard, it is needed to investigate the electrochemical performance of oxygen-functional group-rich quantum dot which is prepared from biomass and their carbonization.

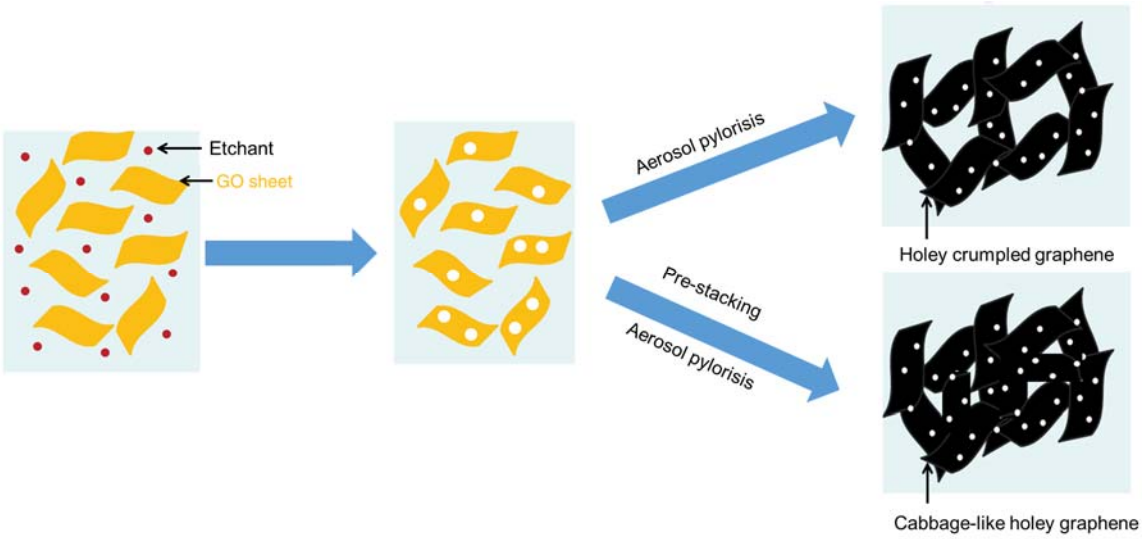

Figure 7.2 Schematic preparation of cabbage-like holey graphene. Reproduced with the permission from Ref#201 Copyright ©2014 Springer Nature.

In the study of graphene as an active material, graphene was investigated as cathode material in Li-cell and, anode material in Li-, Na- and K-cell. As the cathode material, the reduced crumpled graphene oxide was used, and it showed a good rate-capability (~170 mAh g^{-1} at 0.1 A g^{-1} and ~65 mAh g^{-1} at 10 A g^{-1}) as shown in Chapter 4. The high capacity and good rate-capability were attributed to the oxygen functional groups on its surface, such as carbonyl, carboxylic and epoxide while the hydroxyl (-OH) group on the surface of the reduced crumpled graphene oxide only delivers limited capacity.[122] Therefore, it is needed to develop hydroxyl-selective reduction method. The reduced crumpled graphene oxide was investigated in the high potential of 1.5-4.5 V vs. Li. In this potential, conventional carbonate-based electrolytes can be decomposed. Thus, byproducts or their intermediate forms may have an influence on functional groups. In this regard, *in-situ* FTIR and XPS could be utilized to the influence.

To date, various three-dimensional graphene electrodes for supercapacitor have been proposed.[202-203] Regrettably, in most cases, gravimetric capacitance (or capacity) has been focused rather than volumetric density. To grasp high gravimetric and volumetric capacitance with an electrode, we introduced pre-stacking process for graphene (Chapter 5) and prepared a high-density cabbage-like graphene. However, it is unlikely to show that the cabbage-like graphene has a high capacitance or capacity at 10 A g^{-1} or 100 mV s^{-1} due to the large stacking. We believe that enhanced rate-capability can be achieved by employing holey graphene oxide as the precursor. The lowered density coming from the introduction of holes on the graphene oxide sheet could be compensated by increasing the concentration of holey graphene oxide and pre-stacking time (**Fig. 7.2**). The holes on the graphene sheet could facilitate the transport of ions and thus rate-capability of cabbage-like could be further enhanced.

Except for the study of hybrid supercapacitor consisting of Si/graphene anode and TDFC cathode, all the other electrodes were evaluated with negative electrodes of lithium or sodium metal piece. However, the performance of electrodes should be investigated full-cell configuration for practical application. For instance, the reduced crumpled graphene oxide and cabbage-like graphene would be coupled with graphite or Si anode. Recently, there has been noticeable progress in metal anode.[204-213] Thus, advanced metal anode would be also a choice for those cathodes.

In the study of graphene cathode for LIBs, we mainly focused on the oxygen functional groups of graphene and only used thermal reduction to control the amount of the oxygen functional groups. Chemical reduction using $NaBH_4$ and thiourea is also well-the established technique. Using these chemicals and subsequent thermal reduction,

heteroatom (B, N and S)-doped graphene can be prepared. It is known that the heteroatom doping is a promising strategy to enhance graphene-based electrodes. Although this dissertation focuses on the application of graphene in LIBs, SIBs and supercapacitors, graphene can be employed as a catalytic cathode in lithium- and sodium-air battery (Fig. 7.3) and as artificial solid electrolyte interface for room temperature metal battery.[214]

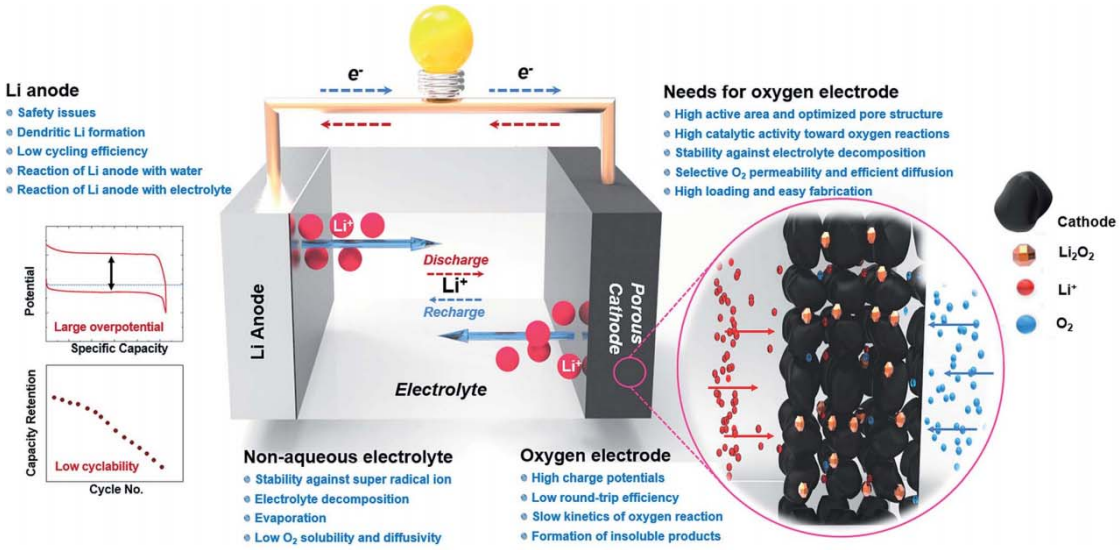

Figure 7.3 Schematic illustration of lithium-air battery. Reprinted with permission from Ref#215 Copyright © 2016 Royal Society of Chemistry.

REFERENCES

1. Goodenough, J. B.; Park, K. S., The Li-Ion Rechargeable Battery: A Perspective. *J Am Chem Soc* **2013,** *135* (4), 1167-1176.
2. Lee, B.; Lee, C.; Liu, T. Y.; Eom, K.; Chen, Z. M.; Noda, S.; Fuller, T. F.; Jang, H. D.; Lee, S. W., Hierarchical networks of redox-active reduced crumpled graphene oxide and functionalized few-walled carbon nanotubes for rapid electrochemical energy storage. *Nanoscale* **2016,** *8* (24), 12330-12338.

3. Xia, X. H.; Chao, D. L.; Fan, Z. X.; Guan, C.; Cao, X. H.; Zhang, H.; Fan, H. J., A New Type of Porous Graphite Foams and Their Integrated Composites with Oxide/Polymer Core/Shell Nanowires for Supercapacitors: Structural Design, Fabrication, and Full Supercapacitor Demonstrations. *Nano Lett* **2014,** *14* (3), 1651-1658.
4. Zhang, L. L.; Zhao, X. S., Carbon-based materials as supercapacitor electrodes. *Chem Soc Rev* **2009,** *38* (9), 2520-2531.
5. Simon, P.; Gogotsi, Y., Materials for electrochemical capacitors. *Nat Mater* **2008,** *7* (11), 845-854.
6. Simon, P.; Gogotsi, Y.; Dunn, B., Where Do Batteries End and Supercapacitors Begin? *Science* **2014,** *343* (6176), 1210-1211.
7. Wang, H. W.; Zhang, Y.; Ang, H. X.; Zhang, Y. Q.; Tan, H. T.; Zhang, Y. F.; Guo, Y. Y.; Franklin, J. B.; Wu, X. L.; Srinivasan, M.; Fan, H. J.; Yan, Q. Y., A High-Energy Lithium-Ion Capacitor by Integration of a 3D Interconnected Titanium Carbide Nanoparticle Chain Anode with a Pyridine-Derived Porous Nitrogen-Doped Carbon Cathode. *Adv Funct Mater* **2016,** *26* (18), 3082-3093.
8. Cho, J.; Kim, Y. J.; Park, B., Novel LiCoO2 cathode material with Al2O3 coating for a Li ion cell. *Chem Mater* **2000,** *12* (12), 3788-3791.
9. Zhao, H. L.; Ling, G.; Qiu, W. H.; Zhang, X. H., Improvement of electrochemical stability of LiCoO2 cathode by a nano-crystalline coating. *J Power Sources* **2004,** *132* (1-2), 195-200.
10. Frisco, S.; Kumar, A.; Whitacre, J. F.; Litster, S., Understanding Li-Ion Battery Anode Degradation and Pore Morphological Changes through Nano-Resolution X-ray Computed Tomography. *J Electrochem Soc* **2016,** *163* (13), A2636-A2640.
11. Luo, J. S.; Liu, J. L.; Zeng, Z. Y.; Ng, C. F.; Ma, L. J.; Zhang, H.; Lin, J. Y.; Shen, Z. X.; Fan, H. J., Three-Dimensional Graphene Foam Supported Fe3O4 Lithium Battery Anodes with Long Cycle Life and High Rate Capability. *Nano Lett* **2013,** *13* (12), 6136-6143.
12. Zhou, Y. P.; Rui, X. H.; Sun, W. P.; Xu, Z. C.; Zhou, Y.; Ng, W. J.; Yan, Q. Y.; Fong, E., Biochemistry-Enabled 3D Foams for Ultrafast Battery Cathodes. *Acs Nano* **2015,** *9* (4), 4628-4635.

13. Jost, K.; Dion, G.; Gogotsi, Y., Textile energy storage in perspective. *J Mater Chem A* **2014,** *2* (28), 10776-10787.
14. Wang, G. P.; Zhang, L.; Zhang, J. J., A review of electrode materials for electrochemical supercapacitors. *Chem Soc Rev* **2012,** *41* (2), 797-828.
15. Ma, Y. F.; Chang, H. C.; Zhang, M.; Chen, Y. S., Graphene-Based Materials for Lithium-Ion Hybrid Supercapacitors. *Adv Mater* **2015,** *27* (36), 5296-5308.
16. Aravindan, V.; Gnanaraj, J.; Lee, Y. S.; Madhavi, S., Insertion-Type Electrodes for Nonaqueous Li-Ion Capacitors. *Chem Rev* **2014,** *114* (23), 11619-11635.
17. Li, H. S.; Peng, L. L.; Zhu, Y.; Zhang, X. G.; Yu, G. H., Achieving High-Energy-High-Power Density in a Flexible Quasi-Solid-State Sodium Ion Capacitor. *Nano Lett* **2016,** *16* (9), 5938-5943.
18. Naoi, K.; Ishimoto, S.; Miyamoto, J.; Naoi, W., Second generation 'nanohybrid supercapacitor': Evolution of capacitive energy storage devices. *Energ Environ Sci* **2012,** *5* (11), 9363-9373.
19. Raccichini, R.; Varzi, A.; Passerini, S.; Scrosati, B., The role of graphene for electrochemical energy storage. *Nat Mater* **2015,** *14* (3), 271-279.
20. Novoselov, K. S.; Geim, A. K.; Morozov, S. V.; Jiang, D.; Zhang, Y.; Dubonos, S. V.; Grigorieva, I. V.; Firsov, A. A., Electric field effect in atomically thin carbon films. *Science* **2004,** *306* (5696), 666-669.
21. Schwierz, F., Graphene transistors. *Nat Nanotechnol* **2010,** *5* (7), 487-496.
22. Huang, X.; Qi, X. Y.; Boey, F.; Zhang, H., Graphene-based composites. *Chem Soc Rev* **2012,** *41* (2), 666-686.
23. Novoselov, K. S.; Fal'ko, V. I.; Colombo, L.; Gellert, P. R.; Schwab, M. G.; Kim, K., A roadmap for graphene. *Nature* **2012,** *490* (7419), 192-200.
24. Wu, Z. S.; Zhou, G. M.; Yin, L. C.; Ren, W.; Li, F.; Cheng, H. M., Graphene/metal oxide composite electrode materials for energy storage. *Nano Energy* **2012,** *1* (1), 07-131.
25. Edwards, R. S.; Coleman, K. S., Graphene synthesis: relationship to applications. *Nanoscale* **2013,** *5* (1), 38-51.

26. Su, C. Y.; Lu, A. Y.; Xu, Y. P.; Chen, F. R.; Khlobystov, A. N.; Li, L. J., High-Quality Thin Graphene Films from Fast Electrochemical Exfoliation. *Acs Nano* **2011,** *5* (3), 2332-2339.
27. Wang, J. Z.; Manga, K. K.; Bao, Q. L.; Loh, K. P., High-Yield Synthesis of Few-Layer Graphene Flakes through Electrochemical Expansion of Graphite in Propylene Carbonate Electrolyte. *J Am Chem Soc* **2011,** *133* (23), 8888-8891.
28. Huang, H.; Xia, Y.; Tao, X. Y.; Du, J.; Fang, J. W.; Gan, Y. P.; Zhang, W. K., Highly efficient electrolytic exfoliation of graphite into graphene sheets based on Li ions intercalation-expansion-microexplosion mechanism. *J Mater Chem* **2012,** *22* (21), 10452-10456.
29. Blake, P.; Brimicombe, P. D.; Nair, R. R.; Booth, T. J.; Jiang, D.; Schedin, F.; Ponomarenko, L. A.; Morozov, S. V.; Gleeson, H. F.; Hill, E. W.; Geim, A. K.; Novoselov, K. S., Graphene-based liquid crystal device. *Nano Lett* **2008,** *8* (6), 1704-1708.
30. Wang, G. X.; Wang, B.; Park, J.; Wang, Y.; Sun, B.; Yao, J., Highly efficient and large-scale synthesis of graphene by electrolytic exfoliation. *Carbon* **2009,** *47* (14), 3242-3246.
31. Englert, J. M.; Rohrl, J.; Schmidt, C. D.; Graupner, R.; Hundhausen, M.; Hauke, F.; Hirsch, A., Soluble Graphene: Generation of Aqueous Graphene Solutions Aided by a Perylenebisimide-Based Bolaamphiphile. *Adv Mater* **2009,** *21* (42), 4.
32. Luo, J. Y.; Jang, H. D.; Sun, T.; Xiao, L.; He, Z.; Katsoulidis, A. P.; Kanatzidis, M. G.; Gibson, J. M.; Huang, J. X., Compression and Aggregation-Resistant Particles of Crumpled Soft Sheets. *Acs Nano* **2011,** *5* (11), 8943-8949.
33. Shams, S. S.; Zhang, R. Y.; Zhu, J., Graphene synthesis: a Review. *Mater Sci-Poland* **2015,** *33* (3), 566-578.
34. Lin, Y. M.; Dimitrakopoulos, C.; Jenkins, K. A.; Farmer, D. B.; Chiu, H. Y.; Grill, A.; Avouris, P., 100-GHz Transistors from Wafer-Scale Epitaxial Graphene. *Science* **2010,** *327* (5966), 662-662.
35. Hassoun, J.; Bonaccorso, F.; Agostini, M.; Angelucci, M.; Betti, M. G.; Cingolani, R.; Gemmi, M.; Mariani, C.; Panero, S.; Pellegrini, V.; Scrosati, B., An Advanced

Lithium-Ion Battery Based on a Graphene Anode and a Lithium Iron Phosphate Cathode. *Nano Lett* **2014,** *14* (8), 4901-4906.

36. Vargas, O. A.; Caballero, A.; Morales, J., Can the performance of graphene nanosheets for lithium storage in Li-ion batteries be predicted? *Nanoscale* **2012,** *4* (6), 2083-2092.
37. Wang, Y. X.; Chou, S. L.; Liu, H. K.; Dou, S. X., Reduced graphene oxide with superior cycling stability and rate capability for sodium storage. *Carbon* **2013,** *57*, 202-208.
38. Wen, Y.; He, K.; Zhu, Y. J.; Han, F. D.; Xu, Y. H.; Matsuda, I.; Ishii, Y.; Cumings, J.; Wang, C. S., Expanded graphite as superior anode for sodium-ion batteries. *Nat Commun* **2014,** *5*.
39. Ivanovskii, A. L., Graphene-based and graphene-like materials. *Russ Chem Rev+* **2012,** *81* (7), 571-605.
40. Wang, Z. L.; Xu, D.; Xu, J. J.; Zhang, L. L.; Zhang, X. B., Graphene Oxide Gel-Derived, Free-Standing, Hierarchically Porous Carbon for High-Capacity and High-Rate Rechargeable Li-O2 Batteries. *Adv Funct Mater* **2012,** *22* (17), 3699-3705.
41. Sun, Y. Q.; Wu, Q. O.; Xu, Y. X.; Bai, H.; Li, C.; Shi, G. Q., Highly conductive and flexible mesoporous graphitic films prepared by graphitizing the composites of graphene oxide and nanodiamond. *J Mater Chem* **2011,** *21* (20), 7154-7160.
42. Qiu, L.; Yang, X. W.; Gou, X. L.; Yang, W. R.; Ma, Z. F.; Wallace, G. G.; Li, D., Dispersing Carbon Nanotubes with Graphene Oxide in Water and Synergistic Effects between Graphene Derivatives. *Chemistry-a European Journal* **2010,** *16* (35), 10653-10658.
43. Xu, Y. X.; Sheng, K. X.; Li, C.; Shi, G. Q., Self-Assembled Graphene Hydrogel via a One-Step Hydrothermal Process. *Acs Nano* **2010,** *4* (7), 4324-4330.
44. Jiang, L. L.; Fan, Z. J., Design of advanced porous graphene materials: from graphene nanomesh to 3D architectures. *Nanoscale* **2014,** *6* (4), 1922-1945.
45. Yoon, Y.; Lee, K.; Kwon, S.; Seo, S.; Yoo, H.; Kim, S.; Shin, Y.; Park, Y.; Kim, D.; Choi, J. Y.; Lee, H., Vertical Alignments of Graphene Sheets Spatially and

Densely Piled for Fast Ion Diffusion in Compact Supercapacitors. *Acs Nano* **2014,** *8* (5), 4580-4590.

46. Zhu, Y. W.; Murali, S.; Stoller, M. D.; Ganesh, K. J.; Cai, W. W.; Ferreira, P. J.; Pirkle, A.; Wallace, R. M.; Cychosz, K. A.; Thommes, M.; Su, D.; Stach, E. A.; Ruoff, R. S., Carbon-Based Supercapacitors Produced by Activation of Graphene. *Science* **2011,** *332* (6037), 1537-1541.
47. Wang, H. L.; Yang, Y.; Liang, Y. Y.; Robinson, J. T.; Li, Y. G.; Jackson, A.; Cui, Y.; Dai, H. J., Graphene-Wrapped Sulfur Particles as a Rechargeable Lithium-Sulfur Battery Cathode Material with High Capacity and Cycling Stability. *Nano Lett* **2011,** *11* (7), 2644-2647.
48. Li, Y. Z.; Yan, K.; Lee, H. W.; Lu, Z. D.; Liu, N.; Cui, Y., Growth of conformal graphene cages on micrometre-sized silicon particles as stable battery anodes. *Nat Energy* **2016,** *1*.
49. Kim, W.; Ryu, W.; Han, D.; Lim, S.; Eom, J.; Kwon, H., Fabrication of Graphene Embedded LiFePO4 Using a Catalyst Assisted Self Assembly Method as a Cathode Material for High Power Lithium-Ion Batteries. *Acs Appl Mater Inter* **2014,** *6* (7), 4731-4736.
50. Ding, Y. H.; Ren, H. M.; Huang, Y. Y.; Chang, F. H.; Zhang, P., Three-dimensional graphene/LiFePO4 nanostructures as cathode materials for flexible lithium-ion batteries. *Mater Res Bull* **2013,** *48* (10), 3713-3716.
51. Sun, J.; Lee, H. W.; Pasta, M.; Yuan, H. T.; Zheng, G. Y.; Sun, Y. M.; Li, Y. Z.; Cui, Y., A phosphorene-graphene hybrid material as a high-capacity anode for sodium-ion batteries. *Nat Nanotechnol* **2015,** *10* (11), 980-U184.
52. Zhu, J. X.; Yang, D.; Yin, Z. Y.; Yan, Q. Y.; Zhang, H., Graphene and Graphene-Based Materials for Energy Storage Applications. *Small* **2014,** *10* (17), 3480-3498.
53. Kim, H.; Lim, H. D.; Kim, J.; Kang, K., Graphene for advanced Li/S and Li/air batteries. *J Mater Chem A* **2014,** *2* (1), 33-47.
54. Wang, C.; Wang, X. S.; Yang, Y.; Kushima, A.; Chen, J. T.; Huang, Y. H.; Li, J., Slurryless Li2S/Reduced Graphene Oxide Cathode Paper for High-Performance Lithium Sulfur Battery. *Nano Lett* **2015,** *15* (3), 1796-1802.

55. Wu, H.; Chan, G.; Choi, J. W.; Ryu, I.; Yao, Y.; McDowell, M. T.; Lee, S. W.; Jackson, A.; Yang, Y.; Hu, L. B.; Cui, Y., Stable cycling of double-walled silicon nanotube battery anodes through solid-electrolyte interphase control. *Nat Nanotechnol* **2012,** *7* (5), 309-314.

56. Gomez-Camer, J. L.; Bunzli, C.; Hantel, M. M.; Poux, T.; Novak, P., On the correlation between electrode expansion and cycling stability of graphite/Si electrodes for Li-ion batteries. *Carbon* **2016,** *105*, 42-51.

57. Chen, L. F.; Zhang, X. D.; Liang, H. W.; Kong, M. G.; Guan, Q. F.; Chen, P.; Wu, Z. Y.; Yu, S. H., Synthesis of Nitrogen-Doped Porous Carbon Nanofibers as an Efficient Electrode Material for Supercapacitors. *Acs Nano* **2012,** *6* (8), 7092-7102.

58. Wu, H.; Cui, Y., Designing nanostructured Si anodes for high energy lithium ion batteries. *Nano Today* **2012,** *7* (5), 414-429.

59. Liu, N.; Wu, H.; McDowell, M. T.; Yao, Y.; Wang, C. M.; Cui, Y., A Yolk-Shell Design for Stabilized and Scalable Li-Ion Battery Alloy Anodes. *Nano Lett* **2012,** *12* (6), 3315-3321.

60. Feng, K.; Ahn, W.; Lui, G.; Park, H. W.; Kashkooli, A. G.; Jiang, G. P.; Wang, X. L.; Xiao, X. C.; Chen, Z. W., Implementing an in-situ carbon network in Si/reduced graphene oxide for high performace lithium-ion battery anodes. *Nano Energy* **2016,** *19*, 187-197.

61. Liu, N.; Lu, Z. D.; Zhao, J.; McDowell, M. T.; Lee, H. W.; Zhao, W. T.; Cui, Y., A pomegranate-inspired nanoscale design for large-volume-change lithium battery anodes. *Nat Nanotechnol* **2014,** *9* (3), 187-192.

62. Liu, X. H.; Zhong, L.; Huang, S.; Mao, S. X.; Zhu, T.; Huang, J. Y., Size-Dependent Fracture of Silicon Nanoparticles During Lithiation. *Acs Nano* **2012,** *6* (2), 1522-1531.

63. Kim, H.; Seo, M.; Park, M. H.; Cho, J., A Critical Size of Silicon Nano-Anodes for Lithium Rechargeable Batteries. *Angew Chem Int Ed* **2010,** *49* (12), 2146-2149.

64. Xiao, X. C.; Zhou, W. D.; Kim, Y. N.; Ryu, I.; Gu, M.; Wang, C. M.; Liu, G.; Liu, Z. Y.; Gao, H. J., Regulated Breathing Effect of Silicon Negative Electrode for Dramatically Enhanced Performance of Li-Ion Battery. *Adv Funct Mater* **2015,** *25* (9), 1426-1433.

65. Park, Y.; Choi, N. S.; Park, S.; Woo, S. H.; Sim, S.; Jang, B. Y.; Oh, S. M.; Park, S.; Cho, J.; Lee, K. T., Si-Encapsulating Hollow Carbon Electrodes via Electroless Etching for Lithium-Ion Batteries. *Adv Energy Mater* **2013,** *3* (2), 206-212.
66. Yao, Y.; McDowell, M. T.; Ryu, I.; Wu, H.; Liu, N. A.; Hu, L. B.; Nix, W. D.; Cui, Y., Interconnected Silicon Hollow Nanospheres for Lithium-Ion Battery Anodes with Long Cycle Life. *Nano Lett* **2011,** *11* (7), 2949-2954.
67. Yu, Y.; Gu, L.; Zhu, C. B.; Tsukimoto, S.; van Aken, P. A.; Maier, J., Reversible Storage of Lithium in Silver-Coated Three-Dimensional Macroporous Silicon. *Adv Mater* **2010,** *22* (20).
68. Lee, J. I.; Lee, K. T.; Cho, J.; Kim, J.; Choi, N. S.; Park, S., Chemical-Assisted Thermal Disproportionation of Porous Silicon Monoxide into Silicon-Based Multicomponent Systems. *Angew Chem Int Ed* **2012,** *51* (11), 2767-2771.
69. Chan, C. K.; Peng, H. L.; Liu, G.; McIlwrath, K.; Zhang, X. F.; Huggins, R. A.; Cui, Y., High-performance lithium battery anodes using silicon nanowires. *Nat Nanotechnol* **2008,** *3* (1), 31-35.
70. Cui, L. F.; Ruffo, R.; Chan, C. K.; Peng, H. L.; Cui, Y., Crystalline-Amorphous Core-Shell Silicon Nanowires for High Capacity and High Current Battery Electrodes. *Nano Lett* **2009,** *9* (1), 491-495.
71. Ng, S. H.; Wang, J. Z.; Wexler, D.; Konstantinov, K.; Guo, Z. P.; Liu, H. K., Highly reversible lithium storage in spheroidal carbon-coated silicon nanocomposites as anodes for lithium-ion batteries. *Angew Chem Int Ed* **2006,** *45* (41), 6896-6899.
72. Hu, Y. S.; Demir-Cakan, R.; Titirici, M. M.; Muller, J. O.; Schlogl, R.; Antonietti, M.; Maier, J., Superior storage performance of a Si@SiOx/C nanocomposite as anode material for lithium-ion batteries. *Angew Chem Int Ed* **2008,** *47* (9), 1645-1649.
73. Ko, M.; Chae, S.; Jeong, S.; Oh, P.; Cho, J., Elastic a-Silicon Nanoparticle Backboned Graphene Hybrid as a Self-Compacting Anode for High-Rate Lithium Ion Batteries. *Acs Nano* **2014,** *8* (8), 8591-8599.
74. Zhou, X. S.; Yin, Y. X.; Wan, L. J.; Guo, Y. G., Self-Assembled Nanocomposite of Silicon Nanoparticles Encapsulated in Graphene through Electrostatic Attraction for Lithium-Ion Batteries. *Adv Energy Mater* **2012,** *2* (9), 1086-1090.

75. Luo, J. Y.; Zhao, X.; Wu, J. S.; Jang, H. D.; Kung, H. H.; Huang, J. X., Crumpled Graphene-Encapsulated Si Nanoparticles for Lithium Ion Battery Anodes. *J Phys Chem Lett* **2012,** *3* (13), 1824-1829.

76. Tang, H.; Zhang, J.; Zhang, Y. J.; Xiong, Q. Q.; Tong, Y. Y.; Li, Y.; Wang, X. L.; Gu, C. D.; Tu, J. P., Porous reduced graphene oxide sheet wrapped silicon composite fabricated by steam etching for lithium-ion battery application. *J Power Sources* **2015,** *286*, 431-437.

77. Li, B.; Yang, S. B.; Li, S. M.; Wang, B.; Liu, J. H., From Commercial Sponge Toward 3D Graphene-Silicon Networks for Superior Lithium Storage. *Adv Energy Mater* **2015,** *5* (15).

78. Xu, Z. L.; Zhang, B.; Kim, J. K., Electrospun carbon nanofiber anodes containing monodispersed Si nanoparticles and graphene oxide with exceptional high rate capacities. *Nano Energy* **2014,** *6*, 27-35.

79. Bao, Q.; Huang, Y. H.; Lan, C. K.; Chen, B. H.; Duh, J. G., Scalable Upcycling Silicon from Waste Slicing Sludge for High-performance Lithium-ion Battery Anodes. *Electrochim Acta* **2015,** *173*, 82-90.

80. Lu, Z. D.; Liu, N.; Lee, H. W.; Zhao, J.; Li, W. Y.; Li, Y. Z.; Cui, Y., Nonfilling Carbon Coating of Porous Silicon Micrometer-Sized Particles for High-Performance Lithium Battery Anodes. *Acs Nano* **2015,** *9* (3), 2540-2547.

81. Magasinski, A.; Dixon, P.; Hertzberg, B.; Kvit, A.; Ayala, J.; Yushin, G., High-performance lithium-ion anodes using a hierarchical bottom-up approach. *Nat Mater* **2010,** *9* (4), 353-358.

82. Kasavajjula, U.; Wang, C. S.; Appleby, A. J., Nano- and bulk-silicon-based insertion anodes for lithium-ion secondary cells. *J Power Sources* **2007,** *163* (2), 1003-1039.

83. Bao, Z. H.; Weatherspoon, M. R.; Shian, S.; Cai, Y.; Graham, P. D.; Allan, S. M.; Ahmad, G.; Dickerson, M. B.; Church, B. C.; Kang, Z. T.; Abernathy, H. W.; Summers, C. J.; Liu, M. L.; Sandhage, K. H., Chemical reduction of three-dimensional silica micro-assemblies into microporous silicon replicas. *Nature* **2007,** *446* (7132), 172-175.

84. van Sark, W. G. J. H. M.; Brandsen, G. W.; Fleuster, M.; Hekkert, M. P., Analysis of the silicon market: Will thin films profit? *Energ Policy* **2007,** *35* (6), 3121-3125.

85. Muller, A.; Ghosh, M.; Sonnenschein, R.; Woditsch, P., Silicon for photovoltaic applications. *Mat Sci Eng B-Solid* **2006,** *134* (2-3), 257-262.

86. Jang, H. D.; Kim, H.; Chang, H.; Kim, J.; Roh, K. M.; Choi, H.; Cho, B. G.; Park, E.; Kim, H.; Luo, J. Y.; Huang, J. X., Aerosol-Assisted Extraction of Silicon Nanoparticles from Wafer Slicing Waste for Lithium Ion Batteries. *Sci Rep* **2015,** *5*.

87. Bang, B. M.; Lee, J. I.; Kim, H.; Cho, J.; Park, S., High-Performance Macroporous Bulk Silicon Anodes Synthesized by Template-Free Chemical Etching. *Adv Energy Mater* **2012,** *2* (7), 878-883.

88. Bang, B. M.; Kim, H.; Song, H. K.; Cho, J.; Park, S., Scalable approach to multi-dimensional bulk Si anodes via metal-assisted chemical etching. *Energy Environ Sci* **2011,** *4* (12), 5013-5019.

89. Yi, R.; Dai, F.; Gordin, M. L.; Chen, S. R.; Wang, D. H., Micro-sized Si-C Composite with Interconnected Nanoscale Building Blocks as High-Performance Anodes for Practical Application in Lithium-Ion Batteries. *Adv Energy Mater* **2013,** *3* (3), 295-300.

90. Jang, H. D.; Kim, H.; Kil, D. S.; Chang, H., A Novel Recovery of Silicon Nanoparticles from a Waste Silicon Sludge. *J Nanosci Nanotechnol* **2013,** *13* (3), 2334-2338.

91. Byon, H. R.; Lee, S. W.; Chen, S.; Hammond, P. T.; Shao-Horn, Y., Thin films of carbon nanotubes and chemically reduced graphenes for electrochemical micro-capacitors. *Carbon* **2011,** *49* (2), 457-467.

92. Li, D.; Muller, M. B.; Gilje, S.; Kaner, R. B.; Wallace, G. G., Processable aqueous dispersions of graphene nanosheets. *Nat Nanotechnol* **2008,** *3* (2), 101-105.

93. Krishnan, D.; Raidongia, K.; Shao, J. J.; Huang, J. X., Graphene Oxide Assisted Hydrothermal Carbonization of Carbon Hydrates. *Acs Nano* **2014,** *8* (1), 449-457.

94. Wang, J.; Meng, X. C.; Fan, X. L.; Zhang, W. B.; Zhang, H. Y.; Wang, C. S., Scalable Synthesis of Defect Abundant Si Nanorods for High-Performance Li-Ion Battery Anodes. *Acs Nano* **2015,** *9* (6), 6576-6586.

95. Etacheri, V.; Wang, C. W.; O'Connell, M. J.; Chan, C. K.; Pol, V. G., Porous carbon sphere anodes for enhanced lithium-ion storage. *J Mater Chem A* **2015,** *3* (18), 9861-9868.

96. Zhang, H. R.; Qin, X. Y.; Wu, J. X.; He, Y. B.; Du, H. D.; Li, B. H.; Kang, F. Y., Electrospun core-shell silicon/carbon fibers with an internal honeycomb-like conductive carbon framework as an anode for lithium ion batteries. *J Mater Chem A* **2015,** *3* (13), 7112-7120.

97. Kim, N.; Oh, C.; Kim, J.; Kim, J.-S.; Jeong, E. D.; Bae, J.-S.; Hong, T. E.; Lee, J. K., High-Performance Li-Ion Battery Anodes Based on Silicon-Graphene Self-Assemblies. *J. Electrochem. Soc* **2017,** *164* (1), A6075-A6083.

98. Li, N.; Jin, S. X.; Liao, Q. Y.; Cu, H.; Wang, C. X., Encapsulated within graphene shell silicon nanoparticles anchored on vertically aligned graphene trees as lithium ion battery anodes. *Nano Energy* **2014,** *5*, 105-115.

99. Guo, J. C.; Sun, A.; Chen, X. L.; Wang, C. S.; Manivannan, A., Cyclability study of silicon-carbon composite anodes for lithium-ion batteries using electrochemical impedance spectroscopy. *Electrochim Acta* **2011,** *56* (11), 3981-3987.

100. Dsoke, S.; Fuchs, B.; Gucciardi, E.; Wohlfahrt-Mehrens, M., The importance of the electrode mass ratio in a Li-ion capacitor based on activated carbon and Li4Ti5O12. *J Power Sources* **2015,** *282*, 385-393.

101. Li, B.; Dai, F.; Xiao, Q. F.; Yang, L.; Shen, J. M.; Zhang, C. M.; Cai, M., Nitrogen-doped activated carbon for a high energy hybrid supercapacitor. *Energy Environ Sci* **2016,** *9* (1), 102-106.

102. Jain, A.; Aravindan, V.; Jayaraman, S.; Kumar, P. S.; Balasubramanian, R.; Ramakrishna, S.; Madhavi, S.; Srinivasan, M. P., Activated carbons derived from coconut shells as high energy density cathode material for Li-ion capacitors. *Sci Rep* **2013,** *3*.

103. Fang, C.; Huang, Y.; Yuan, L. X.; Liu, Y. J.; Chen, W. L.; Huang, Y. Y.; Chen, K. Y.; Han, J. T.; Liu, Q. J.; Huang, Y. H., A Metal-Organic Compound as Cathode Material with Superhigh Capacity Achieved by Reversible Cationic and Anionic Redox Chemistry for High-Energy Sodium-Ion Batteries. *Angew Chem Int Ed* **2017,** *56* (24), 6793-6797.

104. Ding, J.; Wang, H. L.; Li, Z.; Cui, K.; Karpuzov, D.; Tan, X. H.; Kohandehghan, A.; Mitlin, D., Peanut shell hybrid sodium ion capacitor with extreme energy-power rivals lithium ion capacitors. *Energy Environ Sci* **2015,** *8* (3), 941-955.

105. Sevilla, M.; Fuertes, A. B., Chemical and Structural Properties of Carbonaceous Products Obtained by Hydrothermal Carbonization of Saccharides. *Chem-Eur J* **2009,** *15* (16), 4195-4203.

106. Hu, B.; Wang, K.; Wu, L. H.; Yu, S. H.; Antonietti, M.; Titirici, M. M., Engineering Carbon Materials from the Hydrothermal Carbonization Process of Biomass. *Adv Mater* **2010,** *22* (7), 813-828.

107. Sun, X. M.; Li, Y. D., Ag@C core/shell structured nanoparticles: Controlled synthesis, characterization, and assembly. *Langmuir* **2005,** *21* (13), 6019-6024.

108. Sun, X. M.; Li, Y. D., Colloidal carbon spheres and their core/shell structures with noble-metal nanoparticles. *Angew Chem Int Ed* **2004,** *43* (5), 597-601.

109. Liu, T. Y.; Kavian, R.; Chen, Z. M.; Cruz, S. S.; Noda, S.; Lee, S. W., Biomass-derived carbonaceous positive electrodes for sustainable lithium-ion storage. *Nanoscale* **2016,** *8* (6), 3671-3677.

110. Kumar, R.; Singh, R. K.; Singh, D. P.; Joanni, E.; Yadav, R. M.; Moshkalev, S. A., Laser-assisted synthesis, reduction and micro-patterning of graphene: Recent progress and applications. *Coordination Chem Rev* **2017,** *342*, 34-79.

111. Pomerantseva, E.; Gogotsi, Y., Two-dimensional heterostructures for energy storage. *Nat Energy* **2017,** *2* (7).

112. Hasegawa, K.; Noda, S., Lithium ion batteries made of electrodes with 99 wt% active materials and 1 wt% carbon nanotubes without binder or metal foils. *J Power Sources* **2016,** *321*, 155-162.

113. Liu, T.; Kim, K. C.; Lee, B.; Chen, Z. M.; Noda, S.; Jang, S. S.; Lee, S. W., Self-polymerized dopamine as an organic cathode for Li- and Na-ion batteries. *Energy Environ Sci* **2017,** *10* (1), 205-215.

114. Lee, S. W.; Yabuuchi, N.; Gallant, B. M.; Chen, S.; Kim, B. S.; Hammond, P. T.; Shao-Horn, Y., High-power lithium batteries from functionalized carbon-nanotube electrodes. *Nat Nanotechnol* **2010,** *5* (7), 531-537.

115. Shao, Y. Y.; Xiao, J.; Wang, W.; Engelhard, M.; Chen, X. L.; Nie, Z. M.; Gu, M.; Saraf, L. V.; Exarhos, G.; Zhang, J. G.; Liu, J., Surface-Driven Sodium Ion Energy Storage in Nanocellular Carbon Foams. *Nano Lett* **2013,** *13* (8), 3909-3914.
116. Lee, S. W.; Gallant, B. M.; Lee, Y.; Yoshida, N.; Kim, D. Y.; Yamada, Y.; Noda, S.; Yamada, A.; Shao-Horn, Y., Self-standing positive electrodes of oxidized few-walled carbon nanotubes for light-weight and high-power lithium batteries. *Energ Environ Sci* **2012,** *5* (1), 5437-5444.
117. Shin, H. J.; Kim, K. K.; Benayad, A.; Yoon, S. M.; Park, H. K.; Jung, I. S.; Jin, M. H.; Jeong, H. K.; Kim, J. M.; Choi, J. Y.; Lee, Y. H., Efficient Reduction of Graphite Oxide by Sodium Borohydride and Its Effect on Electrical Conductance. *Adv Funct Mater* **2009,** *19* (12), 1987-1992.
118. Tu, Z. Q.; Liu, Z. C.; Li, Y. F.; Yang, F.; Zhang, L. Q.; Zhao, Z.; Xu, C. M.; Wu, S. F.; Liu, H. W.; Yang, H. T.; Richard, P., Controllable growth of 1-7 layers of graphene by chemical vapour deposition. *Carbon* **2014,** *73*, 252-258.
119. Ferrari, A. C.; Robertson, J., Interpretation of Raman spectra of disordered and amorphous carbon. *Phys Rev B* **2000,** *61* (20), 14095-14107.
120. Lehman, J. H.; Terrones, M.; Mansfield, E.; Hurst, K. E.; Meunier, V., Evaluating the characteristics of multiwall carbon nanotubes. *Carbon* **2011,** *49* (8), 2581-2602.
121. Lu, B. Y.; Yan, J.; Xu, J. K.; Zhou, S. Y.; Hu, X. J., Novel Electroactive Proton-Doped Conducting Poly(aromatic ethers) with Good Fluorescence Properties via Electropolymerization. *Macromolecules* **2010,** *43* (10), 4599-4608.
122. Liu, T. Y.; Kim, K. C.; Kavian, R.; Jang, S. S.; Lee, S. W., High-Density Lithium-Ion Energy Storage Utilizing the Surface Redox Reactions in Folded Graphene Films. *Chem Mater* **2015,** *27* (9), 3291-3298.
123. Bachman, J. C.; Kavian, R.; Graham, D. J.; Kim, D. Y.; Noda, S.; Nocera, D. G.; Shao-Horn, Y.; Lee, S. W., Electrochemical polymerization of pyrene derivatives on functionalized carbon nanotubes for pseudocapacitive electrodes. *Nat Commun* **2015,** *6*.
124. Wang, C. L.; Fang, Y. G.; Xu, Y.; Liang, L. Y.; Zhou, M.; Zhao, H. P.; Lei, Y., Manipulation of Disodium Rhodizonate: Factors for Fast-Charge and Fast-

Discharge Sodium-Ion Batteries with Long-Term Cyclability. *Adv Funct Mater* **2016,** *26* (11), 1777-1786.

125. Li, B.; Dai, F.; Xiao, Q. F.; Yang, L.; Shen, J. M.; Zhang, C. M.; Cai, M., Activated Carbon from Biomass Transfer for High-Energy Density Lithium-Ion Supercapacitors. *Adv Energy Mater* **2016,** *6* (18).
126. Wang, Y. Q.; Ding, Y.; Pan, L. J.; Shi, Y.; Yue, Z. H.; Shi, Y.; Yu, G. H., Understanding the Size-Dependent Sodium Storage Properties of Na2C6O6-Based Organic Electrodes for Sodium-Ion Batteries. *Nano Lett* **2016,** *16* (5), 3329-3334.
127. Song, Z. P.; Qian, Y. M.; Zhang, T.; Otani, M.; Zhou, H. S., Poly(benzoquinonyl sulfide) as a High-Energy Organic Cathode for Rechargeable Li and Na Batteries. *Adv Sci* **2015,** *2* (9).
128. Luo, W.; Allen, M.; Raju, V.; Ji, X. L., An Organic Pigment as a High-Performance Cathode for Sodium-Ion Batteries. *Adv Energy Mater* **2014,** *4* (15).
129. Wang, S. W.; Wang, L. J.; Zhu, Z. Q.; Hu, Z.; Zhao, Q.; Chen, J., All Organic Sodium-Ion Batteries with Na4C8H2O6. *Angew Chem Int Edit* **2014,** *53* (23), 5892-5896.
130. Wang, H. G.; Yuan, S.; Ma, D. L.; Huang, X. L.; Meng, F. L.; Zhang, X. B., Tailored Aromatic Carbonyl Derivative Polyimides for High-Power and Long-Cycle Sodium-Organic Batteries. *Adv Energy Mater* **2014,** *4* (7).
131. Lee, B.; Liu, T.; Kim, S. K.; Chang, H.; Eom, K.; Xie, L.; Chen, S.; Jang, H. D.; Lee, S. W., Submicron silicon encapsulated with graphene and carbon as a scalable anode for lithium-ion batteries. *Carbon* **2017,** *119*, 438-445.
132. Gogotsi, Y.; Simon, P., True Performance Metrics in Electrochemical Energy Storage. *Science* **2011,** *334* (6058), 917-918.
133. Stoller, M. D.; Park, S. J.; Zhu, Y. W.; An, J. H.; Ruoff, R. S., Graphene-Based Ultracapacitors. *Nano Lett* **2008,** *8* (10), 3498-3502.
134. Stankovich, S.; Dikin, D. A.; Piner, R. D.; Kohlhaas, K. A.; Kleinhammes, A.; Jia, Y.; Wu, Y.; Nguyen, S. T.; Ruoff, R. S., Synthesis of graphene-based nanosheets via chemical reduction of exfoliated graphite oxide. *Carbon* **2007,** *45* (7), 1558-1565.

135. Blake, P.; Brimicombe, P. D.; Nair, R. R.; Booth, T. J.; Jiang, D.; Schedin, F.; Ponomarenko, L. A.; Morozov, S. V.; Gleeson, H. F.; Hill, E. W.; Geim, A. K.; Novoselov, K. S., Graphene-based liquid crystal device. *Nano Lett* **2008,** *8* (6), 1704-1708.

136. Hernandez, Y.; Nicolosi, V.; Lotya, M.; Blighe, F. M.; Sun, Z.; De, S.; McGovern, I. T.; Holland, B.; Byrne, M.; Gun'Ko, Y. K.; Boland, J. J.; Niraj, P.; Duesberg, G.; Krishnamurthy, S.; Goodhue, R.; Hutchison, J.; Scardaci, V.; Ferrari, A. C.; Coleman, J. N., High-yield production of graphene by liquid-phase exfoliation of graphite. *Nat Nanotechnol* **2008,** *3* (9), 563-8.

137. Luo, J. Y.; Jang, H. D.; Huang, J. X., Effect of Sheet Morphology on the Scalability of Graphene-Based Ultracapacitors. *Acs Nano* **2013,** *7* (2), 1464-1471.

138. Hsieh, C. T.; Teng, H., Influence of oxygen treatment on electric double-layer capacitance of activated carbon fabrics. *Carbon* **2002,** *40* (5), 667-674.

139. Lee, S. W.; Kim, B. S.; Chen, S.; Shao-Horn, Y.; Hammond, P. T., Layer-by-Layer Assembly of All Carbon Nanotube Ultrathin Films for Electrochemical Applications. *J Am Chem Soc* **2009,** *131* (2), 671-679.

140. Hyder, M. N.; Lee, S. W.; Cebeci, F. C.; Schmidt, D. J.; Shao-Horn, Y.; Hammond, P. T., Layer-by-Layer Assembled Polyaniline Nanofiber/Multiwall Carbon Nanotube Thin Film Electrodes for High-Power and High-Energy Storage Applications. *Acs Nano* **2011,** *5* (11), 8552-8561.

141. Byon, H. R.; Gallant, B. M.; Lee, S. W.; Shao-Horn, Y., Role of Oxygen Functional Groups in Carbon Nanotube/Graphene Freestanding Electrodes for High Performance Lithium Batteries. *Adv Funct Mater* **2013,** *23* (8), 1037-1045.

142. Kim, S. Y.; Hong, J.; Kavian, R.; Lee, S. W.; Hyder, M. N.; Shao-Horn, Y.; Hammond, P. T., Rapid fabrication of thick spray-layer-by-layer carbon nanotube electrodes for high power and energy devices. *Energy Environ Sci* **2013,** *6* (3), 888-897.

143. Ha, S. H.; Jeong, Y. S.; Lee, Y. J., Free Standing Reduced Graphene Oxide Film Cathodes for Lithium Ion Batteries. *Acs Appl Mater Inter* **2013,** *5* (23), 12295-12303.

144. Hummers, W. S.; Offeman, R. E., Preparation of Graphitic Oxide. *J Am Chem Soc* **1958,** *80* (6), 1339-1339.

145. Kim, D. Y.; Sugime, H.; Hasegawa, K.; Osawa, T.; Noda, S., Sub-millimeter-long carbon nanotubes repeatedly grown on and separated from ceramic beads in a single fluidized bed reactor. *Carbon* **2011,** *49* (6), 1972-1979.

146. Liu, T. Y.; Kavian, R.; Kim, I.; Lee, S. W., Self-Assembled, Redox-Active Graphene Electrodes for High-Performance Energy Storage Devices. *J Phys Chem Lett* **2014,** *5* (24), 4324-4330.

147. Ferrari, A. C.; Basko, D. M., Raman spectroscopy as a versatile tool for studying the properties of graphene. *Nat Nanotechnol* **2013,** *8* (4), 235-246.

148. Dresselhaus, M. S.; Jorio, A.; Saito, R., Characterizing Graphene, Graphite, and Carbon Nanotubes by Raman Spectroscopy. *Annu Rev Conden Ma P* **2010,** *1*, 89-108.

149. Pei, S. F.; Zhao, J. P.; Du, J. H.; Ren, W. C.; Cheng, H. M., Direct reduction of graphene oxide films into highly conductive and flexible graphene films by hydrohalic acids. *Carbon* **2010,** *48* (15), 4466-4474.

150. Ma, J.; Yang, M. X.; Yu, F.; Zheng, J., Water-enhanced Removal of Ciprofloxacin from Water by Porous Graphene Hydrogel. *Sci Rep* **2015,** *5*.

151. Huh, S. H., Thermal Reduction of Graphene Oxide. *Physics and Applications of Graphene - Experiments* **2011**, 73-90.

152. Compton, O. C.; Jain, B.; Dikin, D. A.; Abouimrane, A.; Amine, K.; Nguyen, S. T., Chemically Active Reduced Graphene Oxide with Tunable C/O Ratios. *Acs Nano* **2011,** *5* (6), 4380-4391.

153. Kundu, S.; Wang, Y. M.; Xia, W.; Muhler, M., Thermal Stability and Reducibility of Oxygen-Containing Functional Groups on Multiwalled Carbon Nanotube Surfaces: A Quantitative High-Resolution XPS and TPD/TPR Study. *J Phys Chem C* **2008,** *112* (43), 16869-16878.

154. Periasamy, A. P.; Liu, J. F.; Lin, H. M.; Chang, H. T., Synthesis of copper nanowire decorated reduced graphene oxide for electro-oxidation of methanol. *J Mater Chem A* **2013,** *1* (19), 5973-5981.

155. Cao, X. H.; Shi, Y. M.; Shi, W. H.; Lu, G.; Huang, X.; Yan, Q. Y.; Zhang, Q. C.; Zhang, H., Preparation of Novel 3D Graphene Networks for Supercapacitor Applications. *Small* **2011,** *7* (22), 3163-3168.

156. Stankovich, S.; Piner, R. D.; Chen, X. Q.; Wu, N. Q.; Nguyen, S. T.; Ruoff, R. S., Stable aqueous dispersions of graphitic nanoplatelets via the reduction of exfoliated graphite oxide in the presence of poly(sodium 4-styrenesulfonate). *Journal of Materials Chemistry* **2006,** *16* (2), 155-158.

157. Lei, Z. B.; Lu, L.; Zhao, X. S., The electrocapacitive properties of graphene oxide reduced by urea. *Energy Environ Sci* **2012,** *5* (4), 6391-6399.

158. Wu, Z. S.; Sun, Y.; Tan, Y. Z.; Yang, S. B.; Feng, X. L.; Mullen, K., Three-Dimensional Graphene-Based Macro- and Mesoporous Frameworks for High-Performance Electrochemical Capacitive Energy Storage. *J Am Chem Soc* **2012,** *134* (48), 19532-19535.

159. Chen, J.; Li, C.; Shi, G. Q., Graphene Materials for Electrochemical Capacitors. *J Phys Chem Lett* **2013,** *4* (8), 1244-1253.

160. Hwang, J. Y.; Myung, S. T.; Sun, Y. K., Sodium-ion batteries: present and future. *Chem Soc Rev* **2017,** *46* (12), 3529-3614.

161. Liu, T. Y.; Lee, B.; Lee, M. J.; Park, J.; Chen, Z. M.; Noda, S.; Lee, S. W., Improved capacity of redox-active functional carbon cathodes by dimension reduction for hybrid supercapacitors. *J Mater Chem A* **2018,** *6* (8), 3367-3375.

162. Wakeland, S.; Martinez, R.; Grey, J. K.; Luhrs, C. C., Production of graphene from graphite oxide using urea as expansion-reduction agent. *Carbon* **2010,** *48* (12), 3463-3470.

163. Shih, C. J.; Lin, S. C.; Strano, M. S.; Blankschtein, D., Understanding the Stabilization of Liquid-Phase-Exfoliated Graphene in Polar Solvents: Molecular Dynamics Simulations and Kinetic Theory of Colloid Aggregation. *J Am Chem Soc* **2010,** *132* (41), 14638-14648.

164. Martinez, C. R.; Iverson, B. L., Rethinking the term "pi-stacking". *Chemical Science* **2012,** *3* (7), 2191-2201.

165. Ma, X. F.; Zachariah, M. R.; Zangmeister, C. D., Crumpled Nanopaper from Graphene Oxide. *Nano Lett* **2012,** *12* (1), 486-489.

166. Wang, G. K.; Sun, X.; Lu, F. Y.; Sun, H. T.; Yu, M. P.; Jiang, W. L.; Liu, C. S.; Lian, J., Flexible Pillared Graphene-Paper Electrodes for High-Performance Electrochemical Supercapacitors. *Small* **2012,** *8* (3), 452-459.

167. Mattevi, C.; Eda, G.; Agnoli, S.; Miller, S.; Mkhoyan, K. A.; Celik, O.; Mastrogiovanni, D.; Granozzi, G.; Garfunkel, E.; Chhowalla, M., Evolution of Electrical, Chemical, and Structural Properties of Transparent and Conducting Chemically Derived Graphene Thin Films. *Adv Funct Mater* **2009,** *19* (16), 2577-2583.

168. Chua, C. K.; Pumera, M., Chemical reduction of graphene oxide: a synthetic chemistry viewpoint. *Chem Soc Rev* **2014,** *43* (1), 291-312.

169. Dreyer, D. R.; Park, S.; Bielawski, C. W.; Ruoff, R. S., The chemistry of graphene oxide. *Chem Soc Rev* **2010,** *39* (1), 228-240.

170. Cheng, Q.; Tang, J.; Ma, J.; Zhang, H.; Shinya, N.; Qin, L. C., Graphene and nanostructured MnO2 composite electrodes for supercapacitors. *Carbon* **2011,** *49* (9), 2917-2925.

171. Tollefson, J., Car industry: CHARGING UP THE FUTURE. *Nature* **2008,** *456* (7221), 436-440.

172. Ellingsen, L. A. W.; Hung, C. R.; Majeau-Bettez, G.; Singh, B.; Chen, Z. W.; Whittingham, M. S.; Stromman, A. H., Nanotechnology for environmentally sustainable electromobility (vol 11, pg 1039, 2016). *Nat Nanotechnol* **2017,** *12* (1), 90-90.

173. Vaalma, C.; Buchholz, D.; Weil, M.; Passerini, S., A cost and resource analysis of sodium-ion batteries. *Nat Rev Mater* **2018,** *3*, 18013.

174. Hong, Y. S.; Li, N.; Chen, H. S.; Wang, P.; Song, W. L.; Fang, D. N., In operando observation of chemical and mechanical stability of Li and Na dendrites under quasi-zero electrochemical field. *Energy Storage Materials* **2018,** *11*, 118-126.

175. Wenzel, S.; Hara, T.; Janek, J.; Adelhelm, P., Room-temperature sodium-ion batteries: Improving the rate capability of carbon anode materials by templating strategies. *Energy Environ Sci* **2011,** *4* (9), 3342-3345.

176. Yuan, B. H.; Bao, C. L.; Qian, X. D.; Wen, P. Y.; Xing, W. Y.; Song, L.; Hu, Y., A facile approach to prepare graphene via solvothermal reduction of graphite oxide. *Mater Res Bull* **2014,** *55*, 48-52.

177. Kumar, N. A.; Gaddam, R. R.; Varanasi, S. R.; Yang, D. F.; Bhatia, S. K.; Zhao, X. S., Sodium ion storage in reduced graphene oxide. *Electrochim Acta* **2016,** *214*, 319-325.

178. Emery, N.; Herold, C.; d'Astuto, M.; Garcia, V.; Bellin, C.; Mareche, J. F.; Lagrange, P.; Loupias, G., Superconductivity of bulk CaC6. *Phys Rev Lett* **2005,** *95* (8).

179. Stevens, D. A.; Dahn, J. R., High capacity anode materials for rechargeable sodium-ion batteries. *J Electrochem Soc* **2000,** *147* (4), 1271-1273.

180. Hwang, J. Y.; Li, M. P.; El-Kady, M. F.; Kaner, R. B., Next-Generation Activated Carbon Supercapacitors: A Simple Step in Electrode Processing Leads to Remarkable Gains in Energy Density. *Adv Funct Mater* **2017,** *27* (15).

181. Yun, Y. S.; Park, Y. U.; Chang, S. J.; Kim, B. H.; Choi, J.; Wang, J. J.; Zhang, D.; Braun, P. V.; Jin, H. J.; Kang, K., Crumpled graphene paper for high power sodium battery anode. *Carbon* **2016,** *99*, 658-664.

182. Nakada, K.; Ishii, A., DFT Calculation for Adatom Adsorption on Graphene. *Graphene Simulation* **2011**, 3-20.

183. Zang, J. F.; Ryu, S.; Pugno, N.; Wang, Q. M.; Tu, Q.; Buehler, M. J.; Zhao, X. H., Multifunctionality and control of the crumpling and unfolding of large-area graphene. *Nature Materials* **2013,** *12* (4), 321-325.

184. Li, S.; Qiu, J. X.; Lai, C.; Ling, M.; Zhao, H. J.; Zhang, S. Q., Surface capacitive contributions: Towards high rate anode materials for sodium ion batteries. *Nano Energy* **2015,** *12*, 224-230.

185. Ding, J.; Wang, H. L.; Li, Z.; Kohandehghan, A.; Cui, K.; Xu, Z. W.; Zahiri, B.; Tan, X. H.; Lotfabad, E. M.; Olsen, B. C.; Mitlin, D., Carbon Nanosheet Frameworks Derived from Peat Moss as High Performance Sodium Ion Battery Anodes. *Acs Nano* **2013,** *7* (12), 11004-11015.

186. Luo, W.; Wan, J. Y.; Ozdemir, B.; Bao, W. Z.; Chen, Y. N.; Dai, J. Q.; Lin, H.; Xu, Y.; Gu, F.; Barone, V.; Hu, L. B., Potassium Ion Batteries with Graphitic Materials. *Nano Letters* **2015,** *15* (11), 7671-7677.

187. Lotfabad, E. M.; Ding, J.; Cui, K.; Kohandehghan, A.; Kalisvaart, W. P.; Hazelton, M.; Mitlin, D., High-Density Sodium and Lithium Ion Battery Anodes from Banana Peels. *Acs Nano* **2014,** *8* (7), 7115-7129.

188. Ding, J.; Li, Z.; Cui, K.; Boyer, S.; Karpuzov, D.; Mitlin, D., Heteroatom enhanced sodium ion capacity and rate capability in a hydrogel derived carbon give record performance in a hybrid ion capacitor. *Nano Energy* **2016,** *23*, 129-137.

189. Diez, N.; Sliwak, A.; Gryglewicz, S.; Grzyb, B.; Gryglewicz, G., Enhanced reduction of graphene oxide by high-pressure hydrothermal treatment. *Rsc Adv* **2015,** *5* (100), 81831-81837.

190. Chen, H. Y.; Bucher, N.; Hartung, S.; Li, L. L.; Friedl, J.; Liou, H. P.; Sun, C. L.; Stimming, U.; Srinivasan, M., A Multi-Walled Carbon Nanotube Core with Graphene Oxide Nanoribbon Shell as Anode Material for Sodium Ion Batteries. *Adv Mater Interfaces* **2016,** *3* (20).

191. Luo, W.; Bommier, C.; Jian, Z. L.; Li, X.; Carter, R.; Vail, S.; Lu, Y. H.; Lee, J. J.; Ji, X. L., Low-Surface-Area Hard Carbon Anode for Na-Ion Batteries via Graphene Oxide as a Dehydration Agent. *Acs Appl Mater Inter* **2015,** *7* (4), 2626-2631.

192. Deng, X.; Xie, K. Y.; Li, L.; Zhou, W.; Sunarso, J.; Shao, Z. P., Scalable synthesis of self-standing sulfur-doped flexible graphene films as recyclable anode materials for low-cost sodium-ion batteries. *Carbon* **2016,** *107*, 67-73.

193. Liu, S.; Wang, A. X.; Li, Q. Q.; Wu, J. S.; Chiou, K. V.; Huang, J. X.; Luo, J. Y., Crumpled Graphene Balls Stabilized Dendrite-free Lithium Metal Anodes. *Joule* **2018,** *2* (1), 184-193.

194. Hwang, T. H.; Jung, D. S.; Kim, J. S.; Kim, B. G.; Choi, J. W., One-Dimensional Carbon-Sulfur Composite Fibers for Na-S Rechargeable Batteries Operating at Room Temperature. *Nano Lett* **2013,** *13* (9), 4532-4538.

195. Wang, H. G.; Wu, Z.; Meng, F. L.; Ma, D. L.; Huang, X. L.; Wang, L. M.; Zhang, X. B., Nitrogen-Doped Porous Carbon Nanosheets as Low-Cost, High-

Performance Anode Material for Sodium-Ion Batteries. *Chemsuschem* **2013,** *6* (1), 56-60.

196. David, L.; Singh, G., Reduced Graphene Oxide Paper Electrode: Opposing Effect of Thermal Annealing on Li and Na Cyclability. *J Phys Chem C* **2014,** *118* (49), 28401-28408.

197. Augustyn, V.; Come, J.; Lowe, M. A.; Kim, J. W.; Taberna, P. L.; Tolbert, S. H.; Abruna, H. D.; Simon, P.; Dunn, B., High-rate electrochemical energy storage through Li+ intercalation pseudocapacitance. *Nat Mater* **2013,** *12* (6), 518-522.

198. Cook, J. B.; Kim, H. S.; Yan, Y.; Ko, J. S.; Robbennolt, S.; Dunn, B.; Tolbert, S. H., Mesoporous MoS2 as a Transition Metal Dichalcogenide Exhibiting Pseudocapacitive Li and Na-Ion Charge Storage. *Adv Energy Mater* **2016,** *6* (9).

199. Liu, Y. Y.; Merinov, B. V.; Goddard, W. A., Origin of low sodium capacity in graphite and generally weak substrate binding of Na and Mg among alkali and alkaline earth metals. *Proc Natl Acad Sci* **2016,** *113* (14), 3735-3739.

200. Gao, Z.; Zhang, Y. Y.; Song, N. N.; Li, X. D., Biomass-derived renewable carbon materials for electrochemical energy storage. *Mater Res Lett* **2017,** *5* (2), 69-88.

201. Xu, Y. X.; Lin, Z. Y.; Zhong, X.; Huang, X. Q.; Weiss, N. O.; Huang, Y.; Duan, X. F., Holey graphene frameworks for highly efficient capacitive energy storage. *Nat Commun* **2014,** *5*.

202. Tao, Y.; Xie, X. Y.; Lv, W.; Tang, D. M.; Kong, D. B.; Huang, Z. H.; Nishihara, H.; Ishii, T.; Li, B. H.; Golberg, D.; Kang, F. Y.; Kyotani, T.; Yang, Q. H., Towards ultrahigh volumetric capacitance: graphene derived highly dense but porous carbons for supercapacitors. *Sci Rep* **2013,** *3*.

203. Li, C.; Zhang, X.; Wang, K.; Zhang, H. T.; Sun, X. Z.; Ma, Y. W., Three dimensional graphene networks for supercapacitor electrode materials. *New Carbon Mater* **2015,** *30* (3), 193-206.

204. Xu, W.; Wang, J. L.; Ding, F.; Chen, X. L.; Nasybutin, E.; Zhang, Y. H.; Zhang, J. G., Lithium metal anodes for rechargeable batteries. *Energy Environ Sci* **2014,** *7* (2), 513-537.

205. Cheng, X. B.; Zhang, R.; Zhao, C. Z.; Wei, F.; Zhang, J. G.; Zhang, Q., A Review of Solid Electrolyte Interphases on Lithium Metal Anode. *Adv Sci* **2016,** *3* (3).

206. Wood, K. N.; Noked, M.; Dasgupta, N. P., Lithium Metal Anodes: Toward an Improved Understanding of Coupled Morphological, Electrochemical, and Mechanical Behavior. *ACS Energy Lett.* **2017,** *2* (3), 664-672.

207. Xin, S.; You, Y.; Wang, S.; Gao, H. C.; Yin, Y. X.; Guo, Y. G., Solid-State Lithium Metal Batteries Promoted by Nanotechnology: Progress and Prospects. *ACS Energy Lett.* **2017,** *2* (6), 1385-1394.

208. Cheng, X. B.; Zhang, R.; Zhao, C. Z.; Zhang, Q., Toward Safe Lithium Metal Anode in Rechargeable Batteries: A Review. *Chem Rev* **2017,** *117* (15), 10403-10473.

209. Mauger, A.; Armand, M.; Julien, C. M.; Zaghib, K., Challenges and issues facing lithium metal for solid-state rechargeable batteries. *J Power Sources* **2017,** *353*, 333-342.

210. Lin, D. C.; Liu, Y. Y.; Pei, A.; Cui, Y., Nanoscale perspective: Materials designs and understandings in lithium metal anodes. *Nano Res* **2017,** *10* (12), 4003-4026.

211. Lin, D. C.; Liu, Y. Y.; Cui, Y., Reviving the lithium metal anode for high-energy batteries. *Nat Nanotechnol* **2017,** *12* (3), 194-206.

212. Tikekar, M. D.; Choudhury, S.; Tu, Z. Y.; Archer, L. A., Design principles for electrolytes and interfaces for stable lithium-metal batteries. *Nat Energy* **2016,** *1*, 1-7.

213. Li, B.; Wang, Y.; Yang, S. B., A Material Perspective of Rechargeable Metallic Lithium Anodes. *Adv Energy Mater* **2018,** *8* (13).

214. Wang, H.; Wang, C.; Matios, E.; Li, W., Critical Role of Ultrathin Graphene Films with Tunable Thickness in Enabling Highly Stable Sodium Metal Anodes. *Nano Lett.* **2017,** *17*, 6808-6815.

215. Jung, K. N.; Kim, J.; Yamauchi, Y.; Park, M. S.; Lee, J. W.; Kim, J. H., Rechargeable lithium-air batteries: a perspective on the development of oxygen electrodes. *J Mater Chem A* **2016,** *4* (37), 14050-14068.